

**SORPTION OF N₂, CO₂ AND CH₄ ON THE
ULTRASOUND ENHANCED CATION
EXCHANGED X ZEOLITES**

**A Thesis Submitted to
the Graduate School of Engineering and Sciences of
İzmir Institute of Technology
in Partial Fulfillment of the Requirements for the Degree of**

DOCTOR OF PHILOSOPHY

in Chemical Engineering

**by
Yasemin ERTEN KAYA**

**June 2011
İZMİR**

APPROVAL PAGE

ACKNOWLEDGEMENT

First and foremost, I am especially grateful to my advisor Assoc. Dr. Fehime akıcıođlu-Özkan for her guidance, support and encouragement in all steps of this study.

I wish to express my gratitude to my committee members, Prof. Dr. Sacide Alsoy, Prof. Dr. Semra Ülkü, Prof. Dr. Mustafa Güden and Prof. Dr. Hayrettin Yücel for their insightful comments and constructive criticism, which helped to improve the overall quality of my thesis.

I am also thankful to State Planning Organization of Turkey (DPT) and IYTE Research Foundation for their financial supports to this project.

Special thanks to my officemates; Filiz Yaşar Mahlıçlı, Metin Uz, Alev Güneş Yerkesikli, Gülşim Ural, Senem Yetgin, Dilek Demirbuker Kavak and Didem Berkun for their friendship and interest. My absolute thanks to Nesrin Tatlıdil, Nesrin Gaffarođulları and MAM team for their precious contributions during analysis of the samples.

Lastly, I am eternally grateful for the unconditionally support and encouragement of my parents. I wish to express my endless love to my husband, Hamdi Kaya and my sisters Saliha Ađan and Yeter Erten for their patience and their trust.

ABSTRACT

SORPTION OF N₂, CO₂ AND CH₄ ON THE ULTRASOUND ENHANCED CATION EXCHANGED X ZEOLITES

Li⁺, Ca²⁺ and Ce³⁺ ions exchange on NaX zeolite under ultrasonic irradiation and the N₂, CO₂ and CH₄ sorption on the zeolites obtained by using Zero Length Column (ZLC) technique were studied.

The kinetic and equilibrium of ion exchange were applied in the concentration range of 3-9 fold equivalent excess at 50 °C and 70 °C. The results obtained from the ultrasonic method was compared with the traditional method. Maximum exchange percent was obtained under ultrasonic irradiation as 76, 72 and 66 for Li⁺, Ca²⁺ and Ce³⁺ ions exchange, respectively. The kinetics of the ion exchange of Li⁺, Ca²⁺, Ce³⁺ ions into NaX zeolite has been investigated with models; pseudo first order, pseudo second order reaction models, intraparticle and external diffusion models. At initial, ion exchange is very fast kinetically and completed within about 15 min. After that both mechanism: intraparticle and external resistance are dominant which are proved with Biot number.

The experimental conditions in zero length column are adjusted to control the adsorption under diffusion. The adsorbents selected for adsorption in ZLC have the convenient average pore diameters for CO₂, N₂ and CH₄ adsorption. The kinetic gas selectivities, S_{CO_2/CH_4} , S_{CO_2/N_2} , S_{N_2/CH_4} at 30 °C, 60 °C and 90 °C are lower than 5 for all the adsorbents. The lowest selectivity is obtained for NaX zeolite. The CO₂ selectivity over CH₄ and N₂ are higher than N₂ selectivity over CH₄ for all the adsorbents ($S_{CO_2/CH_4}, S_{CO_2/N_2} > S_{N_2/CH_4}$). This can be explained with the high electrostatic interaction and the low kinetic diameter of CO₂ than the other gases.

ÖZET

ULTRASES İLE KATYON DEĞİŞİMİ ARTTIRILMIŞ X ZEOLİTLERİNE N₂, CO₂ ve CH₄ SORPSİYONU

Ultrases kullanımı ile NaX zeoliti üzerine Li⁺, Ca²⁺ ve Ce³⁺ iyonlarının değişimi çalışılmış ve elde edilen zeolitler üzerine N₂, CO₂ ve CH₄ sorpsiyonu ZLC tekniği kullanılarak çalışılmıştır.

İyon değişim denge ve kinetiği 50 °C ve 70 °C de 3-9 kat eşdeğer aşırı konsantrasyon aralığında uygulanmıştır. Ultrasonik yöntem ile elde edilen sonuçlar geleneksel yöntemi ile karşılaştırılmıştır. Maksimum değişim ultrasonik yöntem sonrasında Li⁺, Ca²⁺ ve Ce³⁺ iyonları için sırasıyla yüzde 76, 72 ve 66 bulunmuştur. İyon değişim kinetiği sözde birinci ve ikinci dereceden reaksiyon modelleri ile parçacık içi ve yüzey difuzyon modelleri ile incelenmiştir. İlk 15 dakika içerisinde iyon değişimi kinetik olarak çok hızlı olmuştur. Sonrasında iyon değişim üzerine parçacık içi ve yüzey difuzyon dirençlerinin hakim olduğu Biot sayısı ile kanıtlanmıştır.

ZLC sistemde deneysel koşullar difuzyon kontrolü altında gerçekleştirilmiştir. Adsorpsiyon için seçilen adsorbentler, CO₂, N₂ ve CH₄ gazları için uygun ortalama gözenek çaplarına sahiptirler. Adsorbentlerin gazlara karşı kinetik seçiciliği, S_{CO_2/CH_4} , S_{CO_2/N_2} , S_{N_2/CH_4} , 30 °C, 60 °C ve 90 °C'de 5 den küçük bulunmuştur. En düşük seçicilik NaX zeoliti için elde edilmiştir. CO₂ gazının CH₄ ve N₂ gazlarına karşı seçiciliği N₂ gazının CH₄ gazına karşı olan seçiciliğinden daha fazla bulunmuştur ($S_{CO_2/CH_4}, S_{CO_2/N_2} > S_{N_2/CH_4}$). Elde edilen sonuç, CO₂ gazının diğer gazlara göre yüksek elektrostatik etkileşimi ve düşük kinetik çapına sahip olması ile açıklanabilir.

dedicated to

my family

TABLE OF CONTENTS

LIST OF FIGURES.....	xi
LIST OF TABLES.....	xv
CHAPTER 1. INTRODUCTION.....	1
CHAPTER 2. ZEOLITE.....	4
2.1. Zeolite Science	4
2.2. Structure of Zeolite.....	5
2.3. The Synthetic 13X (NaX or X) Zeolite.....	6
2.4. The Important Characteristics and Application of Zeolites	9
2.5. The Granulation Form of Zeolite.....	10
2.5.1. Structure and Properties of Montmorillonite and Sepiolite Minerals.....	11
CHAPTER 3. ULTRASOUND.....	14
3.1. Physical Mechanisms of Ultrasound.....	16
3.1.1. Acoustic Streaming.....	16
3.1.2. Microstreaming due to Cavitation.....	17
3.1.3. Microjets.....	18
3.1.4. Shock Waves.....	19
3.2. Cavitation Phenomenon Influencing with Factors.....	19
3.3. Types of Ultrasound Devices.....	20
3.3.1. The Ultrasonic Cleaning Bath.....	21
3.3.2. Ultrasonic Probe.....	22
CHAPTER 4. ION EXCHANGE.....	26
4.1. Ion Exchange Isotherms for NaX Zeolite.....	29
4.2. Sorption: Ion exchange & Adsorption.....	30
4.2.1. Ion Exchange Kinetics.....	32
4.2.2. Kinetic Models.....	33

4.2.2.1. Reaction Models.....	34
4.2.2.2. Diffusion Models.....	35
4.3. Thermodynamics of Ion Exchange	41
CHAPTER 5. GAS ADSORPTION.....	43
5.1. Gas Adsorption Measurement Technique.....	44
5.2. The ZLC Method for Single Component System: Background and Theory.....	48
5.2.1. Flow Through Zero Length Column.....	49
5.2.2. Mathematical Models.....	52
5.2.3. Analysis Dimensionless Theoretical ZLC Curves.....	55
5.3. Selectivity.....	56
5.4. Thermodynamics of Gas Adsorption.....	57
CHAPTER 6. EXPERIMENTAL STUDIES.....	59
6.1. Ion Exchange Studies.....	60
6.2. Granule Formation of NaX Zeolite.....	62
6.2.1. Measurement of True Density.....	64
6.3. ZLC Adsorption System.....	64
6.3.1. Data Collection and Analysis.....	66
CHAPTER 7. RESULTS AND DISCUSSIONS.....	67
7.1. Ion Exchange Studies.....	67
7.1.1. Kinetic Studies.....	68
7.1.2. Consecutive Studies.....	94
7.2. Characterization Studies.....	95
7.2.1. Zeolite Granules.....	96
7.2.2. Ion Exchanged Zeolites.....	104
7.3. Adsorption of N ₂ , CO ₂ and CH ₄ on Zeolites by Zero Length Column Technique.	113
CHAPTER 8. CONCLUSION.....	129

REFERENCES.....	133
APPENDICES	
APPENDIX A. ION EXCHANGE STUDY.....	141
APPENDIX B. THE TEMPERATURE EFFECT ON INTRAPARTICLE RATE CONSTANT OF ION EXCHANGE.....	151
APPENDIX C. CHARACTERIZATION STUDY FOR ZEOLITE GRANULES...	155
APPENDIX D. ZLC STUDY	157

LIST OF FIGURES

<u>Figure</u>	<u>Page</u>
Figure 2.1. Faujasite structure showing cation sites (I, II, III) and locations of oxygen atoms (1, 2, 3, 4)	6
Figure 2.2. Crystal structure of NaX zeolite	8
Figure 2.3. Cation sites in NaX zeolite (the numbers refer to cation sites)	8
Figure 2.4. Schematic representation of a biporous particle.....	10
Figure 2.5. A schematic representation of sepiolite.....	12
Figure 2.6. The structure of 2:1 type montmorillonite.....	12
Figure 3.1. Frequency ranges of sound.....	14
Figure 3.2. Successive growth cycle and bubble collapse.....	17
Figure 3.3. Variation of the threshold intensity with frequency (a) in aerated (b) in air-free water.....	18
Figure 3.4. A typical ultrasonic cleaning bath.....	21
Figure 3.5. The illustration of ultrasonic processor.....	22
Figure 3.6. Ultrasonic horn immersed to the vessel.....	24
Figure 3.7. Shapes of the acoustic horns	24
Figure 4.1. Two-dimensional representation of the zeolite structure.....	26
Figure 4.2. Equivalent character of ion exchange for (a) $\text{Li}^+_{\text{aq}} + \text{Na-X}_{(\text{zeo})} = \text{Na}^+_{(\text{aq})} + \text{Li-X}_{(\text{zeo})}$ (b) $\text{Ca}^{2+}_{\text{aq}} + \text{Na-X}_{(\text{zeo})} = 2\text{Na}^+_{(\text{aq})} + \text{Ca-X}_{(\text{zeo})}$	27
Figure 4.3. Types of ion exchange isotherms.....	29
Figure 4.4. General scheme of mass transfer and diffusion mechanism.....	33
Figure 5.1. Representative adsorption and desorption on adsorbent.....	43
Figure 5.2. Representative Zero Length Column including zeolite granules.....	48
Figure 5.3. Zero Length Column.....	52
Figure 5.4. Dimensionless theoretical ZLC curves (a) Diffusion controlled system for $C/C_0 > 0.7$ (b) Diffusion controlled system for $C/C_0 < 0.3$	56
Figure 6.1. Experimental set-up of ultrasonic processor.....	61
Figure 6.2. Flow sheet for preparation of NaX granule.....	63
Figure 6.3. Displacement type pycnometer (helium densitometer)	64
Figure 6.4. Zero Length Column configurations.....	65

Figure 6.5. Qualitative (a) Raw ZLC response and (b) Normalized reponse curve...	66
Figure 7.1. Kinetic curves of Li^+ ion exchange at 50 °C (fold equivalent excess: (a) 3 (b) 6 (c) 9)	68
Figure 7.2. Kinetic curves of Li^+ ion exchange at 70 °C (fold equivalent excess: (a) 3 (b) 6 (c) 9)	69
Figure 7.3. Kinetic curves of Ca^{2+} ion exchange at 50 °C (fold equivalent excess: (a) 3 (b) 6 (c) 9)	70
Figure 7.4. Kinetic curves of Ca^{2+} ion exchange at 70 °C (fold equivalent excess: (a) 3 (b) 6 (c) 9)	71
Figure 7.5. Kinetic curves of Ce^{3+} ion exchange at 50 °C (fold equivalent excess: (a) 3 (b) 5 c) 6 (d) 9)	72
Figure 7.6. Kinetic curves of Ce^{3+} ion exchange at 70 °C (fold equivalent excess: (a) 3 (b) 5 c) 6 (d) 9)	73
Figure 7.7. Kinetic curves at 70 °C for exchange of (a) Li^+ (b) Ca^{2+} (c) Ce^{3+} ions...	75
Figure 7.8. Li-exchange isotherm at 50 °C (■,●) and 70 °C (□,○) by using traditional (solid line) and ultrasonic (dashed line) method.....	79
Figure 7.9. Ca-exchange isotherm at 50 °C (■,●) and 70 °C (□,○) by using traditional (solid line) and ultrasonic (dashed line) method.....	80
Figure 7.10. Ce-exchange isotherm at 50 °C (■,●) and 70 °C (□,○) by using traditional (solid line) and ultrasonic (dashed line) method.....	80
Figure 7.11. Intraparticle diffusion kinetic curves of Li- exchange at 50 °C (fold equivalent excess: (a) 3 (b) 6 c) 9)	82
Figure 7.12. Intraparticle diffusion kinetic curves of Li- exchange at 70 °C (fold equivalent excess: (a) 3 (b) 6 c) 9)	83
Figure 7.13. Intraparticle diffusion kinetic curves of Ca- exchange at 50 °C (fold equivalent excess: (a) 3 (b) 6 c) 9)	84
Figure 7.14. Intraparticle diffusion kinetic curves of Ca- exchange at 70 °C (fold equivalent excess: (a) 3 (b) 6 c) 9)	85
Figure 7.15. Intraparticle diffusion kinetic curves of Ce- exchange at 50 °C (fold equivalent excess: (a) 3 (b) 5 (c) 6 (d) 9)	86
Figure 7.16. Intraparticle diffusion kinetic curves of Ce- exchange at 70 °C (fold equivalent excess: (a) 3 (b) 5 (c) 6 (d) 9)	87

Figure 7.17. Ion exchange with consecutive cation solution of (a) Li^+ (b) Ca^{2+} (c) Ce^{3+} ions in traditional (T) and ultrasonic method (U)	94
Figure 7.18. N_2 adsorption isotherms of NaX zeolite sepiolite and montmorillonite	96
Figure 7.19. SEM images of (a) NaX zeolite (b) Montmorillonite (c) Sepiolite.....	98
Figure 7.20. SEM images of (a) NaX-M (10%) (b) NaX-M (20%) (c) NaX-S (10%) (d) NaX-S (20%).....	99
Figure 7.21. X-ray diffractogram of the NaX zeolite, Montmorillonite (M) and granulated form with montmorillonite (NaX-M).....	100
Figure 7.22. X-ray diffractogram of NaX zeolite, Sepiolite (S) and granulated form with sepiolite (NaX-S).....	100
Figure 7.23. FT-IR spectra of NaX zeolite.....	101
Figure 7.24. FT-IR spectra of the zeolites and Sepiolite.....	101
Figure 7.25. FT-IR spectra of the zeolites and Montmorillonite.....	102
Figure 7.26. Indentation of the NaX pellets.....	103
Figure 7.27. Thermogravimetry curve for NaX.....	105
Figure 7.28. Nitrogen adsorption isotherms on NaX and exchanged NaX zeolite at 77 K.....	106
Figure 7.29. SEM images of zeolites: (a) NaX (b) LiX-T (c) LiX-U (d) CaNaX-T (e) CaNaX-U (f) CeNaX-T (g) CeNaX-U.....	107
Figure 7.30. X-ray diffraction patterns of zeolites.....	109
Figure 7.31. Nitrogen adsorption isotherm on (a) Li^+ (b) Ca^{2+} (c) Ce^{3+} ion exchanged zeolites.....	111
Figure 7.32. ZLC blank response curves for (a) CH_4 -He (b) N_2 -He (c) CO_2 -He.....	114
Figure 7.33. ZLC response curves for CH_4 -NaX ($C_0=3.3\%$).....	115
Figure 7.34. ZLC response curves for CO_2 -NaX ($C_0=3.2\%$).....	116
Figure 7.35. ZLC response curves of NaX for (a) N_2 (b) CO_2 (c) CH_4	117
Figure 7.36. ZLC response curves of LiX-U for (a) N_2 (b) CO_2 (c) CH_4	118
Figure 7.37. ZLC response curves of CaNaX-U for (a) N_2 (b) CO_2 (c) CH_4	119
Figure 7.38. ZLC response curves of CeNaX-U for (a) N_2 (b) CO_2 (c) CH_4	120
Figure 7.39. Temperature dependence of micropore diffusion coefficient for (a) NaX (b) LiX-U (c) CaNaX-U (d) CeNaX-U.....	122
Figure 7.40. Van't Hoff plots showing temperature dependence of the Henry constants for (a) NaX (b) LiX-U (c) CaNaX-U (d) CeNaX-U zeolites	124

Figure 7.41. The kinetic selectivity, $S_{A/B}$, for (a) NaX (b) LiX-U (c) CaNaX-U
(d) CeNaX-U.....

127

LIST OF TABLES

<u>Table</u>	<u>Page</u>
Table 2.1. Zeolite: X	7
Table 3.1. General application of ultrasound.....	15
Table 4.1. Selected studies for ion exchange in NaX.....	28
Table 4.2. Physical properties of counter and external ions.....	30
Table 4.3. Classification of sorptive separations.....	31
Table 5.1. Classification of methods to measure the intracrystalline diffusion in zeolites.....	46
Table 5.2. Studies with Zero Length Column (ZLC) technique in literature.....	47
Table 6.1. Experimental parameters for Li ⁺ , Ca ²⁺ and Ce ³⁺ ions exchange at 50 °C and 70 °C.....	62
Table 7.1. The experimental conditions and the zeolites obtained.....	77
Table 7.2. The reaction model parameters of cation exchange at 50 °C.....	77
Table 7.3. The reaction model parameters of cation exchange at 70 °C.....	78
Table 7.4. The activation energy and thermodynamic paramaters for lithium, calcium and cerium exchange.....	88
Table 7.5. Diffusion models parameters of ion exchange 50 °C.....	92
Table 7.6. Diffusion models parameters of ion exchange 70 °C.....	93
Table 7.7. N ₂ -adsorption isotherms at 77 K for NaX zeolite and clay minerals.....	97
Table 7.8. The textural properties of the zeolite granules.....	97
Table 7.9. Vickers hardness numbers of the zeolites.....	103
Table 7.10. Losses (%) on attrition for NaX zeolite, clay minerals and pellet forms	104
Table 7.11. Textural properties of the zeolites from consecutive study.....	106
Table 7.12. Textural properties of Li ⁺ , Ca ²⁺ and Ce ³⁺ ion exchanged zeolite.....	110
Table 7.13. Kinetic and Equilibrium parameters of N ₂ , CO ₂ and CH ₄ adsorption...	121
Table 7.14. Arrhenius equation parameters for zeolites.....	123
Table 7.15. Heat of adsorption of NaX and cation exchanged NaX zeolite.....	126

CHAPTER 1

INTRODUCTION

Porous materials have attracted the attention of chemists, physicists and materials scientists because of interest in their application in separation, storage, and heterogeneous catalysis. There were basically two types of porous materials, namely, inorganic and carbon-based materials (Kitagawa et al., 2004). Zeolites are the microporous inorganic solids and extremely useful adsorbents to perform ion exchange and gas separation, which can be attributed to their high surface areas in combination with their chemical nature. They are crystalline aluminosilicates, which can be found in nature or may be produced synthetically. Zeolites are synthesized normally in the 1-10 μm particle size range as polycrystalline powders and they can be shaped into bodies such as spheres, granules and extrudates (Jasra et al., 2003).

NaX is a synthetic zeolite composed of eight sodalite cages joined through six-membered oxygen rings in a tetrahedral arrangement. It has large cavity or supercage accessible through twelve-membered oxygen rings. Inside the framework structure of X zeolite, Na ions reversibly fixed in the cavities and can be exchanged with the other positive ions with traditional ion exchange method which is the batch operation. It is the simplest method for operating ion exchange process. It can be used with either organic or inorganic media at ambient temperatures and pressures. Besides the variety of ways of an ion exchange processes, ultrasound can be also used as an alternative method.

Ultrasound is a source of high energy vibrations that produced mechanical waves with frequencies above the human hearing upper limit (18 kHz) (Kim and Kim, 2008). The sonochemistry (20 kHz - 2 MHz), power (20 kHz - 100 kHz) and diagnostic (5 MHz - GHz) ultrasound are three strands of ultrasound. Different ranges of the frequency of the sound provide diversity of the application field. Agglomeration, bleaching, catalysis, cavitation, adsorption and desorption, dispersion, homogenization, particle size reduction are some of the example for the applications. In recent years, several studies were reported for the effect of ultrasound on the mass transfer mechanisms: bulk diffusion, external (boundary layer) diffusion, intraparticle diffusion. In these studies, the ultrasound is generated by using the horn and also ultrasonic

cleaner. Rege et al. (1998) have studied the desorption of phenol from activated carbon and polymeric resin adsorbents using ultrasound. Mechanism of desorption was altered with an application of an ultrasound at 40 kHz and 1.44 MHz. They found that phenol desorption rates were enhanced with ultrasound due to an increase in diffusive transport within the pores. In another study, the effect of ultrasound was investigated on leaching process (Ji et al., 2006). Geniposide was leached from the Gardenia fruit ultrasonically. Ultrasound increased the external mass transfer coefficient and intraparticle diffusion coefficient, 1.63 and 3.25 times respectively. In the synthesis of nano-sized LiCoO₂ powders (Kim and Kim, 2008), ultrasound (20 kHz, 50 W) was very effective compared to other methods in respect to reaction time and phase purity. Ion exchange reaction between β -CoOOH and Li⁺ ions in the solution was obtained as an intermediate phase before to obtain the nanosized LiCoO₂. According to the study, ultrasonic irradiation accelerated the chemical reaction. However, the study in the literature has not expanded application of ultrasound to cation exchange.

Zeolites are excellent candidate materials for the gas adsorption. Volumetric and manometric method most widely used for gas adsorption. However, they are time consuming methods. ZLC method is relatively inexpensive method and can be used to measure the nature of the diffusion parameters, diffusion coefficient (D_c) and Henry constants (K) (Barcia et al., 2005).

The aim of this study was conducted to investigate the mechanism of the ultrasound as an alternative method on Li⁺, Ca²⁺ and Ce³⁺ ion exchanged NaX zeolite. LiX zeolite is the best adsorbent for the production of nitrogen from the air separation by adsorption process (Hutson et al., 1999). Compared with other available cations like Ca²⁺, Li⁺ ion is expensive and produced according to the custom required (Ackley et al., 2003). Ce is the most common elements of lanthanides group. But it is not produced in zeolite form as commercial. Therefore, NaX zeolite was modified with Li⁺, Ca²⁺ and Ce³⁺ ions to produce higher adsorbent productivity by enhancing the adsorption capacity and selectivity. In the ion exchange studies, the influence of the fold equivalent excess of Li⁺, Ca²⁺, Ce³⁺ ions in salt solutions according to the meq Na⁺ per g NaX zeolite, exchange time, solution temperature and methods used on ion exchange process were investigated. The kinetics of ion exchange were described by using reaction and diffusion kinetic models. Besides to pseudo second order reaction, internal and external diffusion models were fitted to experimental data. The adsorption kinetics of CH₄, CO₂, N₂ gases on NaX and Li-, Ca- and Ce- exchanged NaX zeolite were studied. To

examine the separation efficiency of ion exchanged zeolites in order to produce high concentration of methane, home made ZLC adsorption system was used with mass spectrometry.

CHAPTER 2

ZEOLITE

2.1. Zeolite Science

Most of the properties of zeolites had been described in the literature by the mid-1930's. Besides their physico-chemical properties, the basics of their structures had also been investigated. The interest of the scientific community, however, was aroused when a man now regarded as the 'founding father' of zeolite science, Richard M. Barrer, started a thorough and systematic study of the sorption of polar and non-polar gases by zeolites. He related the sorptive properties to the structural properties known from X-ray measurements. His many of the studies consist of absorption and molecular sieving properties of zeolites and many syntheses of zeolitic structures. He was among the first to propose a scheme for naming zeolites in 1945. After 1970's, the current IUPAC standart was used.

First of all, all the efforts in zeolitic synthesis were directed towards increasing the Si content, which led to the discovery of more stable high silica zeolites by the end of the 1960's. Because Al^{3+} ions at tetrahedrally co-ordinated sites were replaced by Si^{4+} , high silica frameworks were less charged. This made them less suitable for ion-exchange applications but more suitable for catalyzing reactions especially used in the petrochemical industry.

In the early 1980's, the success of the organic-additive driven synthesis discovered by Wilson et al. is a completely new class of materials, the aluminophosphate molecular sieves (Ackley et al., 2003). The absence of counterions in the pores and charges in the lattice makes them less suitable for catalysis, but all the more suitable for molecular sieving since there is no blocking by counterions.

Zeolite science is an important and progressive science. Today, there are 34 species of zeolite minerals and approximately 100 types of synthetic zeolites. Synthetic and natural zeolites are used in numerous applications in a wide variety of fields. The major use of zeolites is as ion exchangers in laundry detergents where they remove calcium and magnesium from water by exchanging it for sodium present in the zeolite.

Furthermore, zeolites are applied as adsorbents in the purification of gas streams to remove water, CO₂ and SO₂ from low-grade natural gas streams and volatile organic species, in the separation of different isomers and gas-mixtures, moreover they are applied in the clean up of radioactive waste.

2.2. Structure of Zeolite

Zeolites are group of crystalline aluminosilicates with a cage like structure of SiO₄ and AlO₄ tetrahedra bound by shared oxygen atoms prepared as microcrystalline powders, extrudates, pellets or beads. The empirical formula of zeolites may be represented as; M_{2/n}O.Al₂O₃.xSiO₂.yH₂O. Where n is the cation valence, x is the equal to or greater than 2 in this oxide formula.

The negative charge arises from the difference in formal valency of the silicon and aluminum cations will be located on one of the oxygen anions connected to an aluminum cation. The negative charges of the AlO₄ units are balanced by exchangeable cations like Na⁺, K⁺, Ca²⁺, Mg²⁺, Ce³⁺ or Fe³⁺ (Diaz et al., 2004).

The zeolite structure consists of a pore system with channels in one, two or three dimensions and additionally inner cavities may be present. The molecular sieving properties of zeolites are based on the size of these well defined openings which can be created by calcination in order to remove water of hydration. The diameters of the pores and cavities range from 3 Å to 12 Å, which coincides with the dimensions of many hydrocarbon molecules for which they are applied as adsorbents and catalysts.

The crystal structure of a zeolite consists of windows, cages and supercages. The molecules to be adsorbed reaches the cages and supercages by the windows. The cages and supercages are the cells in the crystal structure. The cages are the smaller cells than the supercages which may even contain cages as seen in Figure 2.1 (Savitz et al., 1999).

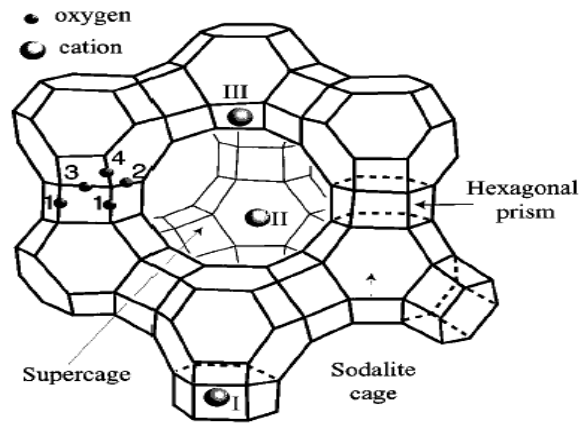


Figure 2.1. Faujasite structure showing cation sites (I, II, III) and locations of oxygen atoms (1, 2, 3, 4).

The pore size openings which can be tuned by exchange of the sodium ions against other mono-, di-, or trivalent cations allow the separation of gas mixtures, vapours or liquids by a molecular sieve effect consisting in the sorption uptake of smaller molecules and hindering of adsorption of larger molecules relate to the critical diameter of the pore opening (Buhl et al., 2004).

2.3. The Synthetic 13X (NaX or X) Zeolite

The commercial or synthetic adsorbents such as crystalline aluminosilicate zeolites, activated carbon, activated clays are used generally for the separation of gas and vapor mixtures. Aluminosilicate zeolites have pores of uniform size contrary to the other adsorbents. The NaX is a synthetic aluminosilicate zeolites composed of Si, Al, Na, and O atoms. Its chemical formula is $\text{Na}_{86}[(\text{Al}_{102})_{86}(\text{SiO}_2)_{106}]\cdot 264\text{H}_2\text{O}$. Data related to structures of X zeolites are summarized in Table 2.1.

Table 2.1. Zeolite: X
(Source: Breck, 1974)

Chemical Composition	
Typical oxide formula	: $\text{Na}_2\text{O} \cdot \text{Al}_2\text{O}_3 \cdot 2.5\text{SiO}_2 \cdot 6\text{H}_2\text{O}$
Typical unit cell contents	: $\text{Na}_{86}[(\text{AlO}_2)_{86}(\text{SiO}_2)_{106}] \cdot 264\text{H}_2\text{O}$
Variations	: $\text{Si}/\text{Al}=1$ to 1.5 and $\text{Na}/\text{Al}=0.7$ to 1.1
Crystallographic Data	
Symmetry	: Cubic
Density	: 1.93g/cc
Unit cell volume	: 15,362-15,670 Å ³
Structural Properties	
Framework	: Truncated octahedra, β cages, linked tetrahedrally through D6R2s in arrangement. Contains eight cavities, ~13 Å in diameter in each cell
Void Volume	: 0.50 cc/cc
Framework density	: 1.31 g/cc
Channel system	: Three-dimensional
Hydrated free apertures	: 12-ring, 7.4 Å, and 6-ring, 2.2 Å
Dehydrated free apertures	: 7.4 Å
Largest molecule adsorbed	: $(\text{C}_4\text{H}_9)_3\text{N}$
Kinetic diameter	: 8.1Å

The zeolite X has tetrahedral crystal structure which is composed of β-cages and double six-rings (D6R) as seen in Figure 2.2 (Fujimoto, 1997). The distance between each center of D6R is 0.88 nm.

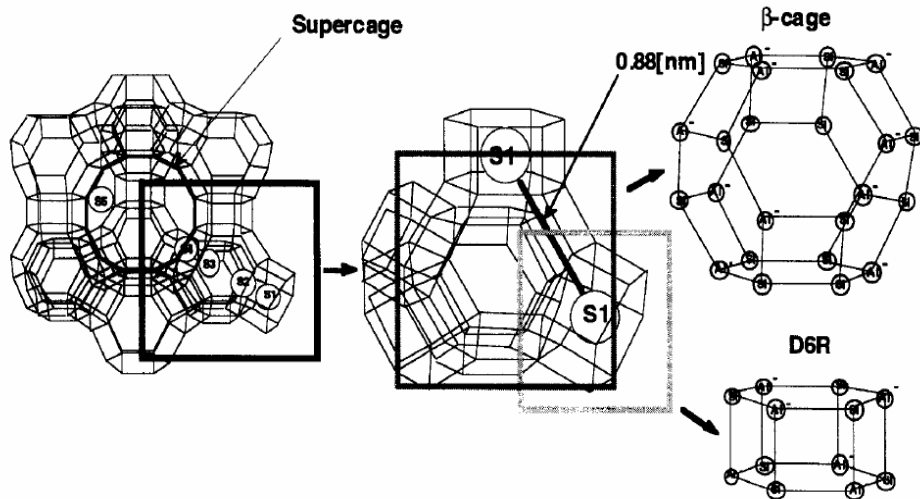


Figure 2.2. Crystal structure of NaX zeolite.
(Source: Fujimoto, 1997)

The positions of cation sites are seen clearly from the Figure 2.3. Cations in SI position are in a more symmetric environment in the center of double six-rings. The SII cation position is located in the supercage and is coordinated to three oxygen atoms of the six-ring window to the sodalite cage while the SI' position is in the sodalite cage. The SIII cations are located in the super cages at the entrance of zeolite cage with eight-membered ring and hinder the passage of incoming molecule (Chatterjee, 2004).

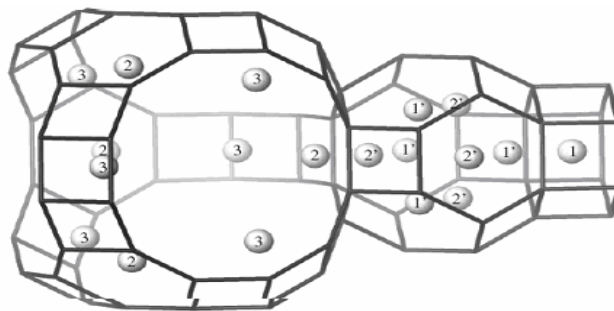
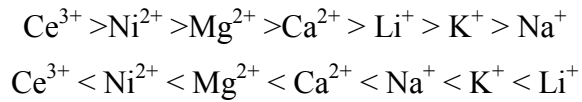


Figure 2.3. Cation sites in NaX zeolite (the numbers refer to cation sites).
(Source: Broach, 2010)

The cation prefers to migrate from higher energy to a stable lower energy and depending on solely on the local architecture and nature of cation (Chatterjee, 2004). The stabilization energy, which depends on the differences between neutral and ionic ground states, for the cations in SI and SII are in the order, respectively ;



Na^+ is the least stable when placed in SI site and hence may have more mobility. The Li^+ in case of SII shows most stability. However, the cation migration is least feasible for Li cation due to having higher hydrated radius compared to the Na^+ ion ($r_{\text{hNa}}=3.58$ $r_{\text{hLi}}=3.82$). The trivalent cation like Ce^{3+} , which was most stable in the SI site, is least stable in SII site.

2.4. The Important Characteristics and Application of Zeolites

Zeolites have a number of characteristic properties and are important for commercial applications which are summarized as follows;

- They are capable of selective ion exchange and can be used as a molecular sieve due to having uniform window (or pore) size. The molecules can be adsorbed through the windows on its large internal area.
- Zeolite can be used as a solid acid catalyst. It can function as a strong acid when the hydration has substituted a hydrogen for the additional valence electron, or isoelectronic exchange with the aluminum occurs.
- Zeolite is metastable. That is, it is stable as long as it is at a suitable temperature and pH.

Because of having important characteristics, zeolites can be adapted for a variety of uses such as;

- Industrial products (Absorbents for oil and spills, gas separations)
- Radioactive waste (Site remediation/decontamination)
- Water treatment (Water filtration, heavy metal removal, swimming pools)
- Wastewater Treatment (Ammonia removal in municipal sludge/wastewater, heavy metal removal, septic leach fields)
- Aquaculture (Ammonia filtration in fish hatcheries, biofilter media)
- Agriculture (Odor control, confined animal environmental control, livestock feed additives)

- Horticulture (Nurseries, greenhouses, floriculture, vegetables/herbs, foliage, tree and shrub transplanting, medium for hydroponic growing)
- Household products (odor control, pet odor control)

2.5. The Granulation Form of Zeolite

The zeolite crystals to be used in adsorption processing are inconvenient for practical use and must be formed into agglomerates to provide high physical strength and attrition resistance. The zeolite powder into pellets or granulation form is commercially done using inorganic binder generally natural clays such as smectite, attapulgite and kaolin to the extent of 15-20 wt% of the zeolite. After that, they are subjected to high-temperature (> 823 K) treatment to destroy the surface area and activity of the clay during the process. Zeolite structure becomes durable to the mechanical and thermal agents after the heat treatment. By this way, meso/macropores are created in a pellet so that modifying the diffusion characteristics of the sorbate molecules. As a result, porous structure are observed as macro and micropores shown in Figure 2.4.

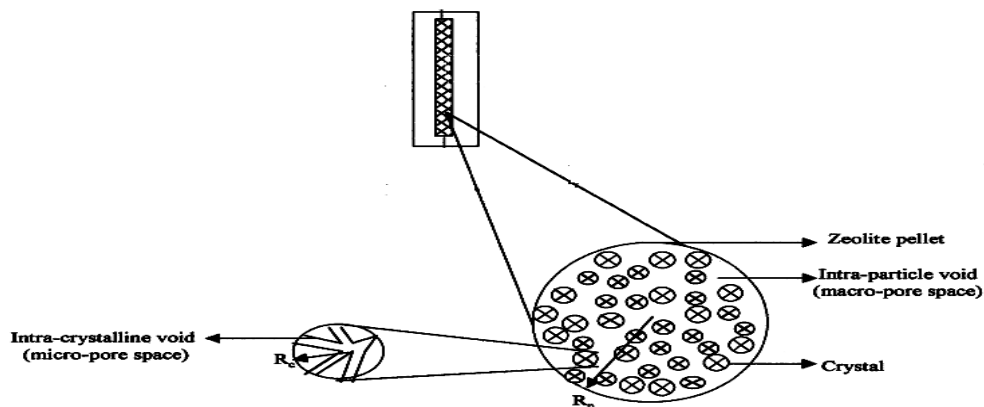


Figure 2.4. Schematic representation of a biporous particle.
(Source: Gupta et al., 2004)

The use of zeolite conformed in the shape of granules is becoming more common because conformation densifies the material and makes it more homogeneous in terms of size and shape and facilitates manipulation. During granulation, clay type binders consist of substantial amounts of group 1a and 1b elements which are mobile

nonframework cations in clay structure and can modify the acidity of the zeolites. The zeolite strong acid sites can be decreased with the presence of binder as a result of solid ion exchange between zeolite protons and clay sodium. Thereby, binders influence and modify the transfer activity, metal/acid site balance and diffusion of sorbate during granulation. That is, selection of binders are important and can be selected according to process. For example, when alumina is used as a binder for zeolites, new acid sites due to the migration and insertion of Al cation in the zeolite framework occur. This migration enhance the acidity of the zeolites. So, having information on the influence of the binder on sorption properties of the zeolite granules are very important (Jasra et al., 2003).

The zeolite can be also formed into granule form without using binder by hot pressing techniques. When subjected to high pressures with an elevated temperature, the zeolite crystal may self-bond into a 100 % zeolite granule. However, it is obtained under laboratory applications, not achieved extensive use in industrial.

2.5.1. Structure and Properties of Montmorillonite and Sepiolite Minerals

Sepiolite mineral is porous, lightweight, non-swelling fibrous hydrated magnesium silicate. It may resemble the bones of the cuttlefish *Sepia*, from which the name derives. Unlike other clays, sepiolite is not a layered phyllosilicate. Its structure can be described as a quincunx (an arrangement of five objects, so placed that four occupy the corners and the fifth the centre of a square or rectangle) of talc-type sheets separated by paralel channels represented in Figure 2.5. This chain-like structure produces needle-like particles instead of plate-like particles. Sepiolite has the highest surface area about $300 \text{ m}^2 \text{ g}^{-1}$ of all the clay minerals, also it includes high density of silanol groups (-SiOH) which explains hydrophilicity of this clay. The cation exchange capacity of this clay is very low because the silicate lattice has not a significant negative charge. It has high porosity and large void space due to loosely packed and porous aggregates with extensive capillary. These properties provide the remarkable adsorptive feature to the sepiolite.

The chemical composition and structure of sepiolite having high surface area and porosity are responsible for the good adsorbent properties towards polar molecules

(e.g. water, ammonia, amines, aldehydes, etc.) in both gas and aqueous phase (Rodriguez-Reinoso, 2001).

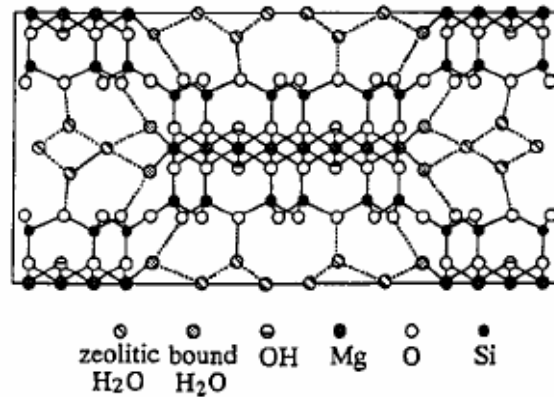


Figure 2.5. A schematic representation of sepiolite.
(Source: Sandi et al., 2002)

Montmorillonite mineral, a member of the smectite family, is based on a hydroxyl-aluminosilicate framework and mainly composed of plate-like particles and also having slit-shaped pores (Mounts, 1981; Tsai et al., 2002). The individual layers are held together with Van der Waals attractive forces, hydrogen bonding or weak electrostatic attraction (Rouquerol et al., 1999). The structure of 2:1 type montmorillonite is represented in Figure 2.6. Using montmorillonite in this study include industrially important mineral, Ca, which is the dominant exchangeable cation (Murray, 2000).

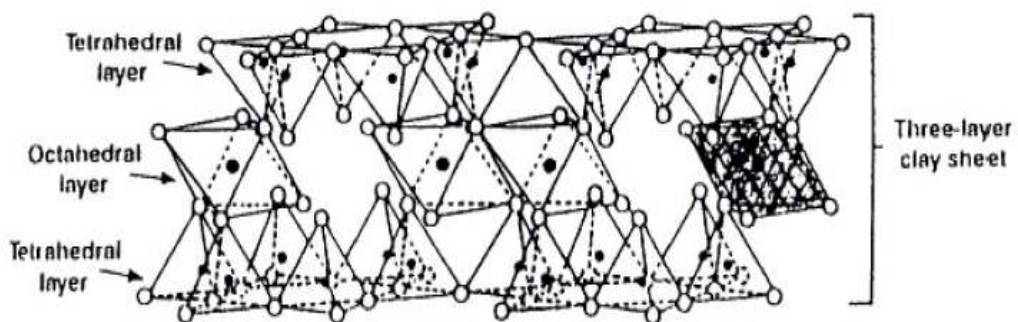


Figure 2.6. The structure of 2:1 type montmorillonite.

In most applications, uses of montmorillonite are the consequence of its properties such as ion exchange, plasticity, swelling, density, compaction, having higher surface area and their adsorption capacity (Bala et al., 2000).

CHAPTER 3

ULTRASOUND

Ultrasound is a source of high energy vibrations that produced mechanical waves with frequencies above the human hearing upper limit (18 kHz) that has potential for promoting many steps in an analysis (Kim and Kim, 2008). The sonochemistry, power and diagnostic ultrasound are three strands in ultrasound given in Figure 3.1.

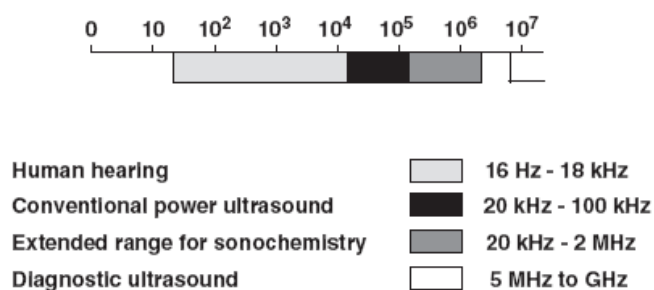


Figure 3.1. Frequency ranges of sound.

Each of them with different ranges of the frequency of the sound provides diversity of the application field. Agglomeration, bleaching, catalysis, cavitation, adsorption and desorption, dispersion, homogenization, particle size reduction are some of the example for the application. Detail application of ultrasound was given in Table 3.1.

Table 3.1. General application of ultrasound

• Acceleration	• Deagglomeration	• Homogenization
• Agglomeration	• Deflocculation	• Mixing
• Agitation	• Degassing	• Particle size reduction
• Atomization	• Dehydration	• Separation
• Bleaching	• Disintegration	• Solids processing
• Grinding	• Dispersion	• Sonocatalysis
• Blending	• Dissociation	• Sonochemistry
• Catalysis	• Emulsification	• Sonoluminescence
• Cavitation	• Extraction	• Surface processing
• Cleaning	• Cutting	• Suspension
• Compaction	• Fluidization	• Tissue disruption

In recent years, several studies were reported for the effect of ultrasound on the mass transfer mechanisms: bulk diffusion, external (boundary layer) diffusion, intraparticle diffusion. In these studies, the ultrasound is generated by using the horn and also ultrasonic cleaner. Rege et al. (1998) have studied the desorption of phenol from activated carbon and polymeric resin adsorbents using ultrasound. Mechanism of desorption was altered with an application of an ultrasound at 40 kHz and 1.44 MHz. They found that phenol desorption rates were enhanced with ultrasound due to an increase in diffusive transport within the pores. In another study, the effect of ultrasound was investigated on the leaching process (Ji et al., 2006). Geniposide was leached from the Gardenia fruit ultrasonically. Ultrasound increased the external mass transfer coefficient and intraparticle diffusion coefficient, 1.63 and 3.25 times respectively. In the degradation of acetic acid Findik et al. (2006), used ultrasound and found that degradation rate increases up to 0.2 W power with 60 kHz frequency of ultrasound to minimize the energy requirement for treatment. In the synthesis of nano-sized LiCoO₂ powders (Kim and Kim, 2008), ultrasound (20 kHz, 50 W) was very effective compared to other methods in respect to reaction time and phase purity. Ion exchange reaction between β -CoOOH and Li⁺ ions in the solution was obtained as an intermediate phase before to obtain the nanosized LiCoO₂. According to the study, ultrasonic irradiation accelerated the chemical reaction. However, the study in the literature has not expanded application of ultrasound to cation exchange.

3.1. Physical Mechanisms of Ultrasound

The possible physical mechanisms of ultrasound can affect the ion exchange process and results in mass transfer enhancement given below (Klima, 2011);

- movement of liquid due to acoustic streaming
- microstreaming due to cavitation
- formation of microjets due to collapse of cavitation bubble;
- shock waves

The formation of microjets, shock waves and microstreaming results from cavitation is the most effective process for decreasing boundary layer thickness under 1 μm than non cavitating effect because of acoustic streaming.

3.1.1. Acoustic Streaming

Acoustic streaming is the movement of the liquid promoted by sonic wave resulted in non cavitation effect (Hamdaoui and Naffrechoux, 2007). Part of ultrasonic energy is absorbed while ultrasound passes through a liquid which is related with the transfer of mechanical momentum from the passing ultrasound to the fluid. As a result of this, radiation force, $F_{rad.}$, occurs (Klima, 2011);

$$F(x, y, z) = \frac{\alpha}{2\rho \cdot c^2} |p_A(x, y, z)|^2 \quad (3.1)$$

where ρ is the fluid density, c is the speed of sound in the fluid, p_A is the amplitude of ultrasonic pressure, α is the absorption coefficient. The radiation force is proportional to amount of absorbed ultrasonic energy. The solution movement depending on the shape of vessel is called as acoustic streaming. This action may enhance the mass transfer in the process.

The most of the ultrasonic energy is absorbed by cavitation in low frequency ultrasound like 20 kHz which depends on intensity. The absorption coefficient depends on intensity. It becomes high when amplitude of ultrasonic pressure (p_A) is higher than cavitation threshold therefore cavitation takes place. On the other hand, the absorption coefficient becomes low when p_A is lower than cavitation threshold and no cavitation

occur. For high-frequency ultrasound of low intensity, absorption is a consequence of fluid viscosity and the absorption coefficient is a material constant which is depending on frequency not on ultrasonic power (Klima, 2011).

3.1.2. Microstreaming due to Cavitation

Cavitating ultrasound causes to acoustic wave which creates micro bubbles. Mutual interaction of oscillating and collapsing of millions of micro bubbles (or cavities) generates an intense cavitation which is rapid formation and expand during the negative pressure excursion and implode violently during the positive excursion. Implosive collapse of these bubbles caused to jet fluid on or near adsorbent surface at speeds 400 km/h (Castro and Capote, 2007). Not only high speed microjets which is observed in heterogeneous solution (when solid particle included) but also high pressure shock waves in the liquid as well as elevated pressures and temperatures due to adiabatic heating of gases and vapours at the implosion sites are produced after collapsing cavitating bubbles (Figure 3.2).

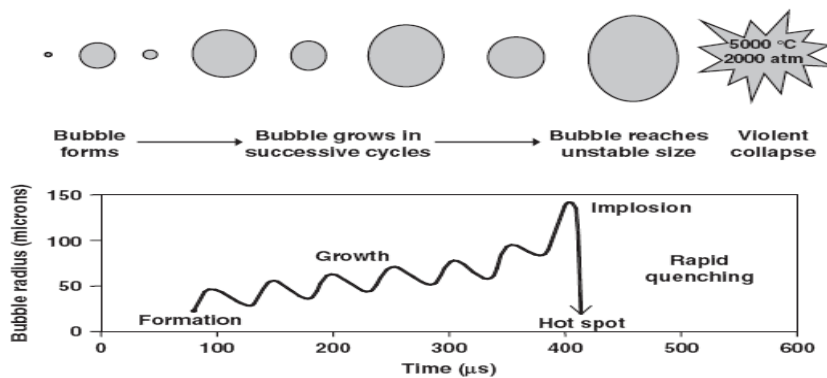


Figure 3.2. Successive growth cycle and bubble collapse.
(Source: Castro and Capote, 2007)

The ultrasonic power and frequency are the important parameters to provide the acoustic energy through the liquid and cavitation bubbles. When a large amount of ultrasonic power was used for a system, acoustic energy can be hindered through liquid by implosive collapse of bubbles. At higher frequencies, cavitation bubbles become initially difficult and it also affects the threshold intensity (Castro and Capote, 2007). As shown in Figure 3.3, the threshold for aerated water is lower than gas-free water and the

threshold intensity increases with increase in frequency. For this reason, frequency should be used in the range of 20-50 kHz to provide efficiency in ultrasound.

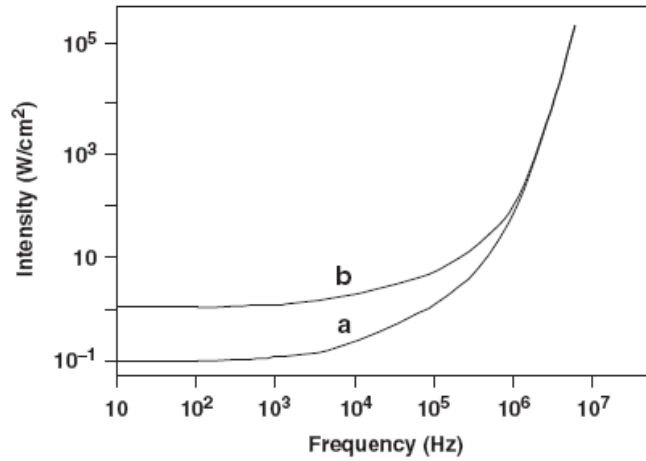


Figure 3.3. Variation of the threshold intensity with frequency (a) in aerated (b) in air-free water (Source: Castro and Capote, 2007).

3.1.3. Microjets

The presence of the solid wall (adsorbent) causes to the disturbance of spherical symmetry of the collapse that bubble develops a liquid jet directed towards the wall of the adsorbent (Plesset and Chapman, 1971; Klima, 2011). The formation of the jet and its shape was predicted theoretically by Plesset and Chapman and recorded experimentally by Lauterborn and Bolle by high-speed camera (Klima, 2011). The jet develops so early in the bubble collapse thus compressibility effects in the liquid and the vapour are not important. Microjets are able not only to transfer new material to the adsorbent but also remove dissolved products from it (Klima, 2011).

The velocity of jet can be scaled by $(\Delta p/\rho)^{1/2}$ where ρ is the density of the fluid and Δp is the difference between the ambient fluid pressure and the pressure in the cavity (Plesset and Chapman, 1971).

3.1.4. Shock Waves

Cavitation bubble acts as a source of waves spreading into the liquid. High pressure can be formed while the violent bubble collapse, which is called shock wave. Effect of shock waves is one of the possible mechanisms of corrosion of solid materials by cavitation.

High speed micro-jets, high pressure shock waves produced by acoustic cavitation and acoustic vortex microstreaming within porous solids and solid-liquid interface produce the hydrodynamical phenomena (non-thermal effect). When hot spots forming as well as by heating of the medium occur with the bubble cavitating, the thermal effect is seen (Hamdaoui and Naffrechoux, 2007).

3.2. Cavitation Phenomenon Influencing with Factors

Factors such as gas and particulate matter, frequency, temperature, intensity can be adjusted for specific purposes.

- ***Gas and particulate matter***

Cavitation occurs approximately 1500 atm. However, in the presence of weak spots in the liquid reduce its tensile strength therefore cavitation occurs at lower values (< 20 atm). Weak spots is the presence of gas molecules in the liquid. This means that gas content of a liquid lowers the cavitation threshold comparing to the degassing of a liquid.

- ***External (applied) pressure***

The external pressure increased raises the rarefaction pressure which is required to initiate cavitation. Suspended gas molecules are dissolved with application of external pressures and decreased the threshold of cavitation.

- ***Solvent viscosity***

The natural cohesive forces act in the liquid and raise the cavitation threshold. Viscosity of liquid increases these forces. Negative pressure in the expansion or rarefaction cycle must overcome the natural cohesive forces.

- ***Solvent surface tension***

Cavitation requires the formation of a liquid–gas interface. Thus, one might expect the use of a solvent of low surface energy per unit area to lower the cavitation threshold. The addition of a surfactant to an aqueous solution also facilitates cavitation.

- ***Frequency***

Producing cavitation bubbles during the available time will be increasingly difficult when frequency increases and this gives rise to increase sound intensities (*i.e.* greater amplitudes). Also more power is required at a higher frequency if the same cavitation effects are to be maintained.

- ***Temperature***

In general, the cavitation threshold increases with decreasing temperature because of increasing in either the surface tension or viscosity of the liquid as the temperature decreasing in the liquid vapour pressure. Increasing the temperature facilitates cavitation at a lower acoustic intensity. Because vapor pressure increases with heating the liquid.

- ***Intensity***

The sonication intensity is directly proportional to the square of the vibration amplitude of the ultrasonic source. When amplitude is increased, bubbles may grow so large on rarefaction that result in inadequate time for collapse.

3.3. Types of Ultrasound Devices

There are three main types of ultrasonic (US) sources consisting of gas driven, liquid driven and electromechanical ultrasonic sources. Gas driven source is used mainly in whistles and sirens. Liquid-driven transducers are useful in homogenization and efficient mixing. Electromechanical transducers are used in analytical devices, even when homogenization and efficient mixing are required. Electromechanical transducers are based on the piezoelectric and magnetostrictive effects. Piezoelectric transducer is the most commonly used in power bath and probe-type sonicators.

The laboratory ultrasonic apparatus are namely, whistle reactors, ultrasonic cleaning baths, probes and cup-horn devices. Analytical chemists use mainly cleaning baths and probes both of which are usually operated at a fixed frequency; 20 kHz for common probe systems and 40 kHz for baths.

3.3.1. The Ultrasonic Cleaning Bath

So many analytical chemists first use cleaning baths because of inexpensive piece of ultrasonic equipment available. Cleaning bath generally consists of a stainless steel tank with transducers clamped to its base, as shown in Figure 3.4.

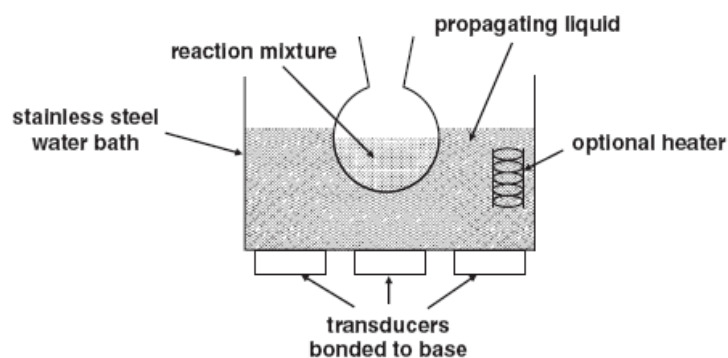


Figure 3.4. A typical ultrasonic cleaning bath.

An ultrasonic bath, which is a low-intensity device, uses a power intensity about $1-5 \text{ W/cm}^2$ at the transducer in modern piezoelectric transducers and operates at a frequency of 40 kHz. Although the cleaning bath is the piece of ultrasonic equipment and used by chemists, it is not most effective. The some advantages of using an ultrasonic bath are as follows:

- The ultrasonic bath is the most widely available laboratory source of ultrasonic radiation.
- Small cleaning baths are inexpensive.
- The acoustic field is fairly evenly distributed throughout the bath liquid.
- The ultrasonic bath is used at high or low pressures or even an inert atmosphere.

On the other hand, the disadvantages of using an ultrasonic bath can be summarized as follows:

- The amount of power dissipated from the bath into the system is usually not very large less than 5 W/cm^2 .
- The amount of power actually delivered will depend on the bath size
- Maintaining the temperature in the bath is difficult unless the ultrasonic device is furnished with some automatic thermal control.
- Cleaning baths have no controlled adjustable power
- The decline in power with time and the lack of uniformity in the transmission of ultrasound.

3.3.2. Ultrasonic Probe

Ultrasound is a source of high energy vibrations that has potential for promoting many steps in an analysis. It has broad range from 20 kHz to the GHz. The ultrasonic power supply converts 50/60 Hz line voltage to high frequency electrical energy. This high frequency electrical energy is transmitted to the piezoelectric transducer within the converter, where it is changed to mechanical vibrations. The vibrations from the converter are intensified by the probe, creating pressure waves in the liquid. This action forms millions of microscopic bubbles (cavities).



Figure 3.5. The illustration of ultrasonic processor.

Ultrasonic probes as shown in Figure 3.5 are not subjected to any exhaustion restrictions so they are preferred in order to use in analytical chemistry comparing to ultrasonic baths. They can be designed for specific purposes. Some variables including the direction, amplitude and frequency of the vibrations at the point of application can

be adjusted to provide maximum effects on the process. Ultrasonic probe consists of the following components:

- A *power supply* to convert mains electrical power to the frequency, voltage and current required by the ultrasound system.
- A *transducer* (or *converter*) to convert electrical power into mechanical vibrations.
- A *transducer cover* to protect the user from high voltages and the transducer from accidental damage. The ceramic discs, electrodes and electrical connections are protected with this cover.
- *Piezoelectric ceramic discs*, which are the heart of the transducer. As a voltage is applied, the discs expand and contract along the transducer axis. It can be provided with *electrodes* which are located on both sides of each ceramic disc. Several discs (usually 2 or 4) are used to increase the movement produced.
- A *machine screw* (normally high-tensile steel) clamps the ceramic discs together in the centre of the transducer
- The *front-end* of the transducer (titanium or high-strength aluminium alloy) is used to transmit its motion to the rest of the system.
- A *back-block* (usually steel or titanium) that provides balance the motion of the transducer which is behind the ceramic discs.
- An optional *booster* (titanium or high-strength aluminium alloy) fitted between the transducer and the ultrasonic tool. It usually increases the vibration amplitude.
- The *extender*, which is not an essential part of the device as it is only required in order to reach into narrow vessels. They consist of simple cylinders, solid or tapped for a tip.
- The *sonotrode* comes in all shapes and sizes and can be constructed with steel, stainless steel, titanium alloy, ceramics according to the application. This is an amplifying element also known as *horn* or *probe* and fitted with a *tip*. Tip is the radiating surface of the horn and irradiates acoustic energy outwards to do work which can be either removable or integrated to the output element.

The probe or sonic horn is driven by the transducer and ultrasound enters system via the probe tip. The intensity of sonication (the vibrational amplitude of the tip) can be controlled by altering the power input to the transducer. Figure 3.6 shows the ultrasonic horn immersed axially to a cylindrical cell.

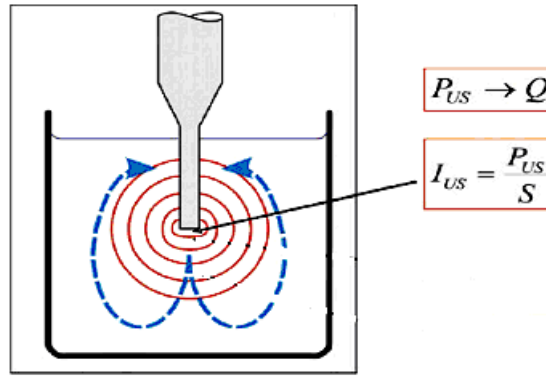


Figure 3.6. Ultrasonic horn immersed to the vessel.
(Source: Klima, 2011)

All the ultrasonic energy enters to the system through the tip of the horn. I_{US} is the average intensity of ultrasound at the horn tip determined by dividing the ultrasonic power, P_{US} , entering the system by the area S of the horn tip.

There are alternative ways to control the power input to a system depending on the probe design including length, shape and gain. The *shape* of the horn greatly affects its performance. Figure 3.7 shows different horn shapes. Uniform horns are fashioned in the shape of a uniform cylinder (e.g. 13 cm in length) subjected to an ultrasonic vibration (e.g. 20 kHz) at one end that produces an exactly identical vibration at the other end.

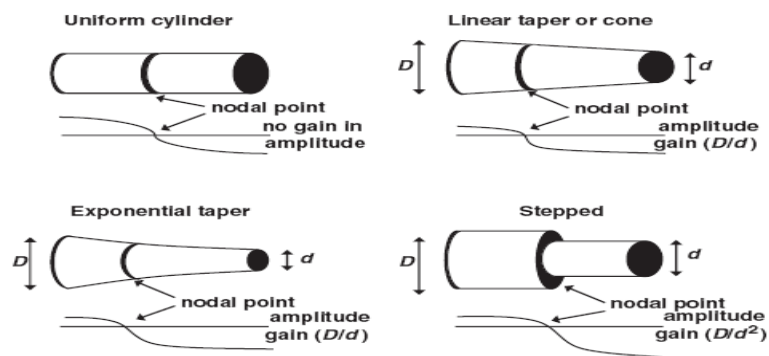


Figure 3.7. Shapes of the acoustic horns.

Advantages and disadvantages of ultrasonic probes

Some advantages of using an ultrasound probe are as follows:

- Ultrasonic horn delivers the ultrasonic power which is directly related to the magnitude of vibration of the tip.
- Bulk mixing is provided from the tip of the probe when dipped in a system since energy losses during the transfer of ultrasound through the reaction vessel walls are eliminated.
- Pulse facility allows the operator adequate time for “cooling” between pulses.
- Variety of frequencies, power ranges, detachable metal probes of different horn and tip diameters and other accessories from a number of manufacturers are operated.

Besides the advantages of ultrasonic probe, some disadvantages of ultrasonic probes includes as follows:

- Optimum performance is obtained at a fixed frequency and most commercial probe systems such a frequency is 20 kHz. However, the power dissipation at overtones like 40 or 80 kHz is very much reduced. For such system individual amplifier should be used.
- There is a problem over accurate temperature control like ultrasonic bath unless some precautions are taken.
- Cavitation is the source of the main effects of ultrasound. However, it is also the origin of a common problem with probe systems. There are two unwanted side effects associated with erosion. First one, metal particles erode from the tip and contaminate the system. The second one, physical shortening of the horn reduces efficiency.
- Multiple probes should be used to cope with for larger volumes.

CHAPTER 4

ION EXCHANGE

Ion exchange is the equivalent exchange of ions between ionised species located in different phases which includes at least one ion exchanger. The structure of the ion exchanger has ability to ion exchange which are grouped according to their functionality and the physical properties of the support matrix. Cation and anion exchangers are classified in terms of their ability to exchange positively or negatively charged species. The media of an ion exchange has a greater affinity for certain ionic species than for others under certain conditions. This property provides perfect separation of selected ions from others (Braun et al., 2002). In addition to being ion exchangers, they can also act as sorbents. The ions in the solution are concentrated on both the surface and in the pores of the ion exchange media (sorbents). Due to the electrostatic attraction between the ions in solution and the fixed ionic groups on the ion exchange media, the sorption equilibrium obtained.

NaX zeolite is composed of a large number of ionic sites and can be exchanged into alkali metal, alkaline earth or transition elements to generate the desired adsorbent materials for a given separation or purification.

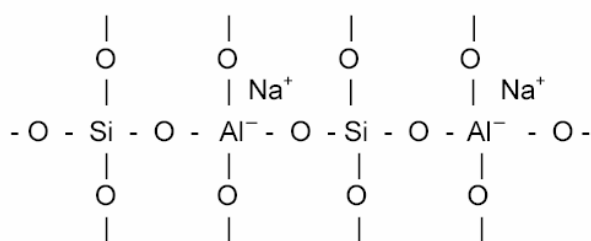
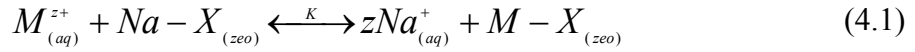


Figure 4.1. Two-dimensional representation of the zeolite structure.

As seen from the Figure 4.1, zeolite has negative charges compensated by Na^+ ions. Na^+ ions can move within the free space of the zeolite matrix and can be replaced by equivalent amount of the counter ions (e.g., M^{Z+} : Li^+ , K^+ , Mg^{2+} , Ca^{2+} , Ce^{3+}) from the solution according to the following equation:



where K is the rate constant of the ion exchange reaction defined as the ratio of rate of forward to that of reverse reaction. As seen from the Figure 4.2, monovalent lithium and divalent calcium ions actually must displace one and two sodium ions, respectively.

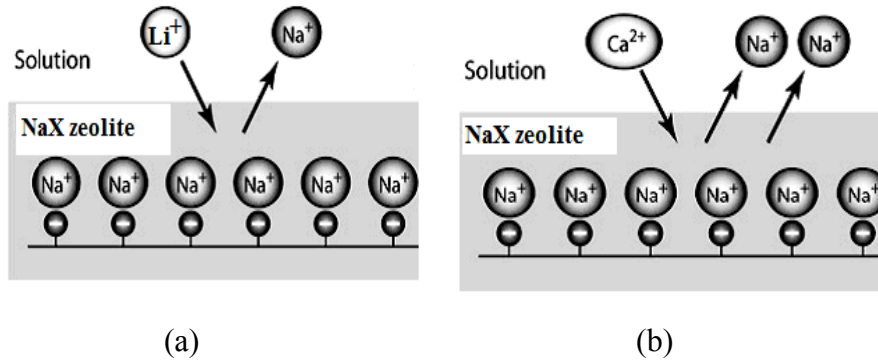


Figure 4.2. Equivalent character of ion exchange for (a) $Li_{aq}^{+} + Na - X_{(zeo)} = Na_{(aq)}^{+} + Li - X_{(zeo)}$ (b) $Ca_{aq}^{2+} + Na - X_{(zeo)} = 2Na_{(aq)}^{+} + Ca - X_{(zeo)}$ (Source: Zagorodni, 2007).

The nature of ion species, size and both hydrated and anhydrous ion charge, the concentration of the ion species in solution, the temperature of the solution and the structural characteristics of the particular zeolite affect the behaviour of the ion exchange.

The success of ion exchange typically increases with an increasing charge. The hydrated radius is decreased with increasing atomic number and charge of the exchanging cation. The affinity of sodium exchange for X zeolite given below.



Literature review for ion exchange performed generally with traditional method was given in Table 4.1.

Table 4.1. Selected studies for ion exchange in NaX

Studies	Counter ions (the amount exchanged %)	Ion exchanger/ Adsorbent	Exchange conditions	Reference
Water softening by combination of ultrasound and ion exchange	Ca ²⁺ , Mg ²⁺	Co-polymer of styrene and divinylbenzene	Combination of ultrasound (20 kHz) and ion exchange to reduce the hardness of water	Entezari and Tahmasbi, 2009
Kinetics of alkylation of phenol with methanol over Ce-exchanged NaX zeolite	Ce ³⁺ (1.74-10.43)	NaX	At boiling point for 16h.	Barman et al., 2006
CO ₂ adsorption in Y and X zeolites modified by alkali metal cation exchange	Li ⁺ (76), K ⁺ (88.7) Rb ⁺ (75.4) Cs ⁺ (55)	NaY, NaX	Four times exchanges at 77°C for 5h	Walton et al., 2006
Cerium uptake by zeolite A synthesized from natural clinoptilolite tuffs	Ce ³⁺	Zeolite A	At room temperature	Faghihian et al., 2005
Li-X type zeolite mediated Michael addition of thiols to cyclic enones and its application in the synthesis of 13-thiaprostaglandins	Cs ⁺ (52) K ⁺ (88) Li ⁺ (75)	NaX	Six times exchanges at 80°C for 6 hours	Shinde et al., 2004
Hydrothermal stability of the novel zeolite type LSX in comparison to the traditional 13X modification	Li ⁺ (74) Na ⁺ (100) K ⁺ (85) Ca ²⁺ (98) Ba ²⁺ (93)	LSX, 13X	Three fold ion exchanged at room temperature for 5 hours	Buhl et al., 2003
Li ⁺ - and H ⁺ - exchanged low silica X zeolite as selective nitrogen adsorbent for air separation	Li ⁺ , H ⁺	LSX	Five times exchanges at 100°C for 1 hour	Kim, 2003
Thermodynamics of nitrogen and oxygen sorption on zeolites LiLSX and CaA	Li ⁺ , Ca ²⁺	NaLSX, A zeolite	Five and four static exchanges of Li ⁺ ion and Ca ²⁺ ion with fourfold excess at 80°C, respectively.	Shen et al., 2001

4.1. Ion Exchange Isotherms for NaX Zeolite

The exchange isotherms show equivalent fraction of the counter ion in the solid (zeolite) phase (A_z) versus equivalent fraction in the solution (A_s) phase at equilibrium and indicate whether zeolite is the favourable or not.

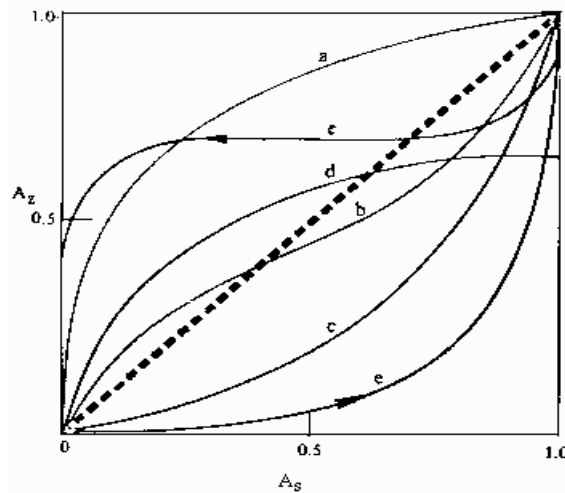


Figure 4.3. Types of ion exchange isotherms.
(Source: Breck, 1974)

There are five types of isotherms given in Figure 4.3. Type (a) with a selectivity for the entering cation over the counter ion in zeolite; type (b) in which the entering cation shows a selectivity reversal with an increasing equivalent fraction in solution; type (c) with a selectivity for the exiting cation over the counter ion of the zeolite; type (d) in which exchange is not completed although the entering cation is initially preferred, and type (e) in which hysteresis effects may result from the formation of two zeolite phases. According to the Breck's arrangement isotherms indicate whether or not the exchange cation in solution is preferably exchanged by zeolite. The selectivity generally changes with degree of exchange. Higher exchange capacity is observed for zeolites having low Si/Al ratio.

Table 4.2. Physical properties of counter and external ions.

Cation	Ionic/hydrated radius /Å	Hydrated radius per charge	Isotherm type
Na ⁺	0.95/3.58	3.58	----
Li ⁺	0.69/3.80	3.80	C
Ca ²⁺	0.99/4.12	2.06	A
Ce ³⁺	1.05/9.0	3.00	D

According to the Table 4.2, calcium is the most favorable cation for ion exchange in NaX zeolite. The replacement of Na⁺ ion by Li⁺ ion is difficult due to higher hydrated radius of Li⁺ ion than Na⁺ ion.

4.2. Sorption: Ion Exchange & Adsorption

According to the Inglezakis and Poulopoulos (2006), sorption is used to describe every type of capture of a substance from the external surface of solids, liquids, or mesomorphs as well as from the internal surface of porous solids or liquids. McBain proposed the term sorption for absorption and adsorption (Inglezakis and Poulopoulos, 2006; Dabrowski, 2001). Adsorption includes the uptake of gaseous or liquid components of mixtures from the external and/or internal surface of porous solids. It is also called separation process during bonding of ions and molecules of one phase is transferred onto the surface of another phase. However, when the species of the adsorbate travel between the atoms, ions or the molecules of the adsorbent, absorption takes place. This phenomena discriminates absorption from the adsorption that takes place on the interface. According to the Levan and Carta (2007), ion exchange and adsorption join in regard to unified treatment application in batch process and they can be classified together as sorption since mass transfer from a fluid to a solid phase is common in both processes and basically diffusion processes. There are three types of sorption grouped according to the type of bonding:

- *Physical sorption*: There is no exchange of electrons in physical sorption and independent of the electronic properties of the molecules involved. This type of adsorption is stable only at temperatures below about 150 °C (Braun et al.,2002). Because the heat of adsorption or activation energy is low.

- *Chemical sorption*: Chemisorption involves an exchange of electrons between specific surface sites and solute molecules. Therefore chemical bond formation occurs. Much stronger adsorption energy is seen compared to physical adsorption. This results in more stable bond at higher temperatures.
- *Electrostatic sorption (ion exchange)*: Coulombic attractive forces is seen between ions and charged functional groups and commonly classified as ion exchange.

However, ion exchange is a stoichiometric process in contrast to sorption. This means that for every ion in the ion-exchange process is removed as the equivalent fraction then another equivalent fraction ion is released into the solution. Table 4.3 shows the type of interaction (adsorption and ion exchange) with sorption operations. Some other similar separations are also included.

Table 4.3. Classification of sorptive separations.

Type of interaction	Basis for separation	Examples
Adsorption	Equilibrium	Numerous purification and recovery processes for gases and liquids Activated carbon-based applications Desiccation using silica gels, aluminas, and zeolites
	Rate Molecular sieving	Oxygen from air by PSA using 5A zeolite Nitrogen from air by PSA using carbon molecular sieve Separation on <i>n</i> - and <i>iso</i> -parafins using 5A zeolite Separation of xylenes using zeolite
Ion exchange (electrostatic)	Equilibrium	Deionization Water softening Rare earth separations Recovery and separation of pharmaceuticals (e.g., amino acids, proteins)
Ligand exchange	Equilibrium	Chromatographic separation of glucose-fructose mixtures with Ca-form resins Removal of heavy metals with chelating resins
Solubility	Equilibrium	Affinity chromatography Partition chromatography
None (purely steric)	Equilibrium partitioning in pores	Size exclusion or gel permeation chromatography

4.2.1. Ion Exchange Kinetics

Adsorption and ion exchange can be achieved by sorbent-fluid contact in batch equipment. They involve the transfer of solute and resulting equilibrium between a fluid phase and particle. The equilibrium isotherms and diffusion rate can be easily measured with batch runs. The rate of kinetics is governed by several factors: solution concentration, the molecular size of the ions exchanged, the size of the pores in the sorbent structure, the extent of agitation influence the kinetic rate (DeSilva, 1999).

The rate of ion exchange may be determined by one or more of several distinct mechanisms (Bekkum et al., 2001). Because ion exchange is not only a chemical process, it is also in principle a redistribution of ions between two phases by diffusion (Inglezakis and Pouloupoulos, 2006). At this point, chemical factors are less significant or even absent. In general, the rate of ion exchange accompanied by chemical reaction is faster than mass transfer or diffusion step (Tan, 2000). Chemical reaction of ions, diffusion through the bulk solution and diffusion of the ions through the boundary layer between the film and adsorbent are generally fast and may not determine the rate of the reaction.

External film diffusion is generally the rate limiting step at the initial period of time in process and it may be affected from the agitation speed and particle size of the adsorbent. Therefore different agitation speeds should be studied to understand external film diffusion is the controlling step or not. Particle size of adsorbent related with the external surface area of the adsorbent which affect the initial uptake rate. When particle size decreases, initial uptake rate is accelerated and shorter time is enough to reach equilibrium.

Ion exchange rate depends on the sorbate concentration and temperature if the ion exchange is reaction controlled. When sorbate concentration increased, ion exchange rate increases since active sites of sorbate are binded with sorbate molecules easily.

Figure 4.4 shows that the kinetics of ion exchange (sorption) between the particle (adsorbent) and the solution involve five steps (Braun et al., 2002; Tan, 2000):

- The chemical reaction involving the exchange of ions
- Diffusion of the ions through the bulk solution in order to reach the adsorbent
- Diffusion of the ion across the external film surrounding the adsorbent

- Diffusion of the ion through the boundary between the film and the adsorbent
- Diffusion of the ion through the adsorbent in the pores and along the pore walls

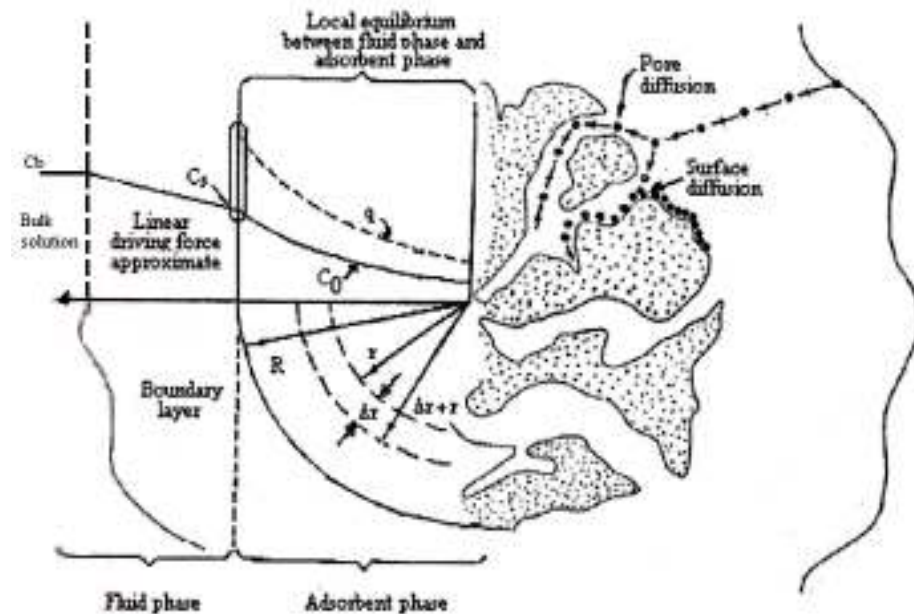


Figure 4.4. General scheme of mass transfer and diffusion mechanism.

In the absence of rate limitation by the chemical reaction, rate controlling process may be diffusion. Besides the diffusion process within the crystallite micropores which is intraparticle diffusion, the rate controlling process can be film or boundary layer diffusion which is observed between the external solution and the crystallite surface (Bekkum et al., 2001; Ibrahim and Hassan, 2008).

4.2.2. Kinetic Models

Kinetics of ion exchange mechanism can be investigated with some mathematical models to determine the rate determining step in process. The mechanism can be described with ion exchange reaction and diffusion models. Not only the reaction models but also diffusion models should be used together to interpret the data. Since ion exchange rate may be affected with the several resistances like surface resistance, intraparticle diffusion and chemical reaction.

4.2.2.1. Reaction Models

Pseudo first order reaction model

The liquid-solid adsorption system may be described by pseudo first order reaction equation. The differential equation is the following (Ho, 2004);

$$\frac{dq}{dt} = k(q_e - q) \quad (4.2)$$

where q_e and q (meq g^{-1}) are the amount adsorption at equilibrium and at time t , respectively. k (min^{-1}) is the rate constant of pseudo first order adsorption. An integrated pseudo first order reaction model can be obtained from Equation 4.2 for the boundary conditions $t=0$ to $t=t$ and $q=0$ to $q=q$, and is given by:

$$\ln\left(\frac{q_e}{q_e - q}\right) = kt \quad (4.3)$$

Equation 4.3 can be written as most popular form used;

$$\log(q_e - q) = \log(q_e) - \frac{k}{2.303}t \quad (4.4)$$

Pseudo first order rate equation can not describe effectively the adsorption behavior for all the temperatures. This is probably due to some complex nature of adsorption (Sarkar et al., 2003).

Pseudo second order reaction model

In many cases, the equilibrium capacity is unknown and long time can be required to reach equilibrium. The pseudo second order reaction model was developed by Ho in 1995 for solid-liquid systems and provides to determine the equilibrium adsorbed amount, rate constant and the initial ion exchange rate (Ho, 2004).

The differential change of pseudo second order reaction model can be written as follows:

$$\frac{dq}{dt} = k(q_e - q)^2 \quad (4.5)$$

where k is the rate constant of pseudo second order reaction ($\text{g meq}^{-1} \text{min}^{-1}$), q and q_e (meq g^{-1}) are the solid-phase concentration at any time t and at equilibrium, respectively. An integrated pseudo second order reaction model can be obtained from Equation 4.5 for the boundary conditions $t=0$ to $t=t$ and $q=0$ to $q=q$, and is given by:

$$q = \frac{t}{\frac{1}{kq_e^2} + \frac{t}{q_e}} \quad (4.6)$$

and

$$h = kq_e^2 \quad (4.7)$$

where h ($\text{meq g}^{-1} \text{min}^{-1}$) is the initial rate when time goes to 0.

4.2.2.2. Diffusion Models

Intraparticle Diffusion Model

The intraparticle diffusion model is used to interpret diffusion kinetics for the systems. When the exchanged ions by the adsorbent are small relative to the total quantity of ions into the isothermal system, the intraparticle pore diffusion in the spherical particle with appropriate boundary conditions can be solved analytically (Crank, 2003; Ruthven, 1984). For a spherical particle, adsorbent phase mass balance can be written as;

$$\frac{\partial q}{\partial t} = \frac{1}{r^2} \frac{\partial}{\partial r} \left(r^2 D \frac{\partial q}{\partial r} \right) \quad (4.8)$$

Because of small change in adsorbed phase concentration, D (intraparticle diffusivity) is constant and Equation 4.8 is simplified to;

$$\frac{\partial q}{\partial t} = D \left(\frac{\partial^2 q}{\partial r^2} + \frac{2}{r} \frac{\partial q}{\partial r} \right) \quad (4.9)$$

The initial and boundary conditions;

$$q(r,0) = q_0 \quad q(r,t) = q_e \quad \left(\frac{\partial q}{\partial r} \right)_{r=0} = 0 \quad (4.10)$$

The exact solution of Equation 4.9 is given by Crank (2003) as follows;

$$\frac{q - q_0}{q_e - q_0} = \frac{\bar{q}}{q_e} = 1 - \frac{6}{\pi^2} \sum_{n=1}^{\infty} \frac{1}{n^2} \exp\left(-\frac{n^2 \pi^2 Dt}{r^2}\right) \quad (4.11)$$

where \bar{q} is the average value of q at any time, q_0 is zero when time equals to zero and q_e is the average concentration in the solid at equilibrium. Since higher terms of the summation become vanishingly small, the Equation 4.11 is written for greater than 70 % of ion exchange as;

$$\frac{q}{q_e} = 1 - \frac{6}{\pi^2} \exp\left(-\frac{\pi^2 D t}{r^2}\right) \quad (4.12)$$

Crank also proposed Equation 4.13 when t is small:

$$\frac{q}{q_e} = 6 \left(\frac{Dt}{r^2} \right)^{0.5} \left[\frac{1}{\sqrt{\pi}} + 2 \sum_{n=1}^{\infty} \frac{1}{n^2} \operatorname{ierfc} \left(\frac{nr}{\sqrt{Dt}} \right) \right] - \frac{3Dt}{r^2} \quad (4.13)$$

Equation 4.13 reduces to :

$$\frac{q}{q_e} = \frac{6}{\sqrt{\pi}} \left(\frac{Dt}{r^2} \right)^{1/2} \quad (4.14)$$

The Equation 4.14 can be represented by Equation 4.15:

$$q = k_i t^{1/2} \quad (4.15)$$

where q (meq g^{-1}) is the amount of ion exchanged at time t , k_i ($\text{meq g}^{-1}\text{h}^{-1/2}$) is the intraparticle diffusion rate constant. The rate constant is determined from the slope of the linear portion of the plot of q vs $t^{1/2}$ which characterizes the rate of adsorption in the region where pore diffusion is rate limiting. If there is an intercept of the plot, it shows the extent of boundary layer effect (external film resistance). At this point, adsorption consists of both surface adsorption and the intraparticle diffusion within the pores of the adsorbent (Sarkar et al., 2003).

The larger the intercept, the greater is the contribution of the external film resistance in the rate limiting step. McKay and Poots extended this model also over longer time periods (Choy et al., 2004)

According to the approximation of Vermeulen (Helfferich, 1962), the Equation 4.16 can be used for the $q/q_e > 0.1$.

$$\frac{q}{q_e} = \left[1 - \exp\left(-\frac{\pi^2 Dt}{r^2}\right) \right]^{0.5} \quad (4.16)$$

Barrer et al. also interpreted diffusion kinetics and proposed as follows (Dyer, 1999; Ash et al., 1977);

$$I_o = \int_0^{\infty} \left(1 - \frac{q}{q_e} \right) dt = \frac{r^2}{15D} \quad (4.17)$$

where I_0 is the area between the asymptote and the curve of q/q_e against time (t), r is the radius of the adsorbent. Equation 4.17, provides to evaluate diffusion coefficient, D , when diffusion coefficient is independent of concentration, position with a large t at constant pressure. This method is a useful and simple method.

External Film Diffusion Model

Diffusion within the adsorbent is very rapid and the rate of solute accumulation in the solid phase is equal to solute transfer according to the mass balance law. The ion exchange rate is given by (Qiu et al., 2009);

$$V_p \left(\frac{\partial \bar{q}}{\partial t} \right) = k_f A_s (C - C^*) \quad (4.18)$$

where \bar{q} is the average solute concentration in the solid, V_p is the volume of the particle, A_s is the surface area of the adsorbent, $(C - C^*)$ is the concentration driving force in the bulk of the liquid and at the adsorbent/liquid interface, respectively.

When the concentration change is sufficiently small, the equilibrium relationship will be linear ($q^* = KC$) and bulk fluid concentration, C , will be constant. Therefore, Equation 4.18 can be rearranged to;

$$\frac{d \bar{q}}{dt} = \frac{3k_f}{Kr} (q^* - \bar{q}) \quad (4.19)$$

where K is the dimensionless Henry's Law constant, r is the radius of adsorbent, q^* is the final equilibrium adsorbed phase concentration and k_f is the external film mass transfer coefficient. Equation 4.19 can be solved by appropriate conditions given in Equation 4.20.

$$t < 0 \quad C = q = 0 \quad \text{and} \quad t > 0 \quad C = C_e = q_e / K \quad (4.20)$$

The integrated form of the Equation 4.19 is written in Equation 4.21 (Karger and Ruthven, 1991).

$$\frac{\bar{q}}{q_e} = 1 - \exp\left[-\frac{3k_f t}{Kr}\right] \quad (4.21)$$

Calculation of External Film Mass Transfer Coefficient

The external film mass transfer coefficients can be obtained by correlation method and dimensional analysis method. In the correlation method, the experimental data of the ion exchange is substituted into the external film diffusion model to calculate the external film mass transfer coefficient as mentioned above. In the dimensional analysis method, the characterization of the zeolites, counter ion and the velocity of zeolites are used for calculating the film diffusion coefficient. The results from the correlation method and dimensional analysis method will be compared in the results and discussion part to interpret the values of the external film mass transfer coefficients.

The external film mass transfer coefficient can be calculated from the Sherwood number (Sh) which is defined as;

$$Sh = \frac{k_f D_p}{D} = 2 \quad (4.22)$$

The Equation 4.22 is used for stagnant fluid that the limiting value of Sherwood number for low Reynolds number flow is 2. At higher Reynolds numbers, Sherwood number is the function of Schmidt and Reynolds numbers ($Sh=f(Sc,Re)$) and the Ranz and Marshall equation can be used to calculate the Sherwood number (Ranz and Marshall, 1952 ; Seader and Henley, 2006).

$$Sh = \frac{k_f D_p}{D} = 2 + 0.6 Re^{1/2} Sc^{1/3} \quad Sh \leq 160 \quad (4.23)$$

$$\text{Re} = \frac{D_p V \rho}{\mu} \qquad \text{Sc} = \frac{\mu}{\rho D} \qquad (4.24)$$

where, D ($\text{m}^2 \text{s}^{-2}$) is diffusivity, k_f is the external film mass transfer coefficient ($\text{m} \text{s}^{-1}$), D_p is the spherical diameter (m), μ ($\text{kg} \text{m}^{-1} \text{s}^{-1}$) and ρ ($\text{kg} \text{m}^{-3}$) are the viscosity and density of the fluid.

Calculation of mass transfer Biot number

Mass transfer Biot number, Bi_m , is a ratio of the external film mass transfer rate to the internal mass transfer rate given in Equation 4.25 which indicates the diffusion stage in ion exchange.

$$Bi_m = r_c k_f / D \qquad (4.25)$$

where r_c is the critical radius and taken as $r/3$ for spherical particle, k_f is the external film mass transfer coefficient and D is the diffusion coefficient. According to the Equation 4.25, if the Bi_m is much smaller than 1 ($Bi_m \ll 1$), the resistance to diffusion within the solid (intraparticle diffusion) is much less than the resistance to diffusion across the fluid boundary layer or external film. If the value is much larger than 1 ($Bi_m \gg 1$) it shows that the intraparticle mass transfer rate is reduced and thus controls the overall exchange rate (Incropera et al., 2007; Yang et al., 2003).

In literature, there are some information about the value of Biot number in order to identify the which resistance is dominant. Depaoli and Perona stated that as the Biot number increases over 30, the intraparticle mass transfer rate decreased and controls the ion exchange rate (Depaoli and Perona, 1996). However, Traegner and Suidan stated that intraparticle diffusion is the dominant mass transfer mechanism when the Biot number is higher than 100 (Traegner and Suidan, 1989; Mier et al., 2001). If the Biot number is lower than 0.5 it shows that external film resistane is dominant (Crittenden et al., 1980; Friedman, 1984). Although, Incropera et al. and Sander et al. stated that when the Biot number is lower than 0.1, the external film resistane is dominant (Incropera et al., 2007; Sander et al., 2003)

Surface Diffusion Model

If ion exchange occurs at the adsorbent surface and there is no gradient of concentration through the adsorbent, the rate expression is given by;

$$\frac{d \bar{q}}{d t} = k_s a (q^* - \bar{q}) \quad (4.26)$$

where k_s (m s^{-1}) is the surface resistance for a spherical adsorbent which is the ratio of the effective diffusivity and thickness of the adsorbent surface film (D/δ), a is the specific external area (the ratio of the area and volume of the sphere = $3/r$), r is the radius of the zeolite particle, q^* (meq g^{-1}) is the final equilibrium adsorbed phase concentration, \bar{q} is the average value of q in adsorbent at any time.

An integrated surface diffusion model can be obtained from Equation 4.26 for the boundary conditions $t=0$ to $t=t$ and $q=0$ to $q=q_e$, and is given by (Karger and Ruthven, 1991):

$$\frac{\bar{q}}{q_e} = 1 - \exp\left(-\frac{3k_s t}{r}\right) \quad (4.27)$$

4.3. Thermodynamics of Ion Exchange

The thermodynamic activation parameters such as enthalpy of activation, entropy of activation and free energy of activation can be applied by using intraparticle diffusion rate constant, k_i , for ion exchange given in Equation 4.28 with Eyring equation (Al-Ghouti et al., 2005).

$$\ln\left(\frac{k_i}{T}\right) = \left[\ln\left(\frac{k_B}{h_p}\right) + \frac{\Delta S^*}{R} \right] - \frac{\Delta H^*}{R} \left(\frac{1}{T}\right) \quad (4.28)$$

where k_B is the Boltzmann constant ($1.3807 \times 10^{-23} \text{ J K}^{-1}$), h_p is the Planck constant ($6.6261 \times 10^{-34} \text{ Js}$), k_i is the intraparticle diffusion rate constant of ion exchange.

An activation energy has been also evaluated from the intraparticle diffusion rate constants given in Equation 4.29 (Ho, 1998; Al-Ghouti et al., 2005; Sarkar et al., 2003).

$$k_i = k' \exp\left(-\frac{E_a}{RT}\right) \quad ; \quad \ln(k_i) = \ln(k') - \frac{E_a}{R} \left(\frac{1}{T}\right) \quad (4.29)$$

where k' is the pre-exponential constant, E_a is activation energy (kJ mol^{-1}) (i.e., activation energy for ion exchange to an external surface of the adsorbent), R is the gas constant ($8.314 \text{ J mol}^{-1}\text{K}^{-1}$), T is the solution temperature (K). A plot of $\ln k$ versus $1/T$ gives a straight line with slope $-E_a/R$. The activation energy, E_a , can be viewed as an energy barrier which the reaction must overcome.

The Arrhenius equation is empirical and not exact contrary to the analogous van't Hoff equation for the temperature dependence of equilibrium constants since the pre-exponential factor is not entirely independent of temperature. Therefore, slight deviations from straight-line behavior must be expected (Bamford et al., 1993).

CHAPTER 5

GAS ADSORPTION

Adsorption occurs whenever a solid surface (adsorbent) exposed to a gas or liquids. The substances in the adsorbed state are called as adsorbate shown in Figure 5.1.

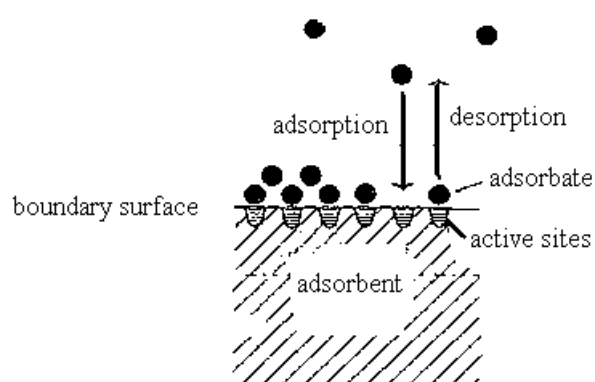


Figure 5.1. Representative adsorption and desorption on adsorbent.

Adsorbent material such as activated carbon, zeolites, silica gel, activated alumina and etc. are classified according to the pores by IUPAC. This is the important criteria for choosing adsorbent in any adsorption-based technology and given as follows;

- microporous (diameter $< 20 \text{ \AA}$)
- mesoporous ($20 \text{ \AA} < \text{diameter} < 500 \text{ \AA}$)
- macroporous (diameter $> 500 \text{ \AA}$)

Physical adsorption is always an exothermic process and decrease with increase of temperature. It is brought about by the interactions between the adsorbent and molecules in the fluid phase which is physisorption. Physisorption involves only relatively weak intermolecular forces. However, chemisorption responsible for the formation of chemical bond between the adsorbate molecule and the surface of adsorbent.

Besides to adsorption technique to separate the mixtures, cryogenic distillation, membrane processes, chemical absorption and physical absorption can be also used.

Absorption should not be mixed up with adsorption. Adsorption occurs at any pressure and temperature and molecules of gases or liquids stick to the surface of a solid material. However, absorption is bulk or volume phenomenon and pressure or temperature is not necessary for process (Keller and Staudt, 2005).

There are a lot of applications of the adsorption technologies. Some of them are;

- separation of gases (air separation, air conditioning, air purification, sewage gas purification, flue-gas purification, hydrogen separation from primary gas mixture and etc.)
- purification of liquids
- pollution control
- respiratory protection
- biological application
- heterogeneous reaction applications

5.1. Gas Adsorption Measurement Technique

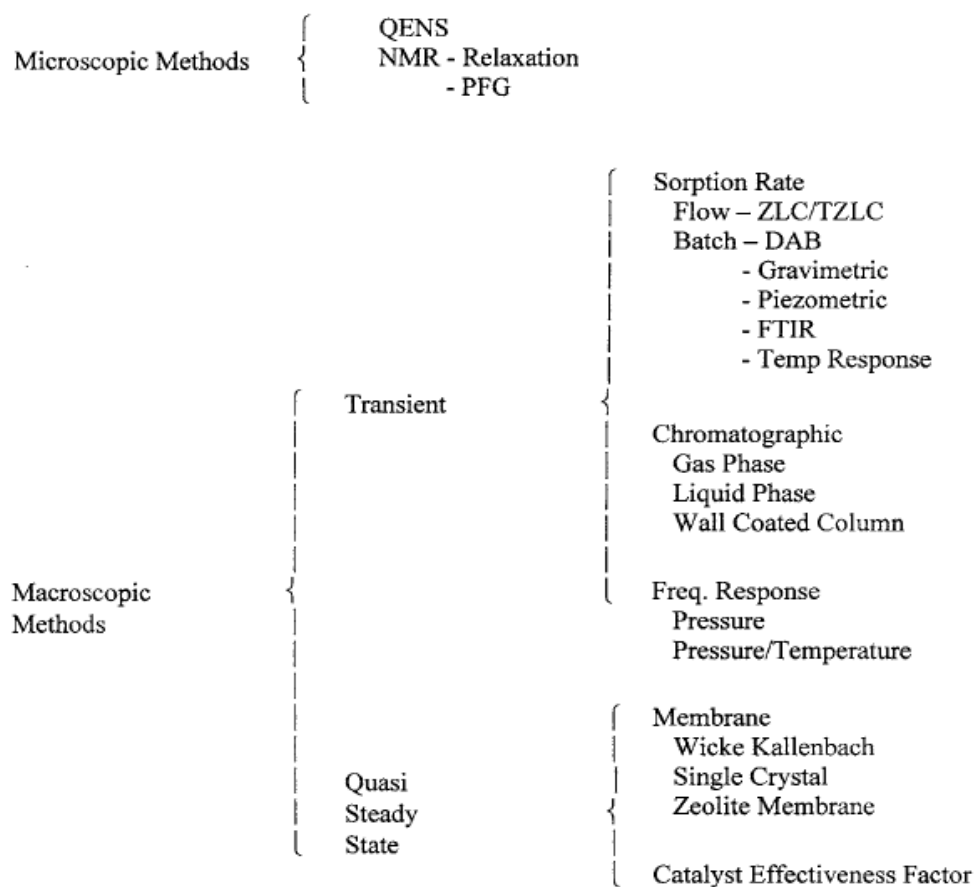
A wide range of different experimental methods have been applied to the measurement of micropore diffusion given in Table 5.1 (Bekkum et al., 2001 ; Karge and Weitkamp, 2008).

Nuclear magnetic resonance (NMR) and neutron scattering (QENS) are the microscopic method and equilibrium measurements are made on a scale smaller than dimensions of an individual crystal by following the mean square displacement of the molecules in a known time interval. NMR technique is a non-invasive technique allows the observation of molecular transport in porous media without any disturbance of their intrinsic molecular dynamics. Pulsed-field gradient NMR (PFG NMR) is able to provide direct information about the rate of molecular migration in the intracrystalline space and follow molecular diffusion paths from 100 nm up to 100 μm (Rouquerol et al., 1999). Neutron spin-echo technique is also microscopic method and depends on measuring the rate of a catalytic reaction under diffusion-controlled conditions.

Single crystal membrane permeation, FTIR and the recently developed interference microscopy technique can be classified as mesoscopic methods and to be applied at the scale of the individual crystal.

If the small sample of adsorbent is subjected to change in ambient concentration (or partial pressure) of sorbate, it is the most obvious way to measure intracrystalline diffusion with direct measurement of the adsorption or desorption rate. Macroscopic methods measure the transport diffusion and depend on measuring the flux under a well defined gradient of concentration. If the diameter of the diffusing molecule is slightly smaller than the pore diameter, diffusion within an ideal micropore is fast and difficult to measure by macroscopic methods. Slow transport diffusion is easily measured macroscopically when the molecular diameter of the sorbate approaches the minimum diameter of the pore, the diffusional activation energy increases and the diffusivity drops by orders of magnitude but it is inaccessible to microscopic techniques. Especially in batch measurements, transient uptake rate measurements are subject to intrusion of heat transfer limitations at low pressures. Membrane permeation, frequency response and ZLC measurements should not be subject to heat transfer limitations. For frequency response and ZLC measurement, the danger of intrusion of extracrystalline resistances to mass transfer can be eliminated by reducing the sample size and dispersed the crystals effectively. The volumetric or manometric method are used mostly as standard method to measure gas adsorption equilibria in today. Principle of this method is to measure the gas pressure in a calibrated constant volume at a known temperature. Gravimetric method is also more accurate and reliable measurements performed by weighing the sorbent mass exerted to the gas atmosphere using a very sensitive microbalance.

Table 5.1. Classification of methods to measure the intracrystalline diffusion in zeolites.
(Source: Bekkum et al., 2001)



The zero length column (ZLC) as a macroscopic method is a fairly new measurement method allowing in principle to get information of adsorption equilibria as well as of adsorption kinetics. ZLC method was studied in this thesis and detail information was given in the following part. Studies with Zero Length Column (ZLC) technique were given in Table 5.2.

Table 5.2. Studies with Zero Length Column (ZLC) technique in literature.

Studies	Adsorbent	Adsorbate	Method	Reference
Diffusion of linear paraffins in silicalite studied by the ZLC method in the presence of CO ₂	Silicalite	<i>n</i> -butane <i>n</i> -hexane <i>n</i> -octane <i>n</i> -decane and CO ₂	ZLC with GC chromatograph	Guimarães et al., 2010
Evaluation of the main diffusion path in novel micro-mesoporous zeolitic materials with the zero length column method	UL-ZSM5 ZSM-5, ZSM-12 Al-Meso-100	<i>n</i> -heptane Toluene	Zero length column method	Malekian et al., 2007
Diffusion of linear paraffins in NaCaA studied by the ZLC method	NaCaA	Linear Alkanes	ZLC with GC chromatograph	Brandani and Gunadi, 2006
Measurement of adsorption equilibrium by the Zero Length Column (ZLC) Technique Part 1: Single Component system	CaA, NaLSX	CO ₂ , N ₂ CO, CH ₄ (pure / mixture)	ZLC with quadrupole mass spectrometer	Brandani et al., 2003
Adsorption of propane and propylene onto carbon molecular sieve	CMS 4A	Propane N35 propylene N24	ZLC with GC chromatograph	Grande et al., 2003
Improved estimation of zeolite diffusion coefficients from zero-length column experiments	Silicalite	Benzene Ethylbenzene	ZLC with GC chromatograph	Loos et al., 2000
Analysis of ZLC desorption curves for liquid systems	NaX	Benzene Hexane	Zero length column method	Ruthven and Brandani, 1995
Diffusion of light alkanes in silicalite studied by the zero length column method	Silicalite	<i>n</i> -butane Isobutane Propane	ZLC with GC chromatograph	Hufton and Ruthven, 1993

5.2. The ZLC Method for Single Component System: Background and Theory

The zero length column (ZLC) method which is a chromatographic method was developed in the late 1980s by Eic and Ruthven (Loos et al., 2000 ; Eic et al., 2002). It has been applied to many different systems as a simple and relatively inexpensive way to determine the controlling mechanism and estimate the diffusivities of hydrocarbons and other simple molecules in zeolites and other microporous adsorbents (Hufton and Ruthven, 1993; Grande et al., 2003). The ZLC method has been widely carried out to measure both micropore and macropore diffusion coefficients by using desorption curves of sorbate previously equilibrated with a small sample of adsorbent into an inert carrier stream (Brandani et al., 1996).

As seen from the Figure 5.2, the ZLC column consists of zeolite granules are sandwiched between the quartz wool or sintered discs placed both side of the column. Gas passes through the crystals and flows to a detector to calculate the concentration of adsorbed gas. At first, an inert carrier gas contains a very small amount of adsorbate and equilibrated with adsorbent. Then, the rate of desorption is determined from the time dependent adsorbate concentration in the carrier gas. From the desorption curve, micropore diffusion coefficient is calculated (Hufton and Ruthven, 1993; Silva and Rodrigues, 1999).

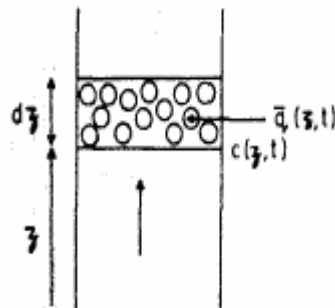


Figure 5.2. Representative Zero Length Column including zeolite granules.

Overall system can be solved analytically, when Henry's law was accepted under isothermal conditions. Rates of adsorption and desorption are generally controlled by transport within the pore network in porous adsorbents. Bulk flow through the pores

is considered intraparticle transport as a diffusive process defined with Fick's Law (Ruthven, 1984).

The advantages of this method are to minimize the external mass and heat transfer resistances by flowing the carrier gas since the crystals are dispersed approximately as a monolayer and sandwiched between two sintered discs. Therefore, adsorption cell can be considered as a perfectly mixed isothermal, continuous flow cell. Also, using the crystal form of zeolite instead of composite or pellet form of zeolite eliminates the possible intrusion of macropore resistance.

5.2.1. Flow Through Zero Length Column

The ZLC method is an experimental technique to measure the intraparticle diffusivities and the Henry constants in a gas-solid systems. This method consists of two steps. First one, a small amount of a adsorptive (C_0) is diluted in an inert gas (helium) at constant partial pressure and temperature, thus, the adsorbent is saturated. At the second step, ZLC is purged with inert gas at the same temperature of the previous step at a fixed flow rate (F). The effluent concentration (C) of desorption curves are recorded and compared with an analytical model.

The zero length column is short enough including only a few layers of adsorbent to be treated as a well-mixed cell. The reciprocal axial *Peclet number* (D_L/vL) is used to control the axial mixing in a column (Brandani et al., 2003). When $L \rightarrow 0$, $D_L/vL \rightarrow \infty$, so the system behaves as a well mixed cell. Flow through a ZLC with the axial dispersion coefficient is

$$-D_L \frac{\partial^2 c}{\partial z^2} + V_f \frac{dc}{dt} + V_s \frac{d\bar{q}}{dt} + F c = 0 \quad (5.1)$$

where D_L ($\text{cm}^2 \text{s}^{-1}$) is axial dispersion coefficient, L (cm) is the length of the ZLC, v (cm.s^{-1}) is the interstitial gas velocity, V_f (cm^3) is the volume of fluid in column, V_s (cm^3) is the volume of adsorbent in column, F ($\text{cm}^3 \text{s}^{-1}$) is the volumetric gas flow rate of the inert gas, C (mol cm^{-3}) is the gas phase concentration and \bar{q} (mol cm^{-3}) is the average adsorbed phase concentration through the crystal. For particle diameter less than 0.3 cm, the limiting Peclet number is given approximately as follows:

$$r_p < 0.15 \text{ cm} \quad \text{Pe}_\infty \approx 3.35 r_p$$

Pore diffusional resistance are reduced with reduction of particle size which increased axial dispersion with the lower particle diameter below about 0.3 cm (Ruthven, 1984). Equation 5.1. is reduced to Equation 5.2.

$$V_f \frac{dc}{dt} + V_s \frac{d\bar{q}}{dt} + F c = 0 \quad (5.2)$$

In Equation 5.2, the first term (gas phase accumulation) is very small when compared with the second term (adsorbed phase) and it was neglected. Thus, Equation 5.2 is reduced and given below.

$$V_s \frac{d\bar{q}}{dt} + F c = 0 \quad (5.3)$$

Heat effects can be negligible because of using small adsorbent sample. Therefore, isothermal conditions can be accepted for the modelling of the desorption cell. However, heat effects on the zero length column experiments was investigated. (Silva et al., 2001). If the heat transfer resistance is accepted only at the external surface of the sample, this implies the assumption of constant temperature throughout the sample, the following equation can be written as:

$$-\Delta H \frac{d(\bar{q})}{dt} = C_p \frac{dT}{dt} + ha(T - T_o) \quad (5.4)$$

where ΔH (J mol^{-1}) is heat of adsorption, C_p ($\text{J cm}^{-3}\text{K}^{-1}$) is specific heat capacity of the adsorbent, h ($\text{J cm}^{-2}\text{s}^{-1}\text{K}^{-1}$) is the heat transfer coefficient, a (cm^{-1}) is external surface area per unit volume of the adsorbent, T (K) is the temperature. At low adsorbate concentration, the equilibrium relationship is linear and temperature changes very small. Then the following equation is written as:

$$q = q_o + \left. \frac{\partial q}{\partial c} \right|_{c_o, T_o} (c_{out} - c_o) + \left. \frac{\partial q}{\partial T} \right|_{c_o, T_o} (T - T_o) \quad (5.5)$$

where C (mol cm^{-3}) is gas phase concentration and C_o (mol cm^{-3}) is the initial gas concentration. In this Equation 5.5, $K = (\partial q / \partial c)$ at c_o and T_o is the dimensionless Henry's Law constant. The initial conditions under equilibrium relation are;

$$t = 0, \quad q = q_o = K(T_o)c_o, \quad T = T_o \quad (5.6)$$

B and α are the dimensionless numbers and are defined as follows:

$$\beta = \frac{\Delta H}{C_p} \left. \frac{\partial q}{\partial T} \right|_{c_o, T_o} \quad (5.7)$$

$$\alpha = \frac{ha}{C_p} \frac{r^2}{D_c} \quad (5.8)$$

$$ha = 3\lambda / r_c^2 \quad (5.9)$$

where λ is the thermal conductivity of gas. The isothermal case is obtained when β and α goes to zero. Thus, $3L\beta/\alpha$ decreases and the system approaches the isothermal operation. A criterion for negligible heat effects is derived from the analytical solution based on ZLC parameters which is $3L\beta/\alpha < 0.1$. $3L\beta/\alpha$ can be written as follows:

$$\frac{3L\beta}{\alpha} = c_o \frac{F (\Delta H)^2}{V_s RT_o^2 ha} \quad (5.10)$$

where F ($\text{cm}^3 \text{s}^{-1}$) is the volumetric gas flow rate of the purge gas and L is the dimensionless ZLC parameter mentioned in Equation 5.18 and R ($\text{cal K}^{-1} \text{mol}^{-1}$) is the ideal gas constant. Heat effects are minimized in various ways, such as decreasing the gas concentration, C_o , decreasing the particle size in order to increasing the external surface area per unit volume of adsorbent.

5.2.2. Mathematical Models

In a zero length column, the assumptions used to obtain a mathematical expression for response curves are as follows:

- Zeolite crystals have spherical geometry.
- Gas behavior is ideal.
- The process is isothermal because of the small quantity of adsorbent used.
- Perfect mixing throughout the ZLC cell, if the holdup in the fluid phase is neglected.
- Axial dispersion and mass transfer resistance can be neglected. Because instantaneous equilibration is assumed at the external surface of the adsorbent particles in the very small column (ZLC).
- The equilibrium relationship between adsorbed phase and fluid phase will be linear at sufficiently low concentrations. This linear relationship is commonly referred to as Henry's law (K).
- The self supported adsorbent has a porous structure containing micropores and the mass transfer control is limited by micropore diffusion, D_c , due to crystal structure.
- Micropore diffusion coefficient (or crystalline diffusivity), D_c , is constant and does not change with concentration.

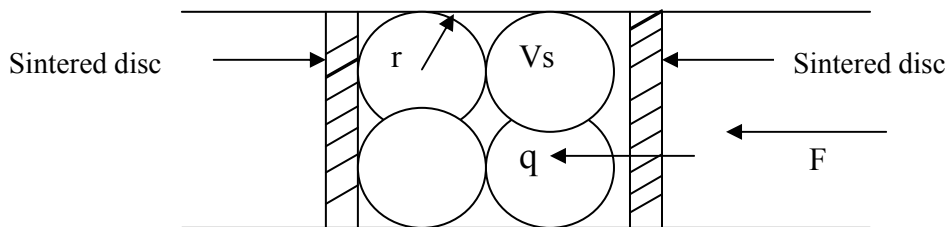


Figure 5.3. Zero Length Column.

As shown in Figure 5.3. the mass balances around the adsorbent

$$\frac{\partial q}{\partial t} = D_c \left(\frac{\partial^2 q}{\partial r^2} + \frac{2}{r} \frac{\partial q}{\partial r} \right) \quad (5.11)$$

and mass balance into fluid phase of the ZLC column

$$V_s \frac{d\bar{q}}{dt} + F c = 0 \quad (5.3)$$

can be solved analytically by using the boundary and initial conditions

$$q(r, 0) = \bar{q}(0) = q_o = K C_o \quad C(0) = C_o \quad \left(\frac{\partial q}{\partial r} \right)_{r=0} = 0 \quad (5.12)$$

$$\left(\bar{q} \right) = \frac{3}{r^3} \int_0^{r_c} q r^2 dr \quad (5.13)$$

Analytic solution equation for ZLC system (Crank 2003);

$$\frac{q_o - \bar{q}}{q_o} = 1 - 6L^2 \sum_{n=1}^{\infty} \frac{\exp(-\beta_n^2 D_c t / r^2)}{\beta_n^2 [\beta_n^2 + L(L-1)]} \quad (5.14)$$

where;

$$\beta_n \cot \beta_n + L - 1 = 0 \quad (5.15)$$

and L is the time constant ratio shows the relation between the flow rate and the controlling steps.

$$L = \frac{1 \text{ purge flow rate } r^2}{3 \text{ crystals volume } K D_c} = \frac{\left(\frac{r^2}{D_c} \right)}{\left(\frac{3 K V_s}{F} \right)} \quad (5.16)$$

When the Equation 5.14 is differentiated and substituted into Equation 5.3, the gas phase concentration of adsorbate is expressed as;

$$\frac{C}{C_o} = 2L \sum_{n=1}^{\infty} \frac{\exp(-\beta_n^2 D_c t / r^2)}{\beta_n^2 + L(L-1)} \quad (5.17)$$

Special Case I: Diffusion controlled system for $C/C_o > 0.7$

β_n are the roots of the equation and only the first root of Equation 5.15 contributes to the summation part of the Equation 5.17, it reduces to;

$$\frac{C}{C_o} = \frac{2L}{\beta_1^2 + L(L-1)} \exp\left(-\frac{\beta_1^2 D_c t}{r^2}\right) \quad (5.18)$$

The micropore diffusion coefficient, D_c , and the dimensionless Henry constant, K , can be determined from the slope and intercept of a plot of $\ln(C/C_o)$ versus t .

Special Case II: Diffusion controlled system for $C/C_o < 0.3$

Gas phase adsorbate concentration can be also expressed as more useful form of the solution for the $C/C_o < 0.3$ as the following equation;

$$\frac{C}{C_o} = \left(\frac{r^2}{L^2 \pi D_c t}\right)^{1/2} - \frac{1}{L} \quad (5.19)$$

D_c and K are estimated from the slope and the intercept of a plot of C/C_o versus $t^{-1/2}$ by the time analysis. Special case I and II are performed at high flow rates such that the effluent concentration is determined by the rate. This mean that sorbate diffuses out of the adsorbent particles.

Special Case III: Equilibrium controlled system

When the ZLC experiment is performed at a sufficiently low flow rate, then L is small and the desorption rate is controlled entirely by convection. In other words, the adsorbate phase is always in equilibrium with the gas phase as the following equation; (Brandani and Ruthven 2005).

$$\bar{q} = KC(t) \quad (5.20)$$

When L is small, β is small and $\beta_n \cot \beta_n$ can be replaced by the first term of the Equation 5.17 and equal to approximately $L \approx \beta^2/3$. Then, the concentration response curve as the simple exponential form can be written as;

$$\frac{c}{c_0} = \exp\left(\frac{-Ft}{KV_s + V_f}\right) \quad (5.21)$$

The response curve is independent of the flow rate under equilibrium control. A plot of $\ln(c/c_0)$ vs. time should give a straight line through the origin with slope $-F/(KV_s + V_f)$. When K has a large value, KV_s value should be higher than V_f . The slope yields directly the value of the dimensionless Henry's Law constant (K).

5.2.3. Analysis Dimensionless Theoretical ZLC Curves

Theoretical ZLC curves are plotted in dimensionless form as seen in Figure 5.4. The diffusion controlled system for fractional uptakes greater than 70 % shows large values of L ($L > 5$), that is the concentration initially decreases very rapidly, followed by an exponential decrease at longer time. However, the kinetics are controlled by equilibrium effects for small values of L ($L < 1$) that is the initial rapid drop in concentration is absent and only an exponential decay is observed (Figure 5.4). It can be said that desorption process is diffusion controlled if $L > 5$ whereas if $L < 1$ it is equilibrium controlled process.

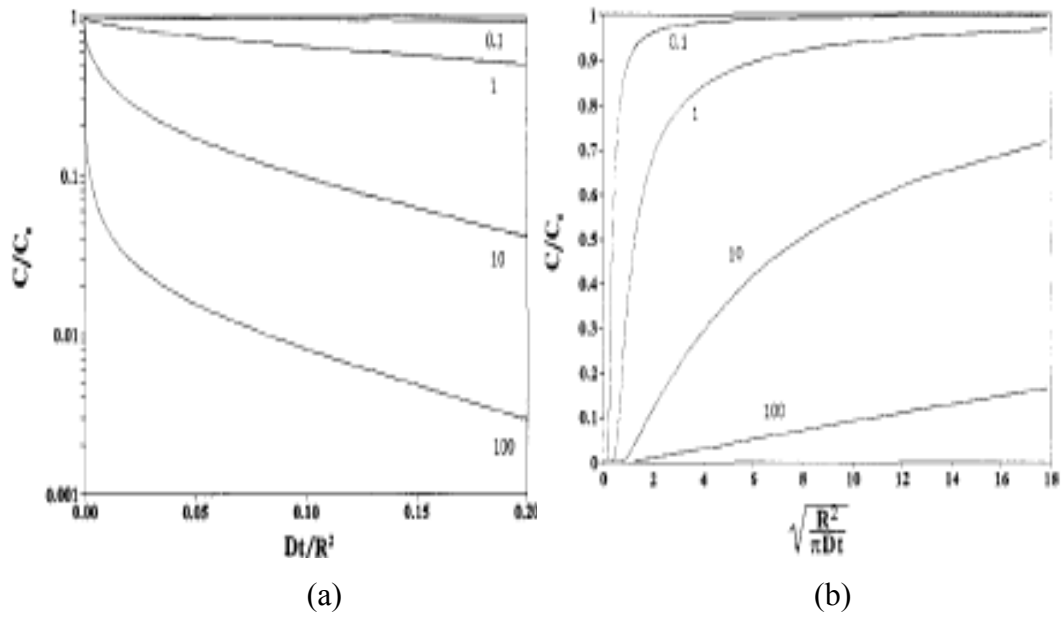


Figure 5.4. Dimensionless theoretical ZLC curves (a) Diffusion controlled system for $C/C_0 > 0.7$ (b) Diffusion controlled system for $C/C_0 < 0.3$.

Analysis by the diffusion controlled system for $C/C_0 < 0.3$, the method shows that for large values of L the plot of C/C_0 versus $t^{-1/2}$ is linear, whereas for equilibrium control (L small) this plot is of sigmoid form given in Figure 5.4 (b) (Hufton and Ruthven, 1993).

5.3. Selectivity

Suitable adsorbent is the first step to provide efficiency of an adsorption separation process. Adsorbent with sufficiently high selectivity and capacity is required for an economic separation process. The selectivity may depend on a difference either adsorption equilibrium or kinetics. However, most of the adsorption processes use depend on equilibrium selectivity. To consider the such processes, separation factor can be defined as (Ruthven, 1984);

$$\alpha_{AB} = \frac{X_A / X_B}{Y_A / Y_B} \quad (5.22)$$

where X and Y are the mole fractions of component A or B in adsorbed and fluid phase at equilibrium, respectively.

Separation factor generally varies with temperature and composition. Therefore, suitable conditions must be selected to maximize the separation factor. However, separation factor is independent of composition and equal to the ratio of the Henry's law constants to relevant components for an ideal Langmuir system given in Equation 5.23. This approach works well for some systems such as CH₄-CO₂ in 5A and NaX zeolite and very quick and reliable method of estimating separation factors (Karge and Weitkamp, 2008; Ruthven, 1984).

$$\alpha_{AB} = \frac{q_A / p_A}{q_B / p_B} = \frac{K_A}{K_B} \quad (5.23)$$

where p_A and p_B are the sorbate pressure for A and B component, respectively. q_A and q_B are the adsorbed phase concentration for A and B component, respectively and calculated by using Langmuir model.

The chromatographic methods has also the advantage to provide information on the adsorption kinetics. Kinetic separations are used especially with molecular sieve adsorbents such as zeolites. The kinetic selectivity is determined by the ratio of intracrystalline diffusivities for the components (Ruthven, 2011; Ruthven and Reyes, 2007) given in Equation 5.24.

$$S_{AB} = \frac{K_A}{K_B} \sqrt{\frac{D_A}{D_B}} \quad (5.24)$$

5.4. Thermodynamics of Gas Adsorption

Heats of Adsorption

Heat of adsorption can provide useful information about the nature of the adsorbent surface and adsorbed phase. The temperature dependence of the Henry constant obeys the Vant Hoff equation gives heat of adsorption (Ruthven, 1984).

$$\Delta H_o = RT^2 \left[\frac{d \ln K(T)}{dT} \right] \quad (5.25)$$

where, ΔH_0 (kJ mol^{-1}) is the limiting heat of adsorption at low loading (in the Henry's law region), R ($\text{kJ mol}^{-1} \text{K}^{-1}$) is the ideal gas constant, K is the Henry's law adsorption equilibrium constant, T (K) is the temperature. Equation (5.25) can be integrated to get;

$$K(T) = K_0 \exp\left[-\frac{\Delta H_0}{RT}\right] \quad (5.26)$$

where K_0 is the pre-exponential factor. In accordance with Equation (5.26), plots of $\ln K$ versus $1/T$ are found to be linear over a wide range of temperature and the slopes of the plot give heat of adsorption.

Heat of adsorption has been related to several interaction energies at low level adsorption. These are dispersion and repulsion energies, polarization energy and electrostatic energy which are caused by the interaction of the local electrostatic fields in the zeolite with molecules possessing dipole moment or quadrupole moments (Breck, 1974). The magnitude of these interactions has been related to heat of adsorption.

Activation Energy

The temperature plays a very important role on the diffusion process. In general, the temperature dependence of the diffusion coefficient is given by Arrhenius equation:

$$D_c = D_0 \exp\left(-\frac{E_a}{RT}\right) \quad (5.27)$$

where D_0 ($\text{m}^2 \text{s}^{-1}$) is the pre-exponential factor of the diffusion process independent from the temperature, E_a (J mol^{-1}) is the activation energy for adsorbates in a given adsorbent, R ($\text{J mol}^{-1}\text{K}^{-1}$) is the gas constant, and T (K) is temperature.

CHAPTER 6

EXPERIMENTAL STUDIES

The zeolite NaX (CAS:63231-69-6) was used as adsorbent in the size of 2 μm (Aldrich). $\text{CeCl}_3 \cdot 7\text{H}_2\text{O}$ (Aldrich, lot number: S37173-356), $\text{CaCl}_2 \cdot 2\text{H}_2\text{O}$ (Merck, lot number: S24294-294) and LiCl (Merck, lot number: B468179-451) were used as salt solution to perform ion exchange experiment. High purity ($> 80\%$) of Sepiolite in the size of $< 105 \mu\text{m}$ supplied by Anadolu Endustri Mineralleri A.S. and Montmorillonite ($< 75 \mu\text{m}$) provided by Esan Eczacıbaşı were used as binder to provide granule formation of NaX zeolite. High purity of N_2 ($> 99.999 \%$), CH_4 ($> 99.95 \%$) and CO_2 ($> 99.995 \%$) were used as adsorbates. He (99.999%) was used as carrier and purge gas to activate and regenerate of the zeolites.

In the characterization of the materials TGA, XRD, FT-IR, SEM, ICP-AES, Volumetric Adsorption, Vicker hardness test and attrition test were used. Thermal properties of the zeolites were analyzed by thermobalance (Shimadzu TGA-51/51H) and scanned up to $1000 \text{ }^\circ\text{C}$ at heating rate of $10 \text{ }^\circ\text{C}/\text{min}$. Nitrogen atmosphere ($40 \text{ ml}/\text{min}$) were used for all analyses. Mineralogy and crystallinity of the zeolite samples were determined by X-ray diffraction (Philips X-Pert Pro Diffractometer) using $\text{CuK}\alpha$ radiation at 45 kV and 40 mA in the $2\theta : 5^\circ - 70^\circ$ with 0.2° step size. The micrographs of the zeolite crystals were taken by using scanning electron microscopy (SEM, Philips XL 30S) with LFD and ETD detector at 5.00 and 3.00 kV under vacuum conditions.

FT-IR analysis was performed with Shimadzu FT-IR 8201. About 3 mg of a powder form of zeolites with or without binders were taken and completed to 150 mg with KBr used to remove scattering effects. This powder mixture is then pressed into a pellet with a thickness of about 1 mm to form homogenous and transparent in appearance. FT-IR spectra were recorded at $400 - 4000 \text{ cm}^{-1}$. Chemical composition of the zeolites were determined by fusion dissolution technique. The supernatants were also analysed after centrifugation the ion exchange mixture by means of centrifuge (Rotofix 32-Hettich). In Fusion dissolution technique, 0.1 gram of the zeolite samples were mixed with 1 gram of $\text{Li}_2\text{B}_4\text{O}_7$. The dry-powder mixture was placed in a platinum crucible and fused in an oven at $1000 \text{ }^\circ\text{C}$ for 1 hour . After that, samples were dissolved

in aqueous solution including HNO₃ (5 % v/v). By adding deionized water, solutions were completed to 250 mL and presented to Inductively Coupled Plasma Atomic Emission Spectroscopy (ICP-AES, 96, Varian). Textural properties of zeolites such as surface area were determined by using a volumetric adsorption instrument (Micromeritics, ASAP 2010). Prior to adsorption, the samples were degassed for 24 h under vacuum better than 10⁻⁵ mbar at 350 °C. Surface area was determined from nitrogen adsorption data at 77 K. The Vicker hardness test is the standard test method to measure combination of the load applied and indenter geometry. To determine the hardness of the zeolites, Zwick/Roell Microhardness test (ZHU 2.5) was used at 9.8 N loading (HV1). ASTM E 728-91, a standard test method, was used to determine the resistance of granular samples to attrition. It was determined by placing granules (2.36 mm -1.7 mm) on a 1.7 mm sieve and vibrating with a common sieve shaker (Retsch) for five minutes at 20 and 50 amplitudes. The amount of granules passing the 1.7 mm sieve was measured as the attrition loss percentage.

6.1. Ion Exchange Studies

The ion exchange experiments were carried out by contacting the zeolite (NaX) with 2 M LiCl, 2 M CaCl₂.2H₂O solution including 3, 6 and 9 fold equivalent excess Li⁺, Ca²⁺ ions, respectively and 0.08 M CeCl₃.7H₂O solution including 3, 5, 6 and 9 fold equivalent excess Ce³⁺ ions in solution at 50 °C and 70 °C. Equivalent is the amount of counter ions (Li⁺, Ca²⁺ and Ce³⁺ ions) theoretically needed to completely exchange the Na⁺ ions of NaX zeolite.

The stock solution was prepared using ultrapure water for all ion exchange studies. pH of the Li⁺, Ca²⁺ and Ce³⁺ solutions was kept approximately at 7.2 ± 0.5, 5.7 ± 0.25 and 5.5 ± 0.25, respectively. Suitable pH was selected to prevent hydrolysis and breakdown of the zeolite structure during the ion exchange process according to the literature. The suspensions were centrifuged (Rotofix 32, Hettich) and then washed several times to obtain the zeolites Cl⁻ free.

The ultrasound processor (Sonics-Vibra Cell 505) with 20 ± 0.050 kHz frequency and 25 and 40 % of acoustic power (500 W) were used in the ion exchange experiment. The processor has the replaceable probe tip having ½” (13 mm) diameter. As seen from the Figure 6.1, the temperature of the solution sonicated was maintained

with circulating water and the probe was dipped to a depth of 15 mm. NaX zeolite and the solution including the ions were agitated in a cylindrical beaker. Ultrasonic bath at 35 kHz and 320 W was also used in order to perform the ion exchange at different frequency and power. Traditional batch ion exchange experiments were performed in the water bath shaker (GFL 1092) at 130 rpm. All experiments were provided for a sufficient time to enable the system to approach equilibrium. Table 6.1 shows the experimental conditions in detail.

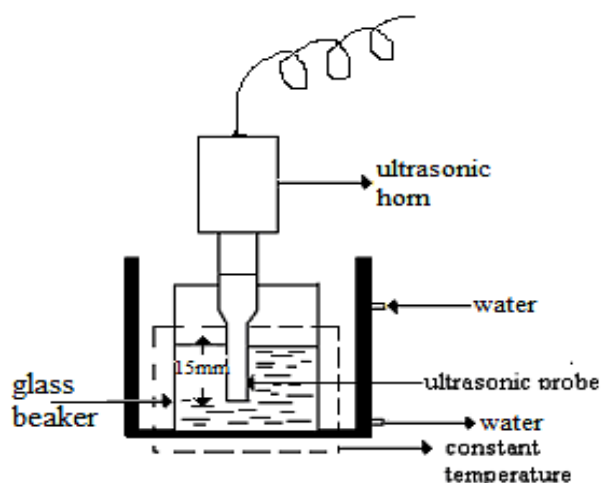


Figure 6.1. Experimental set-up of ultrasonic processor.

Consecutive ion exchange study in which the solution was refreshed five times for each 30 min was applied to obtain fully exchanged zeolite. Li^+ and Ca^{2+} ion solutions with 9 fold equivalent excess and Ce^{3+} ion solution with 5 fold equivalent excess were used in consecutive studies.

In the code of the samples, the numbers (3, 5, 6 or 9) and the following letters were used for the fold equivalent excess and the exchange method; traditional (T) and ultrasound (U). Excess fold: Mixture (including zeolite and solution contains $\text{CaCl}_2 \cdot 2\text{H}_2\text{O}$, CeCl_3 or LiCl) includes fold equivalent excess of the entering ion (Li^+ , Ca^{2+} , Ce^{3+}) with respect to the leaving ion (Na^+).

Table 6.1. Experimental parameters for Li⁺, Ca²⁺ and Ce³⁺ ions exchange at 50 °C and 70 °C.

Counter ions	Fold Equivalent Excess	Speed of water bath shaker (rpm)	Power of ultrasonic bath (W)	Frequency of ultrasound (kHz)	Period of time (h)	Consecutive solution times
Li ⁺	3	130	125	20	0.25 - 5	—
	6		125	20		—
	9		125, 200, 320	20, 35		5
Ca ²⁺	3	130	125	20	0.25 - 5	—
	6		125	20		—
	9		125, 200, 320	20, 35		5
Ce ³⁺	3	130	125	20	0.25 - 5	—
	5		125, 200, 320	20, 35		5
	6		125	20		—
	9		125	20		—

6.2. Granule Formation of NaX Zeolite

The zeolite granules were prepared by using montmorillonite and sepiolite, as inorganic binders. Mixing of zeolite and the binder with distilled water was resulted in a thick suspension. After the kneading, the formed bodies were air-dried and followed by oven drying. Two procedures (A and B) were used to obtain granule form of zeolite. Difference between these procedures is to apply pressure (2.6 metric tons) to make zeolite pellet in procedure B. Then, samples were subjected to high-temperature heating to destroy the surface area and activity of the binder during the process. Finally, the zeolite pellets were crushed and sieved to get granule form. The schematic diagram of experimental procedures is given in Figure 6.2. In the code of the samples, NaX-S and NaX-M were used for NaX zeolite including Sepiolite mineral and Montmorillonite mineral as binders, respectively.

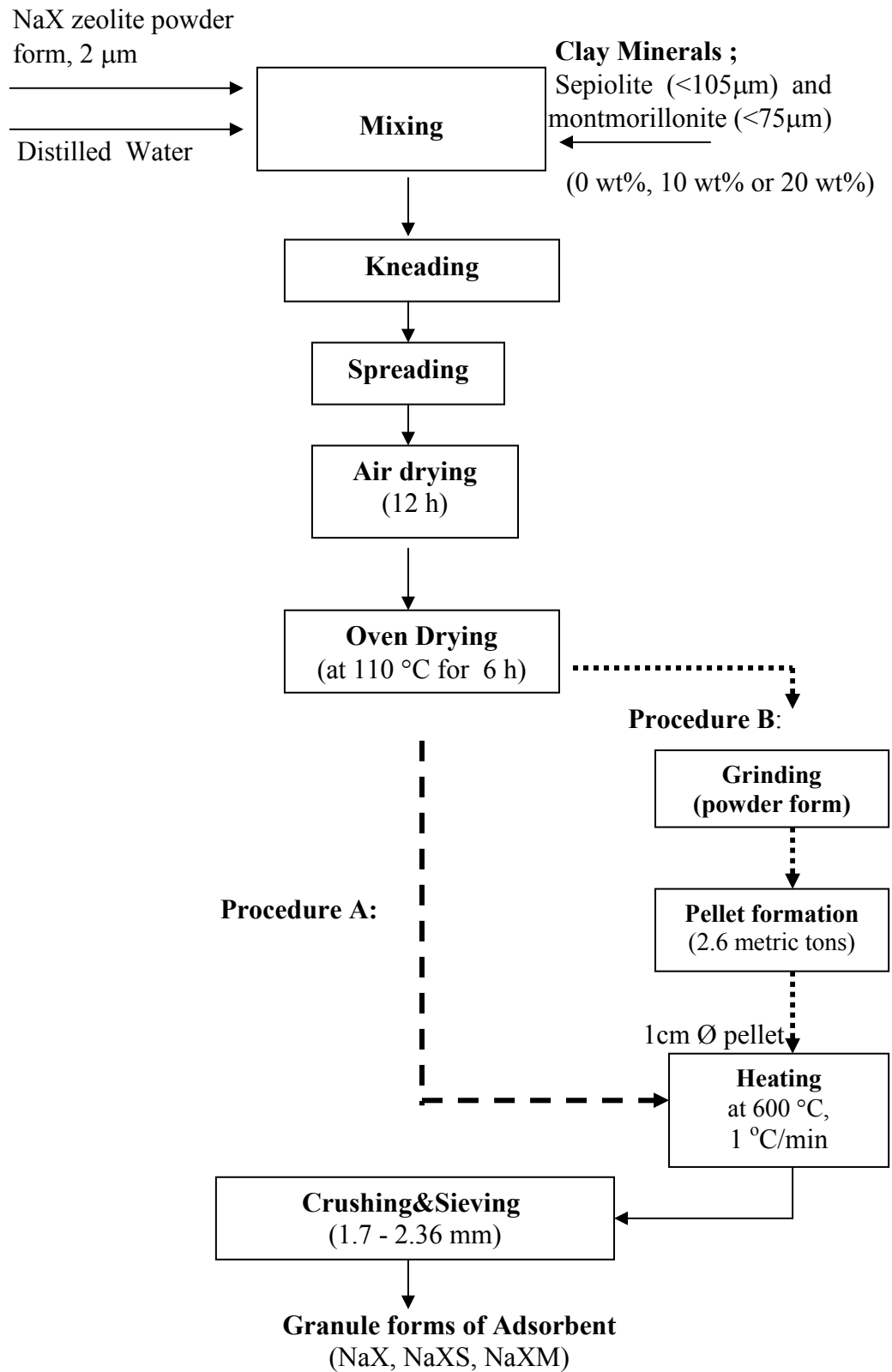


Figure 6.2. Flow sheet for preparation of NaX granule.

6.2.1. Measurement of True Density

Helium densitometer based on the principle of $PV = \text{constant}$ at constant temperature was used to determine the true density. A known amount of porous sample (W_s) is put into closed vessel of volume V_1 . Nonadsorbable gas such as helium is introduced to an evacuated vessel to reach pressure P_1 . After valve is closed, the volume of the vessel changes by moving the piston as ΔV . Change in pressure, ΔP , is also obtained (Figure 6.3). Calculation of true density is given below;

$$V_s = V_1 - (P_1 / \Delta P - 1) \Delta V \quad (6.1)$$

$$\rho_{\text{true}} = W_s / V_s \quad (6.2)$$

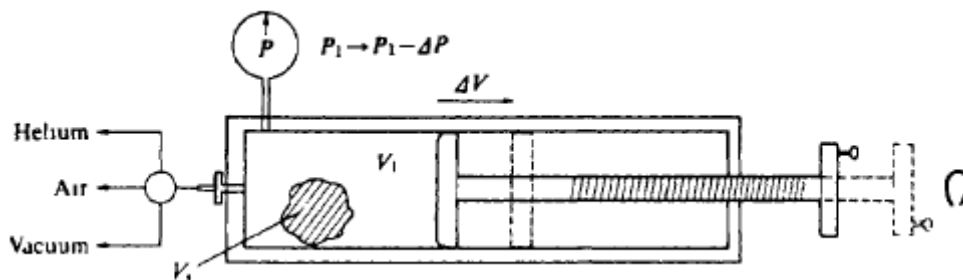


Figure 6.3. Displacement type pycnometer (helium densitometer).
(Source: Suzuki,1990)

6.3. ZLC Adsorption System

CO_2 , CH_4 and N_2 adsorption on the zeolites from consecutive ion exchange obtained by ultrasonic method was studied to determine Henry's constant and diffusion coefficient by using the home-made ZLC system (Figure 6.4). The system includes adsorbent zero length column, oven (Binder ED 53), gas flow controllers (Aalborg, DFC 26) and mass spectrometer (Hiden HPR 20). Water vapour trap (Agilent) was placed before the mass flow controllers to reduce detoriot effect of water vapor on gas adsorption. Simplified zero length column configurations were seen in Figure 6.4.

The ZLC cell consists of a small amount (≈ 2 mg) of adsorbent powder ($2\mu\text{m}$) sandwiched between two sintered discs (Alltech) in a $1/8$ -in. Swagelok fitting. Quartz wool was used to close remaining space of ZLC cell and prevent zeolite crystals to escape the mass spectrometer (MS). All the connections in the system were periodically inspected for leakage with a solution of water and soap.

The ZLC is located into an oven to regenerate and perform the adsorption experiments at desired temperature. Regeneration at $250\text{ }^\circ\text{C}$ (1K heating ramp) removes water vapor and some impurities by using a flow of helium at 10ml/min for 14h. The adsorbent into ZLC was exposed to a diluted stream of a sorbate in an inert (helium) gas. Therefore, 3 % vol. of sorbates (N_2 , CH_4 , CO_2), as the initial concentration was applied in order to describe the equilibrium by Henry's law. Measurements was carried out at 303, 333 and 363 K. Finally, purging with inert gas (He) was carried out at 70 ml/min to obtain desorption (response) curve. The flow rates of both the adsorbative and purge streams were controlled by mass flow controllers. The effluent concentration of the desorption/response curves was recorded in digital form for data processing.

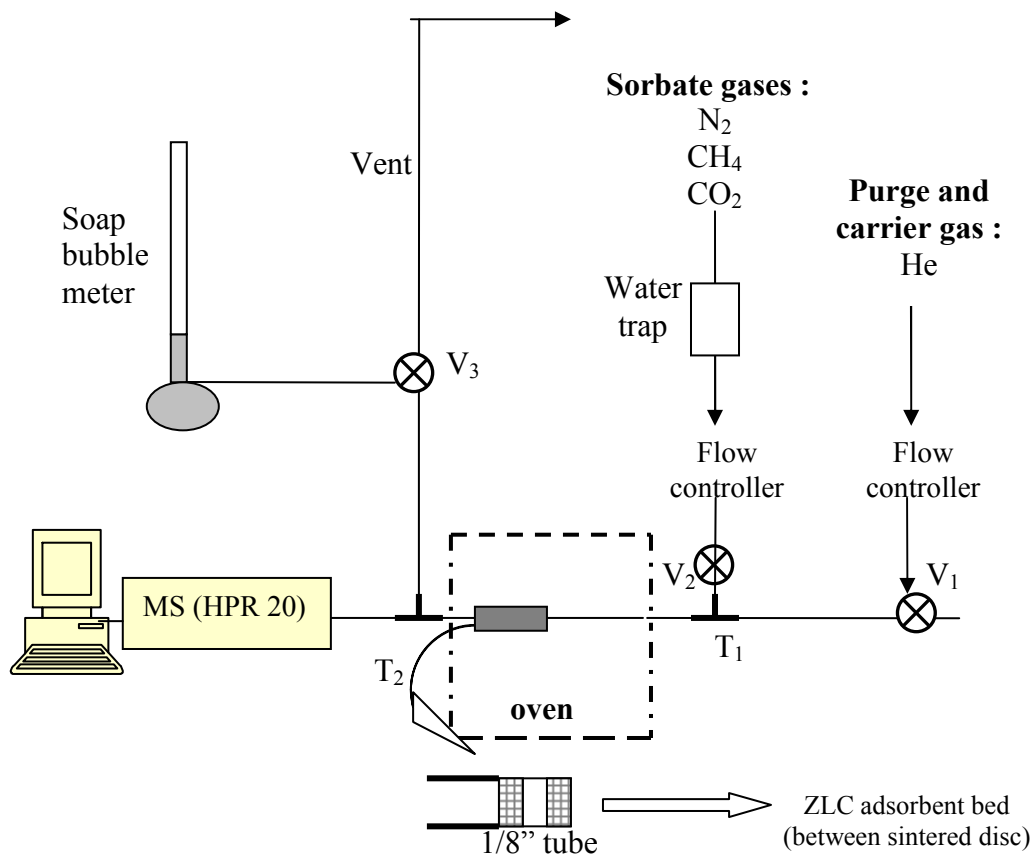


Figure 6.4. Zero Length Column configurations.

6.3.1. Data Collection and Analysis

The software of the mass spectrometer (MASsoft Professional) was used to collect the data. The response curve (pressure versus time) is directly proportional to the concentration of the sorbate in the effluent stream. The analysis of ZLC response curve data requires the response curves was normalized relative to the initial concentration.

To normalize that the response curve, following Equation 6.3 was used (Brandani, 2002);

$$\frac{c(t)}{c_0} = \frac{\sigma(t) - \sigma_{\text{inf}}}{\sigma_0 - \sigma_{\text{inf}}} \quad (6.3)$$

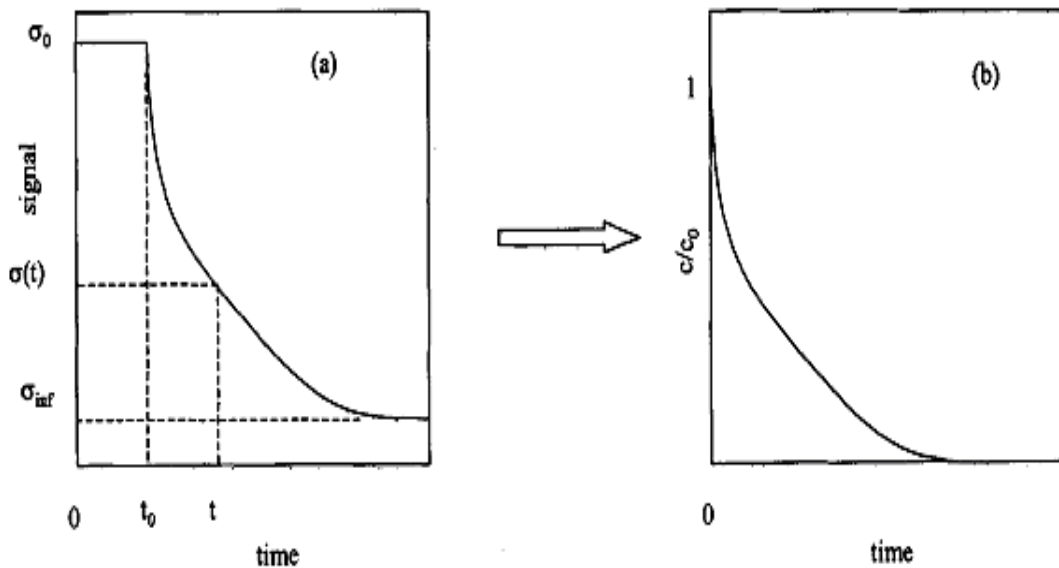


Figure 6.5. Qualitative (a) Raw ZLC response and (b) Normalized response curve.

As seen in Figure 6.5, σ_0 is the value of the signal at time zero given as pressure and σ_{inf} is the value of the signal as pressure when the desorption is completed.

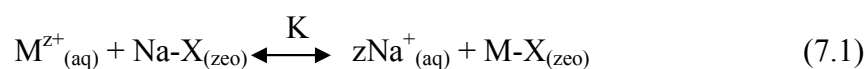
CHAPTER 7

RESULTS AND DISCUSSIONS

The exchange of Li^+ , Ca^{2+} and Ce^{3+} ions into NaX framework were performed and the zeolites obtained were characterized by TGA, ICP-AES, N_2 adsorption at 77 K, SEM, XRD, FTIR methods. CO_2 , N_2 , CH_4 adsorption on the exchanged zeolites were also studied in zero length column (ZLC).

7.1. Ion Exchange Studies

The effect of the concentration of the counter ions, the cations (Li^+ , Ca^{2+} and Ce^{3+}) to be introduced, temperature in the exchange were examined kinetically in the presence of ultrasound. In consecutive studies, the counter ion solution were refreshed five times. The results were compared with those obtained from traditional batch method. Exchange reaction between the counter ions, M^{z+} , and NaX zeolite;



where K is the rate constant of the exchange reaction and defined as the ratio of forward reaction rate to reverse reaction rate. Exchange percent of Na^+ ion (η_{Na}) was calculated;

$$\eta_{\text{Na}} = \left(\frac{q_o - q_{\text{Na}}}{q_o} \right) \times 100 \quad (7.2)$$

where q_o and q_{Na} (mg g^{-1}) are the amount of Na^+ ions into zeolites initially and at any time t, respectively.

7.1.1. Kinetic Studies

Kinetics of ion exchange from counter ion solutions in the concentration range of 3-9 fold equivalent excess were studied at 50 °C and 70 °C with both methods; ultrasonic and traditional. Additionally the ion exchange was studied in ultrasonic bath to understand the effect of source. Figures 7.1-7.6 show the kinetic curves of ion exchange.

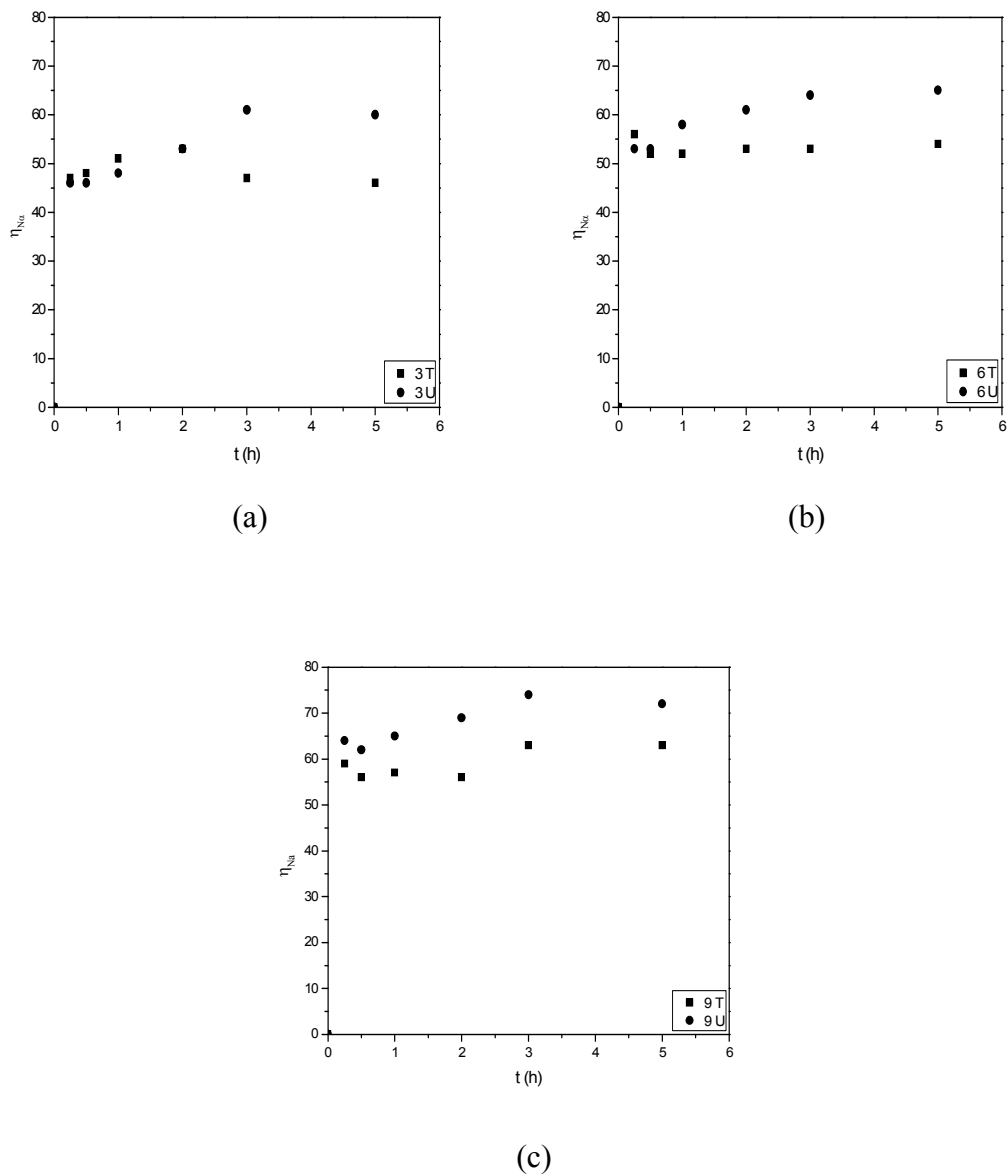
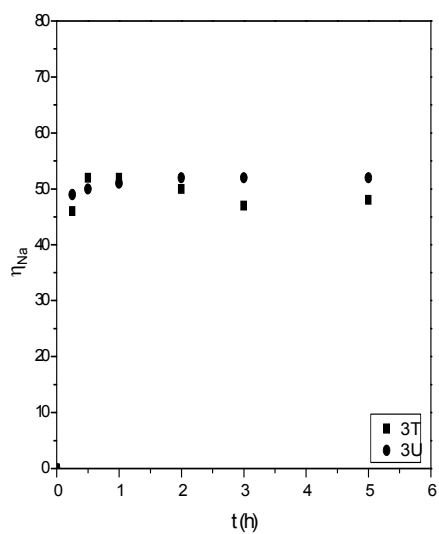
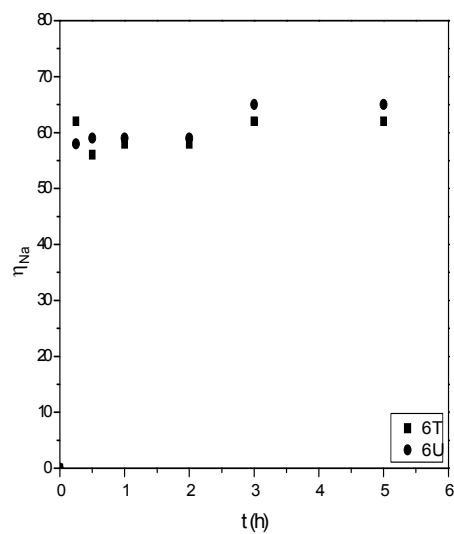


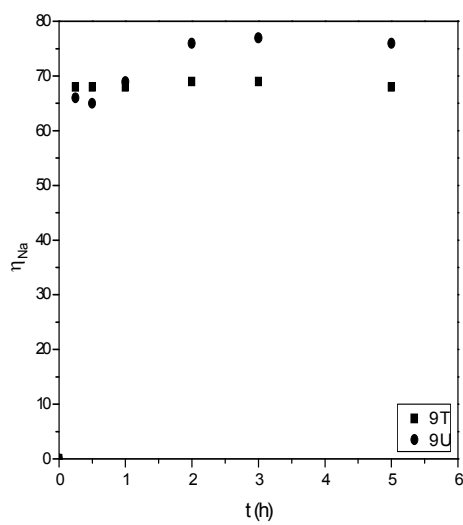
Figure 7.1. Kinetic curves of Li^+ ion exchange at 50 °C (fold equivalent excess: (a) 3 (b) 6 (c) 9).



(a)

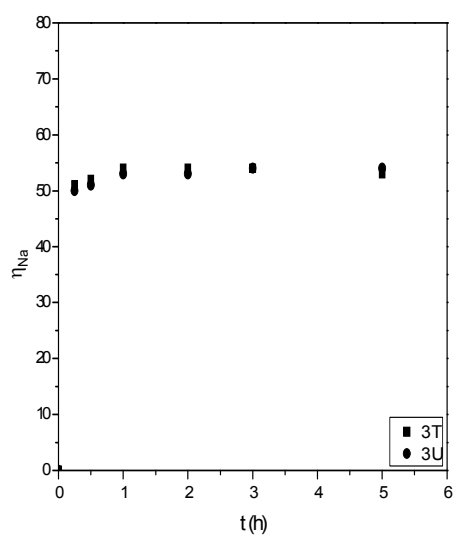


(b)

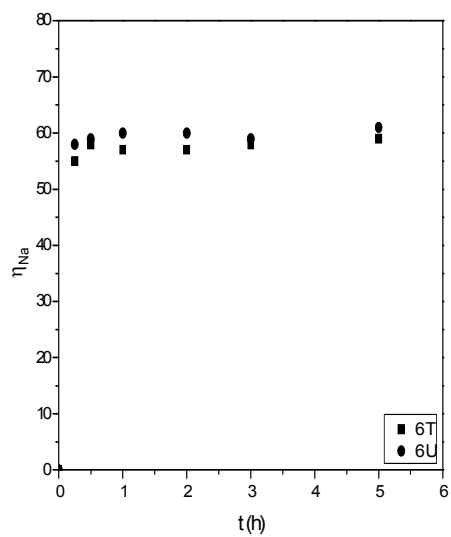


(c)

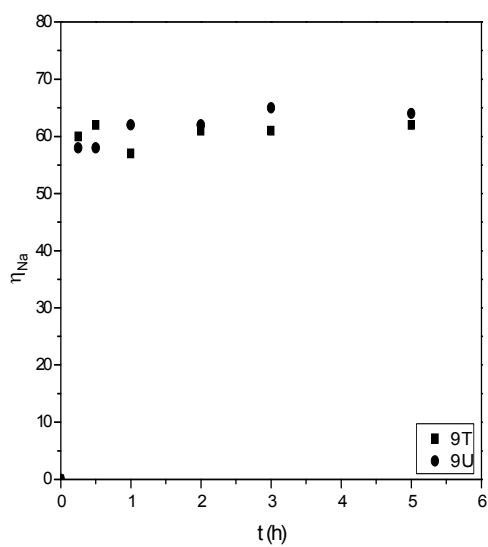
Figure 7.2. Kinetic curves of Li^+ ion exchange at $70\text{ }^\circ\text{C}$ (fold equivalent excess: (a) 3 (b) 6 (c) 9).



(a)

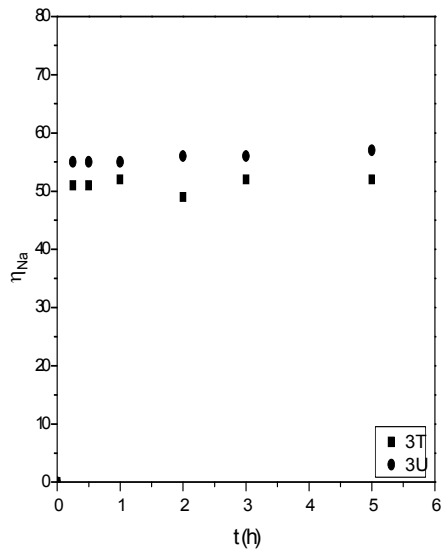


(b)

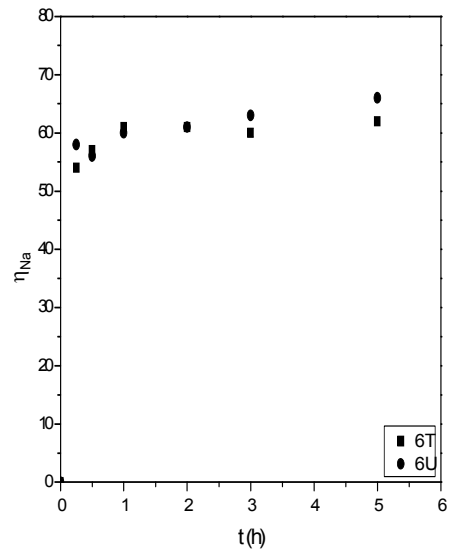


(c)

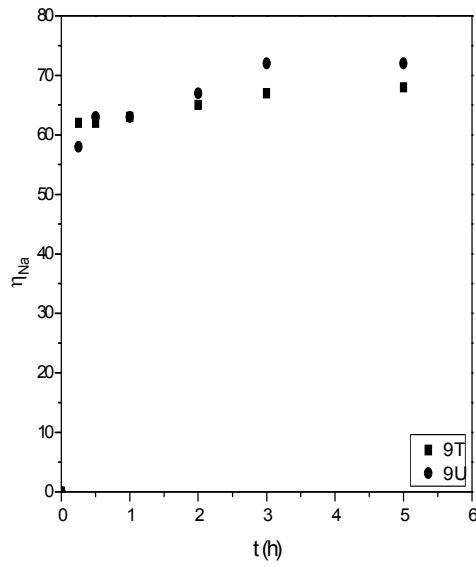
Figure 7.3. Kinetic curves of Ca^{2+} ion exchange at $50\text{ }^{\circ}\text{C}$ (fold equivalent excess: (a) 3 (b) 6 (c) 9).



(a)

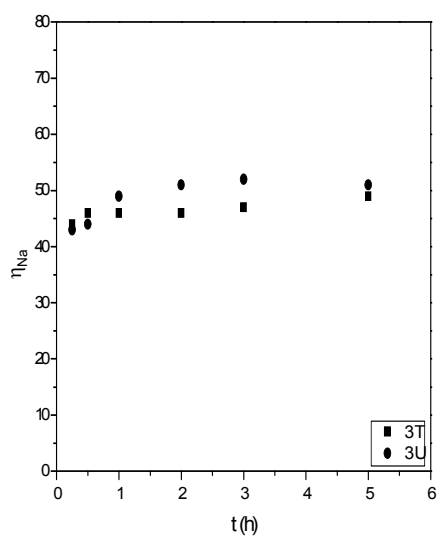


(b)

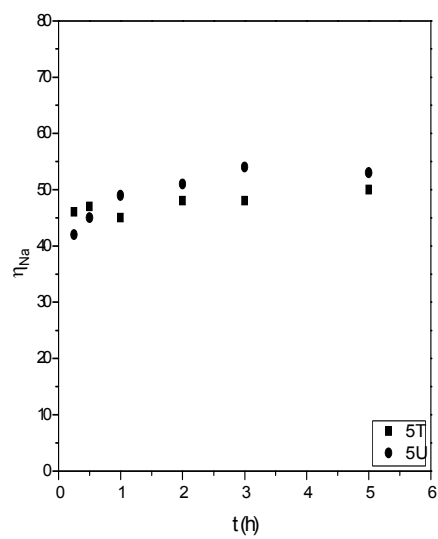


(c)

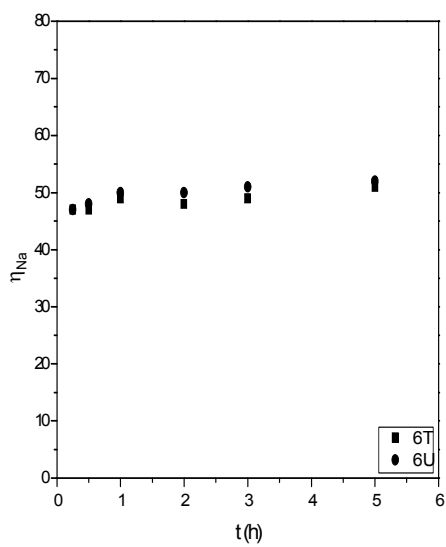
Figure 7.4. Kinetic curves of Ca^{2+} ion exchange at 70°C (fold equivalent excess: (a) 3 (b) 6 (c) 9).



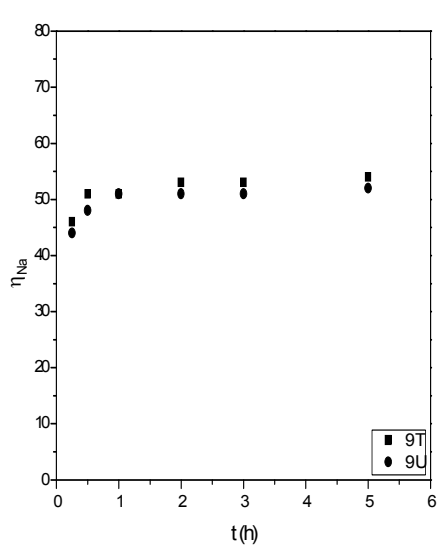
(a)



(b)

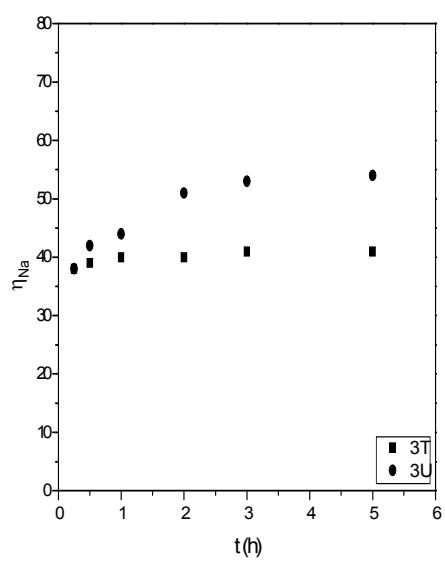


(c)

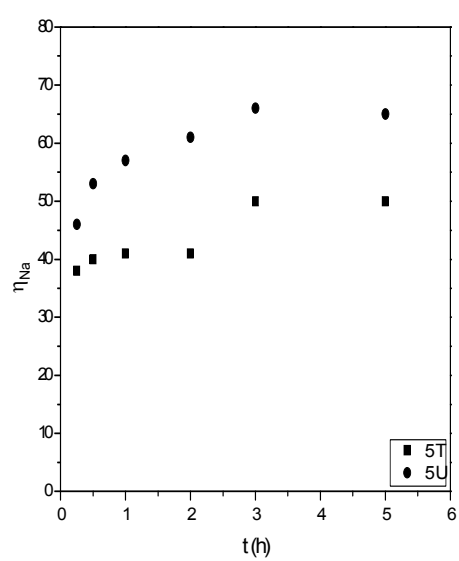


(d)

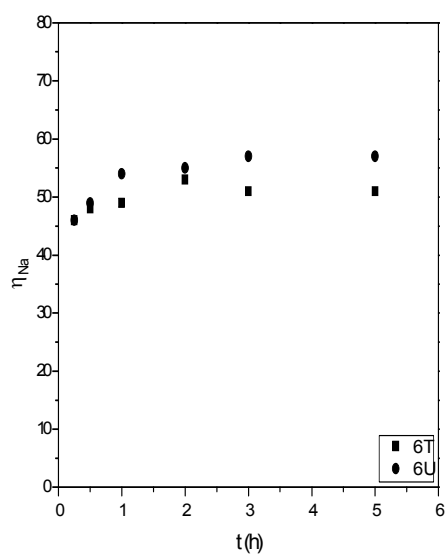
Figure 7.5. Kinetic curves of Ce^{3+} ion exchange at 50 °C (fold equivalent excess: (a) 3 (b) 5 c) 6 (d) 9).



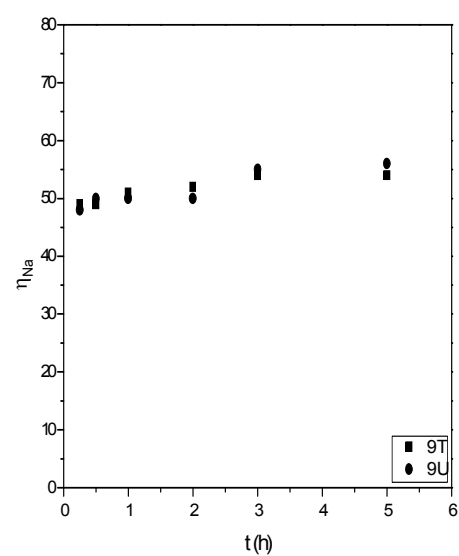
(a)



(b)



(c)



(d)

Figure 7.6. Kinetic curves of Ce^{3+} ion exchange at 70°C (fold equivalent excess: (a) 3 (b) 5 c) 6 (d) 9).

As seen from the kinetic curves, the exchange is very fast and completed within about 15 min. The exchange percents were increased with temperature and the fold equivalent excess used and given in Appendix A. Maximum exchange percent was obtained as 76, 72 and 66 for Li^+ , Ca^{2+} and Ce^{3+} ions exchange, respectively. Fully exchanged NaX zeolite was not obtained at the end of the ion exchange. It was observed that the fold equivalent excess, temperature and ultrasound are more effective in Li^+ ion exchange than Ca^{2+} and Ce^{3+} ions exchanges.

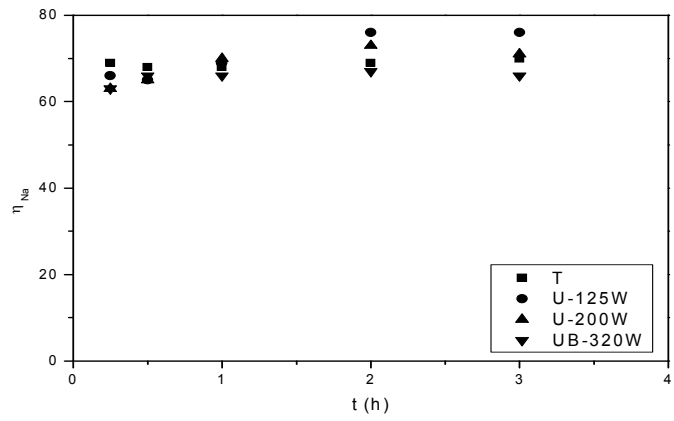
Effect of ultrasonic source

Li^+ , Ca^{2+} and Ce^{3+} ions exchange in ultrasonic bath were examined to show the effect of ultrasonic sources. The conditions of ultrasound experiments are tabulated in Table 7.1.

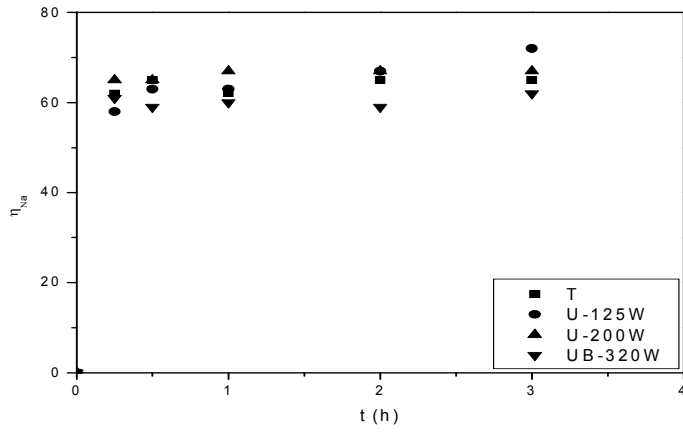
Table 7.1. The experimental conditions and the zeolites obtained.

Codes	Ultrasonic Sources	Power	Frequency (kHz)
U-125W	Probe	125	20
U-200W	Probe	200	20
UB-320W	Bath	320	35

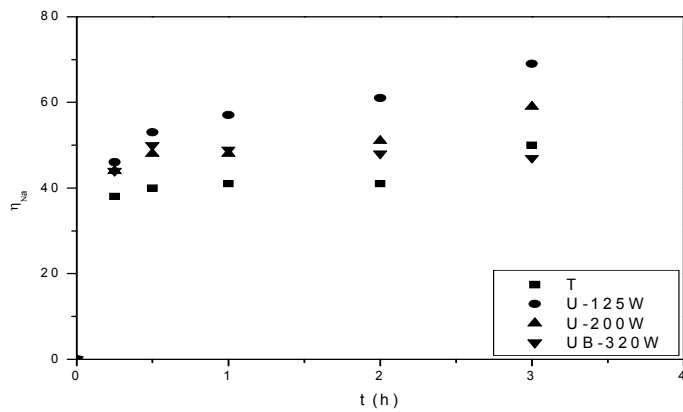
Figure 7.7 shows the kinetic curves of Li^+ , Ca^{2+} and Ce^{3+} ions exchange, respectively. As seen from the Figure, ultrasonic probe is more effective than ultrasonic bath in the exchange. Although ultrasonic probes deliver their energy on a localized zone, it provides a great many transient cavitation bubbles not only in the fluid phase surrounding the particles but also in the solution within the porous particles. Therefore it was observed that ultrasonic probe method enhanced the exchange compared with the traditional and ultrasonic bath methods. Generally, the ion exchange in ultrasonic bath is lower than traditional batch method (T). The exchange percent is changed depending on the method used: $\text{U-125W} > \text{U-200W} > \text{T} \geq \text{UB-320W}$.



(a)



(b)



(c)

Figure 7.7. Kinetic curves at 70 °C for exchange of (a) Li⁺ (b) Ca²⁺ (c) Ce³⁺ ions.

Low exchange percent was obtained when high power (> 25 % acoustic power) was applied from ultrasonic probe. This acoustic power through the liquid causes large number of cavitation bubbles many of which coalesce into larger, longerlived bubbles hindering the exchange as stated by Castro and Capote, (2007).

The kinetic models: reaction (pseudo first and second order) and diffusion models were used to identify the effect of ultrasound on the mass transfer mechanism. Limiting controlled step or steps which are pore (internal) diffusion, external film diffusion and/or reaction kinetics at phase boundaries were investigated by fitting the data with the models. In regression the aim is to decrease the sum of square of error, SSE:

$$SSE = \sum \left[\frac{(q - q_{theo})^2}{q^2} \right] \quad (7.3)$$

where q and q_{theo} are the experimental and theoretical amount of counter ions in zeolite, respectively.

Reaction Models: Pseudo first and second order

The pseudo reaction models are used for solid-liquid systems to provide the equilibrium exchange amount and rate constant. As seen from the Table 7.2 and 7.3, high correlation coefficients were obtained with pseudo second order reaction ($0.98 < R^2 < 0.99$) comparing to the pseudo first order reaction model ($0.95 < R^2 < 0.99$). The rate constants of 1st order are lower than those of 2nd order reaction model. The equilibrium values obtained from the both models are consistent.

The exchange rate (the 2nd order reaction rate constant and initial rate exchange) for lithium was increased significantly with increasing fold equivalent excess and temperature in traditional method. Reverse behavior was observed when ultrasonic method was applied. The exchange rate is irregular for multivalent cations; calcium and cerium. The effect of hydrated radius of the counter ions on the exchange rate was not observed clearly.

Table 7.2. The reaction model parameters of cation exchange at 50 °C.

Counter ion*	Fold Equiv. Excess	Pseudo 1 st Order Reaction Model								Pseudo 2 nd Order Reaction Model									
		q _e (meqg ⁻¹)		k (min ⁻¹)		SSEx10 ⁴		R ²		q _e (meq g ⁻¹)		k (g meq ⁻¹ min ⁻¹)		h (meq g ⁻¹ min ⁻¹)		SSEx10 ⁴		R ²	
		T	U	T	U	T	U	T	U	T	U	T	U	T	U	T	U	T	U
Li ⁺ r _H =3.80Å	3	2.74	2.87	0.22	1.22	135	783	0.9918	0.9537	2.75	3.21	0.88	0.06	6.70	0.65	140	320	0.9914	0.9829
	6	2.99	3.28	1.06	1.31	38	405	0.9977	0.9776	2.99	3.57	0.81	0.07	7.27	0.94	70	90	0.9963	0.9954
	9	3.30	3.83	1.37	1.32	149	242	0.9911	0.9859	3.35	3.98	0.46	0.94	5.14	1.54	140	110	0.9919	0.9929
Ca ²⁺ r _H =4.12Å	3	1.51	1.51	0.20	0.19	10	19	0.9994	0.9989	1.54	1.54	0.72	0.50	1.70	1.20	6	4	0.9998	0.9998
	6	1.64	1.70	0.20	0.23	8	8	0.9995	0.9996	1.66	1.71	0.75	0.99	2.10	2.90	10	5	0.9995	0.9998
	9	1.72	1.77	0.33	0.17	51	71	0.9973	0.9960	1.75	1.81	1.52	0.31	4.60	1.02	1	27	0.9999	0.9985
Ce ³⁺ r _H =9.0Å	3	0.89	0.94	0.19	0.12	28	144	0.9982	0.9927	0.89	0.98	0.90	0.28	0.73	0.27	19	42	0.9988	0.9980
	5	0.90	0.96	0.23	0.11	59	145	0.9966	0.9922	0.91	1.01	1.26	0.22	1.05	0.22	47	31	0.9974	0.9983
	6	0.92	0.95	0.22	0.18	35	32	0.9979	0.9982	0.94	0.97	1.10	0.67	0.97	0.63	22	9	0.9987	0.9948
	9	0.99	0.96	0.14	0.13	20	20	0.9988	0.9988	1.02	0.99	0.39	0.36	0.41	0.35	9	5	0.9995	0.9997

*r_H:hydrated radius

Table 7.3. The reaction model parameters of cation exchange at 70 °C.

Counter ion*	Fold Equiv. Excess	Pseudo 1 st Order Reaction Model								Pseudo 2 nd Order Reaction Model									
		q _e (meqg ⁻¹)		k (min ⁻¹)		SSEx10 ⁴		R ²		q _e (meq g ⁻¹)		k (g meq ⁻¹ min ⁻¹)		h (meq g ⁻¹ min ⁻¹)		SSEx10 ⁴⁺		R ²	
		T	U	T	U	T	U	T	U	T	U	T	U	T	U	T	U	T	U
Li ⁺ r _H =3.80Å	3	2.79	2.89	0.18	0.20	89	11	0.9948	0.9994	2.79	2.93	0.62	0.33	4.85	2.82	88	1	0.9956	0.9999
	6	3.35	3.46	0.99	0.99	101	159	0.9943	0.9908	3.35	3.63	0.90	0.13	10.0	1.78	95	54	0.9940	0.9970
	9	3.84	4.00	1.00	0.99	3	199	0.9998	0.9887	3.87	4.23	1.15	0.10	17.3	1.76	1	53	0.9999	0.9969
Ca ²⁺ r _H =4.12Å	3	1.51	1.51	0.20	0.19	10	20	0.9994	0.9989	1.48	1.60	1.87	1.48	4.01	3.77	1	5	0.9999	0.9997
	6	1.71	1.74	0.14	0.19	31	144	0.9983	0.9918	1.76	1.79	0.25	0.29	0.78	0.93	10	80	0.9994	0.9973
	9	1.82	1.89	0.22	0.13	34	103	0.9964	0.9907	1.88	2.00	0.38	0.14	1.38	0.56	30	66	0.9983	0.9967
Ce ³⁺ r _H =9.0Å	3	0.76	0.93	0.19	0.09	16	373	0.9991	0.9808	0.77	0.99	1.06	0.16	0.64	0.16	3	103	0.9998	0.9940
	5	0.83	1.16	0.12	0.09	453	190	0.9720	0.9895	0.89	1.24	0.27	0.12	0.21	0.18	138	38	0.9907	0.9978
	6	0.95	1.04	0.16	0.11	52	104	0.9969	0.9946	0.98	1.08	0.51	0.22	0.49	0.27	23	17	0.9986	0.9992
	9	0.98	0.99	0.18	0.17	64	124	0.9963	0.9924	1.00	1.01	0.60	0.50	0.61	0.51	26	83	0.9985	0.9951

*r_H:hydrated radius

The equilibrium isotherms (q_e vs. C_e) for Li^+ , Ca^{2+} and Ce^{3+} ions exchange are presented in Figure 7.8, 7.9 and 7.10 respectively. C_e is counter ion concentration at equilibrium. Comparison of the methods shows that ultrasonic method due to “hot spots” is more effective than traditional method. Hot spots increase the temperature and pressure near the surface of the NaX zeolite leading to enhancement in ion exchange as observed in water softening (Entezari and Tahmasbi, 2009). The equilibrated values (q_e) were increased with increasing Li^+ and Ca^{2+} ions concentration in solution for both exchange methods. It seems to decrease an electrostatic interaction of the site with lower affinity when increased initial concentration of solution as stated by Al-Ghouti et al. (2009). In case of Ce^{3+} ion the effect of solution concentration on the equilibrium could not be observed. Thermodynamics analysis of ion exchange couldn't be possible because the effect of temperature on the exchange is not clear.

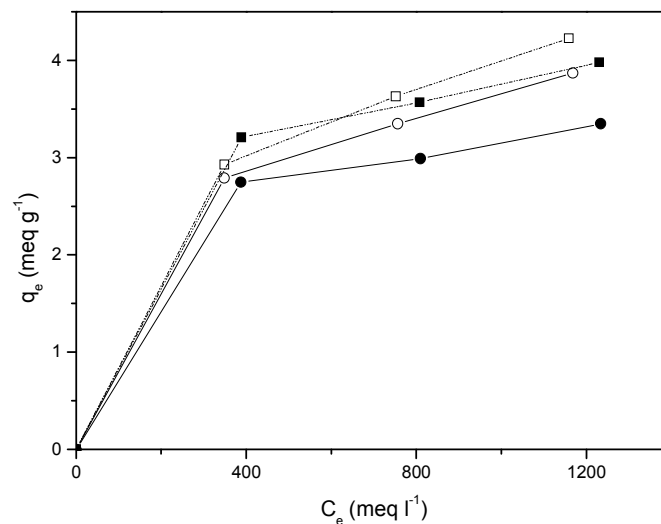


Figure 7.8. Li-exchange isotherm at 50 °C (■, ●) and 70 °C (□, ○) by using traditional (solid line) and ultrasonic (dashed line) method.

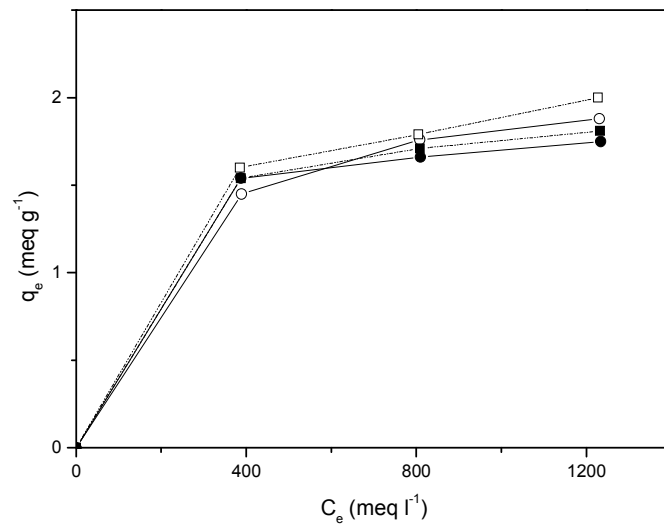


Figure 7.9. Ca-exchange isotherm at 50 °C (■, ●) and 70 °C (□, ○) by using traditional (solid line) and ultrasonic (dashed line) method.

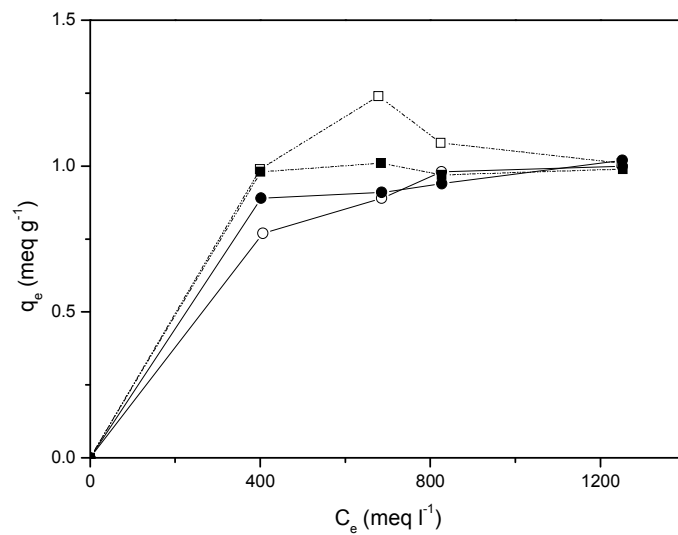


Figure 7.10. Ce-exchange isotherm at 50 °C (■, ●) and 70 °C (□, ○) by using traditional (solid line) and ultrasonic (dashed line) method.

Diffusion model: intraparticle and / or external

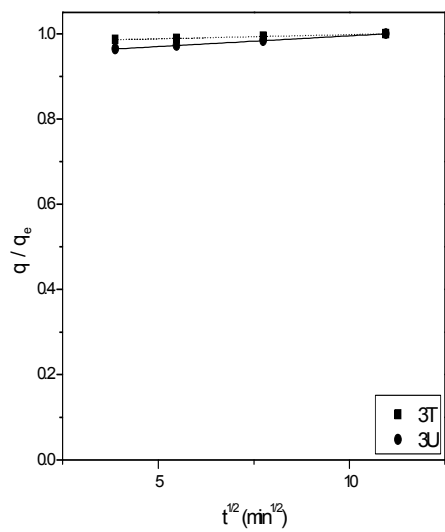
The intraparticle pore diffusion in the spherical particle with appropriate boundary conditions is solved analytically given in Chapter 4. In the initial region of diffusion process ($q/q_e < 0.3$), the analytical solution of is reduced to:

$$\frac{q}{q_e} = \frac{6}{\sqrt{\pi}} \left(\frac{Dt}{r^2} \right)^{1/2} \quad (4.14)$$

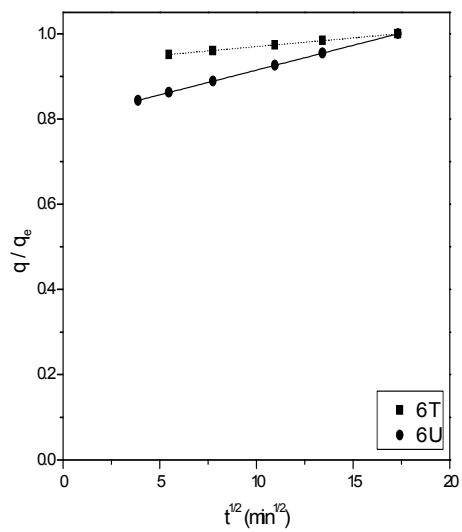
or

$$q = k_i t^{1/2} \quad (4.15)$$

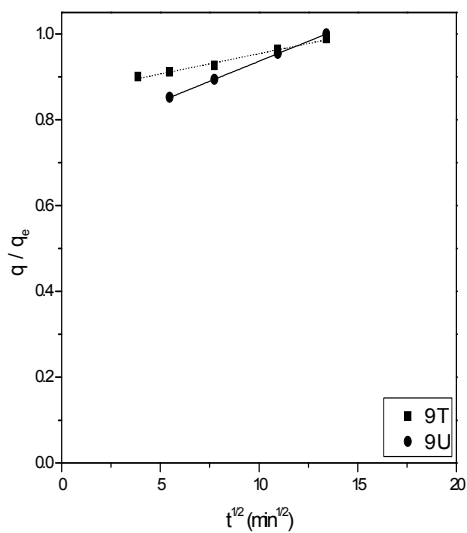
As seen from the Figures 7.11 - 7.16, the plot of q/q_e versus $t^{1/2}$ did not pass through the origin showing that the presence more than one resistance (intraparticle and/or external film) to the ion exchange. The experimental data collected were fitted to the model by reducing the error ($1 \times 10^{-4} < \text{SSE} < 99 \times 10^{-4}$). As seen from Table 7.5 and 7.6 correlation coefficients is in the range of 0.77 - 0.99. The intercept and the slope of the plot were used to calculate C and k_i values, respectively. For lithium and calcium exchange, intraparticle diffusion rate constant, k_i , the exchange rate of counter ion per gram zeolite, is increased significantly with the fold equivalent excess. The irregular change in the k_i values for cerium exchange is seen and could be related to agglomeration on zeolite surface at high fold equivalent excess which could block the pores and reduce the exchange rate. The rate constant, k_i , was high when ultrasonic method was used. Although the hydrated radius of Li^+ ion is higher than Na^+ ion, the rate constants of lithium ion into pore of the NaX zeolite was high significantly comparing to the Ca^{2+} and Ce^{3+} ions. Because ultrasound produces cavitation bubbles which are collapsed asymmetrically in a heterogeneous system resulted in microjet and shockwaves with high velocity on the surface of the zeolite. These actions can lead to reduce the hydrated radius of the Li^+ ion and increase the rate constants as stated by Hamdaoui and Naffrechoux (2007).



(a)

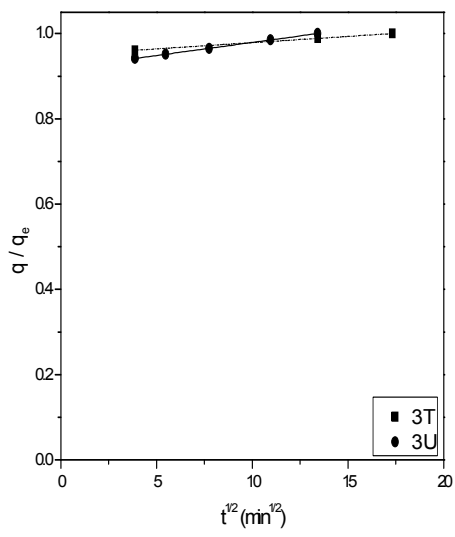


(b)

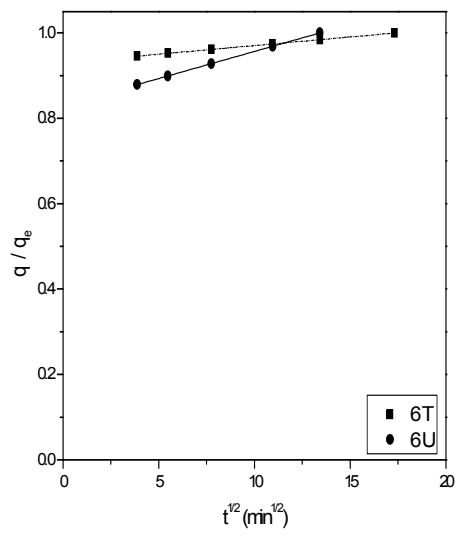


(c)

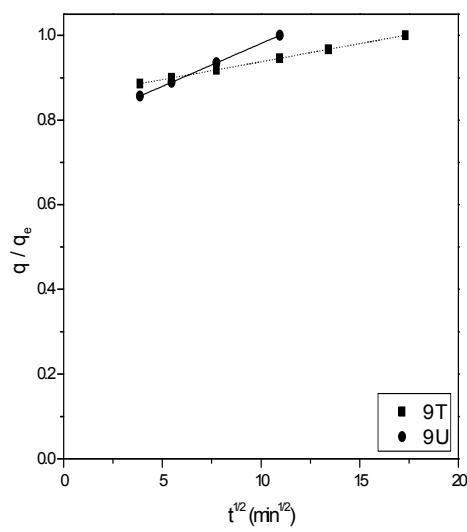
Figure 7.11. Intraparticle diffusion kinetic curves of Li- exchange at 50 °C (fold equivalent excess: (a) 3 (b) 6 c) 9).



(a)

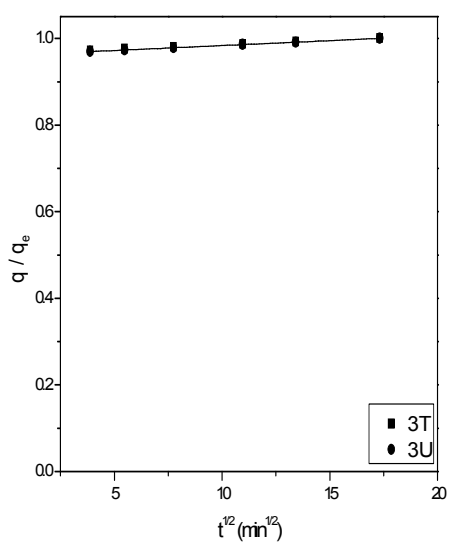


(b)

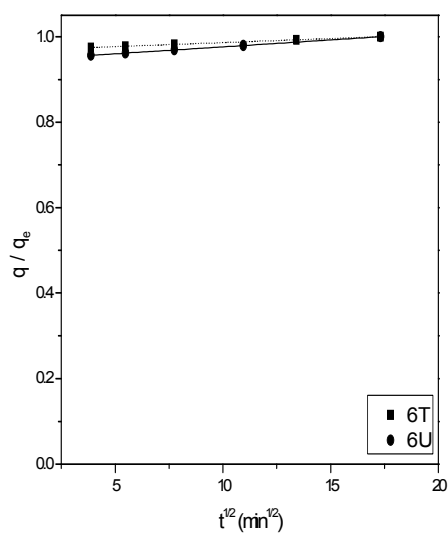


(c)

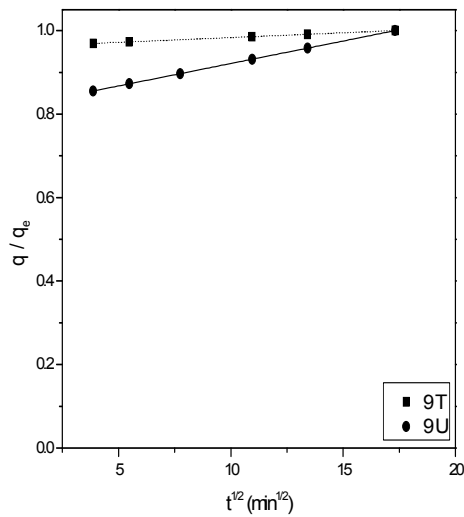
Figure 7.12. Intraparticle diffusion kinetic curves of Li- exchange at 70 °C (fold equivalent excess: (a) 3 (b) 6 c) 9).



(a)

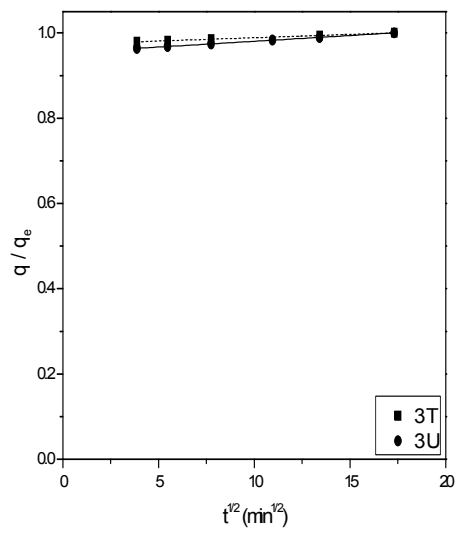


(b)

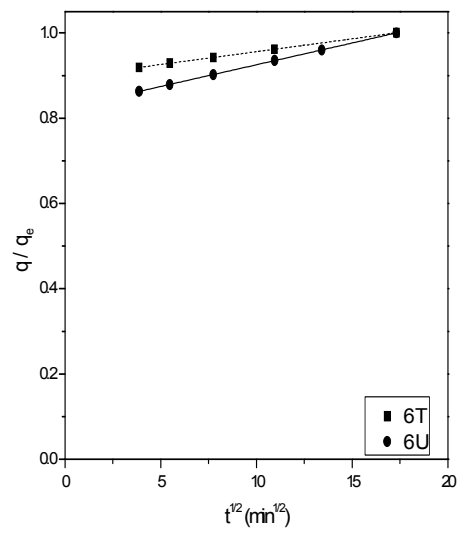


(c)

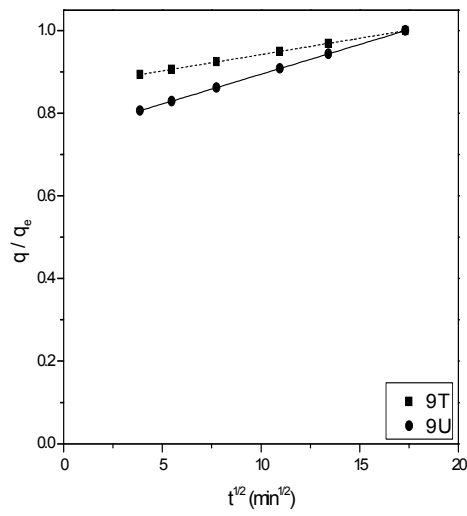
Figure 7.13. Intraparticle diffusion kinetic curves of Ca- exchange at 50 °C (fold equivalent excess: (a) 3 (b) 6 c) 9).



(a)

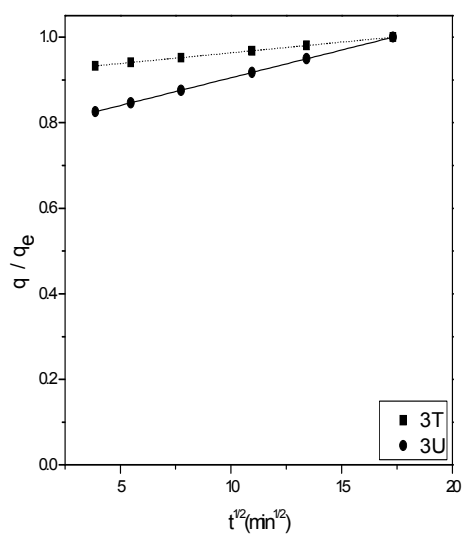


(b)

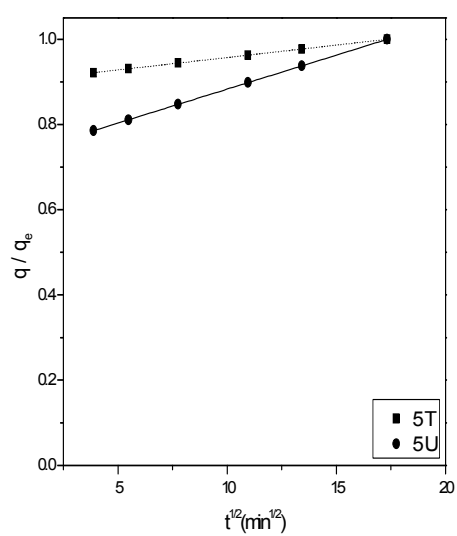


(c)

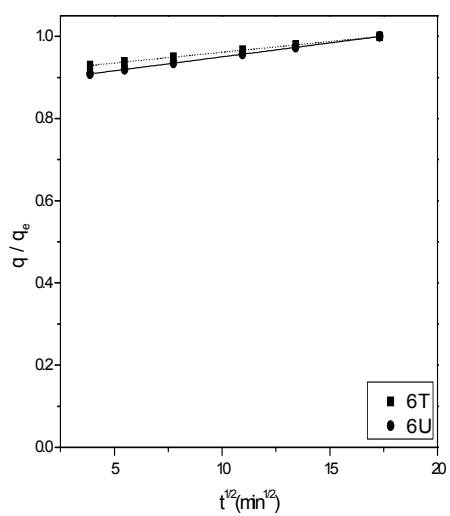
Figure 7.14. Intraparticle diffusion kinetic curves of Ca- exchange at 70 °C (fold equivalent excess: (a) 3 (b) 6 c) 9).



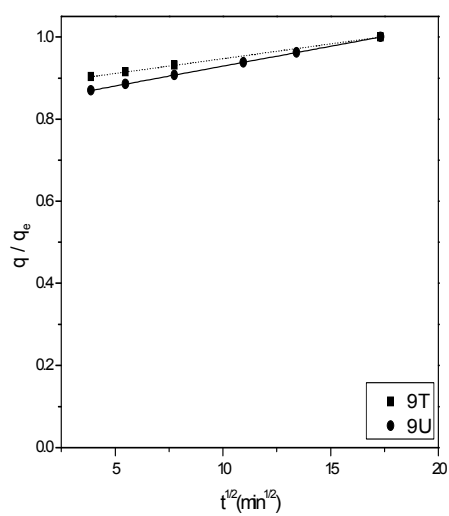
(a)



(b)

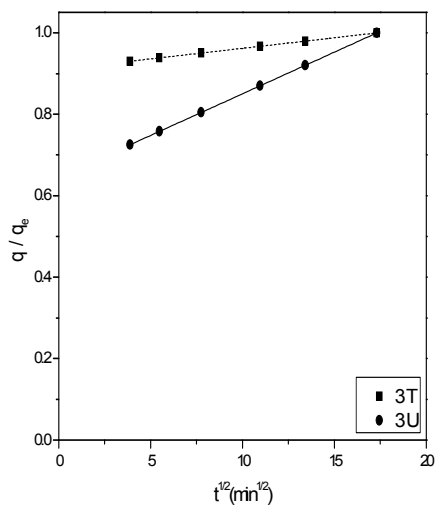


(c)

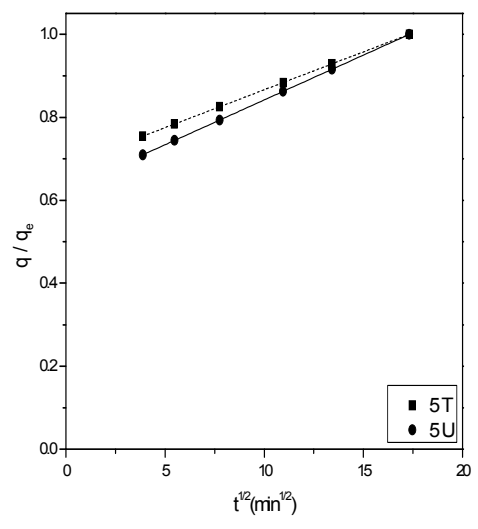


(d)

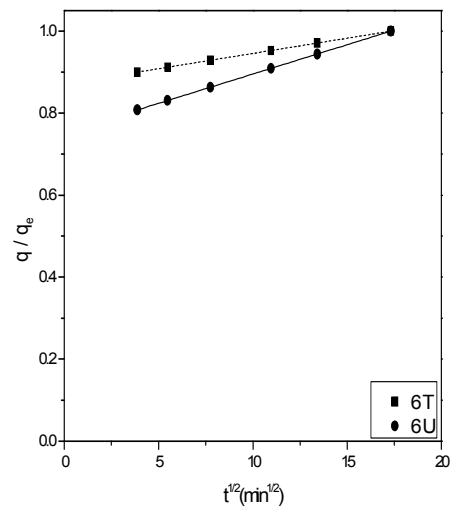
Figure 7.15. Intraparticle diffusion kinetic curves of Ce- exchange at 50 °C (fold equivalent excess: (a) 3 (b) 5 (c) 6 (d) 9).



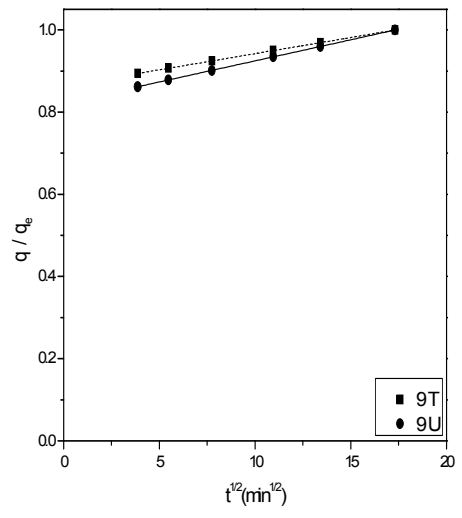
(a)



(b)



(c)



(d)

Figure 7.16. Intraparticle diffusion kinetic curves of Ce- exchange at 70 °C (fold equivalent excess: (a) 3 (b) 5 (c) 6 (d) 9).

Intraparticle diffusion model in this form give also information about the resistance other than one step intraparticle. The C value, intercept of the plot is considerably high showing that the external film and/or intraparticle resistances should be considered. The parameter is decreased with increasing valence (and hydrated radius) of counter ions. The effect of ultrasound on the C value is not evident. As a result the effect of ultrasonic method on the intraparticle becomes clear at high initial bulk solution (fold equivalent excess) and temperature. However ultrasonic method on the external film resistance is not as effective as into the particle surprisingly.

The effect of temperature on intraparticle rate constant

The activation energy and thermodynamics parameters which are important in understanding the mechanism of ion exchange were obtained by using the change in the intraparticle diffusion rate constant, k_i , with temperature (Table 7.4). The plot of rate constant versus the reciprocal temperature was given in Appendix B.

Table 7.4. The activation energy and thermodynamic paramaters for lithium, calcium and cerium exchange.

Counter ion	Fold Equiv. Exces	E_a (kJ mol ⁻¹)		ΔH^* (kJ mol ⁻¹)		ΔS^* (kJ mol ⁻¹ K ⁻¹)		ΔG^* (kJ mol ⁻¹)	
		T	U	T	U	T	U	T	U
Li ⁺	3	22	-19	19	-21	-0.23	-0.34	98	96
	6	16	6	13	4	-0.24	-0.26	96	93
	9	19	5	17	3	-0.23	-0.26	94	91
Ca ²⁺	3	-86	8	-89	5	-0.56	-0.28	102	100
	6	60	56	57	54	-0.12	-0.12	97	96
	9	53	24	50	21	-0.23	-0.11	96	94
Ce ³⁺	3	-5	24	-13	22	-0.33	-0.22	100	95
	5	53	24	50	21	-0.13	-0.21	96	94
	6	16	38	13	35	-0.25	-0.18	99	96
	9	6	9	3	7	-0.28	-0.27	98	97

The activation energy, the dependence of rate constant to temperature, from the slope of the plot was suggested that the rise in the solution temperature favour Li⁺, Ca²⁺ and Ce³⁺ ions exchange onto NaX zeolite at high fold equivalent excess. However, it is interesting to note that an increase in temperature favors a decrease in the cation content in the solid phase for Li-exchange by using ultrasonic method and Ca- and Ce-

exchanges by using traditional method with three fold equivalent excess. After that an increase in temperature favors an increase in the cation content in solid phase with an increasing fold equivalent excess for both methods. As stated by Barros et al. (2003), the ion exchange mechanism is influenced by the three dimensional framework of the NaX zeolite. It can be prevented with some effort to diffuse some ions into unfavorable sites, this unrequired effect was overcome with increasing fold equivalent excess.

The activation energies for the ion exchange were not so high to eliminate the intraparticle diffusion. Al-Ghouti (2005) stated that the lower value of activation energy than 42 kJ mol⁻¹ indicates that diffusion is dominant in the ion exchange.

The thermodynamic parameters, enthalpy of activation, ΔH^* , entropy of activation, ΔS^* , and Gibbs free energy of activation, ΔG^* , were calculated with the Eyring equation (Chapter 4, Eqn. 4.28). As seen from Table 7.4, the cation exchange reactions are the endothermic reactions due to positive values of enthalpy of activation with some exceptions.

The enthalpy of activation for Li⁺ ion exchange is lower in ultrasonic method than traditional method. This means that lithium is replaced by sodium with strong electrostatic interaction when the traditional method was used.

The values of Gibbs free energy (about 100 kJ mol⁻¹) show that the ion exchange reaction should be forced with either the ultrasonic or traditional methods. The negative value in entropy of activation also reflects no significant change in the internal structure of NaX zeolite during ion exchange process as stated by Al- Ghouti (2005). Since the ion exchange is endothermic and the contribution of the entropy is also negative value, the process is driven neither enthalpy nor entropy. This showed that the reverse reaction is spontaneous.

The early stage data could not be collected due to fast ion exchange applied in this study. For this reason the intraparticle diffusion coefficient, D , was calculated by using the following model equation given in Chp. 4.

$$\frac{q}{q_e} = 1 - \frac{6}{\pi^2} \exp\left(-\frac{\pi^2 Dt}{r^2}\right) \quad (4.12)$$

The collected data fitted with the model by decreasing the sum of square of error (SSE) values ($3 \times 10^{-4} < \text{SSE} < 840 \times 10^{-4}$). The correlation coefficient values were

changed in the range of $0.47 < R^2 < 0.98$. We can conclude that the data are not agreed with this model as well as previous model. As seen from Tables, the intraparticle diffusion coefficient for Li^+ and Ca^{2+} ion exchange was increased with decreasing counter ions concentration in both exchange methods at $70\text{ }^\circ\text{C}$, in traditional method at $50\text{ }^\circ\text{C}$. The disordered change in diffusion coefficient with counter ion concentration was observed for Ce^{3+} ion exchange. The effect of hydrated radius of the counter ions and temperature onto diffusion coefficients was not observed clearly. As a result the effect of ultrasound on the exchange rate is not evident as previous model.

Mass transfer rate constant in the external film, k_f , was calculated from the external film resistance model equation

$$\frac{d\bar{q}}{dt} = \frac{3k_f}{Kr} (q_e - \bar{q}) \quad (4.19)$$

and the Sherwood number with an assuming as a stagnant fluid or low value of Reynold number .

$$Sh = \frac{k_f r}{D} = 2 \quad (4.22)$$

The external film mass transfer coefficients were tabulated in Table 7.5 and 7.6 for $50\text{ }^\circ\text{C}$ and $70\text{ }^\circ\text{C}$, respectively. The SSE values for the external film resistance model are changed from 2×10^{-4} to 824×10^{-4} . The k_f value changed irregularly with fold equivalent excess even the experimental data were well correlated with the model ($R^2 > 0.94$). The k_f values are increased with decreasing the valence of the counter ions. The order of the k_f values is;

$$\text{Li}^+ \text{ ion exchange} > \text{Ca}^{2+} \text{ ion exchange} > \text{Ce}^{3+} \text{ ion exchange}$$

The external film mass transfer coefficients was also calculated by using dimensionless method. Stagnant fluid was considered to calculate the k_f value in the dimensionless method. However, the results were found approximately same with the external film mass transfer coefficients calculated by using external film mass transfer model for ultrasonic and traditional methods. This can be explained with the local velocity of ultrasound which is not representing the bulk fluid. The expected

enhancement in the exchange kinetics due to ultrasonic irradiation was not observed. The unexpected result of ultrasonic method can have risen from insufficient mixing depending on the immersion depth of the horn, shape and type of the beaker used as stated by Klima (2011).

Biot mass number, Bi_m , a measure of intraparticle to external film resistance,

$$Bi_m = \frac{k_f r_c}{D} \quad (4.25)$$

where the critical radius, r_c was taken as $r/3$ for spherical particle. Biot number was calculated by using the intraparticle diffusion coefficient and k_f calculated from external film transfer model (Table 7.5 and 7.6). Bi_m values ($0.1 < Bi_m < 0.7$) are not so higher than 0.1 which is the critical value to decide the controlling step in mass transfer. Therefore both intraparticle and external film diffusion are comparable for Li^+ , Ca^{2+} and Ce^{3+} ion exchange. However the external film mass transfer seems to be pronounced for multivalent cations rather than monovalent cation.

The kinetic models; reaction and diffusion show that, the chemical reaction was dominant at initial of the ion exchange and followed by a slower process till equilibrium attained. At this time, the intraparticle, besides to external film resistance were involved in the ion exchange as the rate controlling steps.

Table 7.5. Diffusion models parameters of ion exchange at 50 °C.

Counter ion	Fold Equiv. Excess	Intraparticle Diffusion										External Diffusion						Bi _m	
		k _i (meqg ⁻¹ min ^{-1/2})		C (-)		R ²		Dx10 ¹⁶ (m ² s ⁻¹)		R ²		K _f x10 ¹⁰ (m s ⁻¹)		*K _f x10 ¹⁰ (m s ⁻¹)					
		T	U	T	U	T	U	T	U	T	U	T	U	T	U	T	U	T	U
Li ⁺ r _H =3.80	3	0.005	0.030	0.82	0.76	0.9594	0.9420	1.64	0.52	0.5308	0.7754	1.20	0.70	0.9879	0.9595	1.6	0.5	0.3	0.6
	6	0.010	0.040	0.93	0.79	0.9701	0.9427	1.51	0.92	0.5798	0.8245	1.00	0.97	0.9994	0.9845	1.5	0.9	0.1	0.2
	9	0.020	0.080	0.87	0.75	0.8054	0.9906	0.83	0.59	0.8150	0.9160	1.50	1.13	0.9884	0.9826	0.8	0.6	0.3	0.3
Ca ²⁺ r _H =4.12	3	0.004	0.003	0.94	0.95	0.9038	0.9057	2.58	2.12	0.4770	0.7692	0.94	0.84	0.9993	0.9987	2.6	2.1	0.1	0.1
	6	0.003	0.006	0.96	0.94	0.7786	0.9165	2.44	2.73	0.8233	0.7315	0.89	0.99	0.9993	0.9993	2.4	2.7	0.1	0.1
	9	0.004	0.021	0.96	0.81	0.8111	0.9449	0.56	1.62	0.9855	0.7351	1.15	0.68	0.9970	0.9950	0.6	1.6	0.3	0.1
Ce ³⁺ r _H =9.0	3	0.005	0.013	0.91	0.77	0.9171	0.8660	1.86	1.10	0.7361	0.8905	0.42	0.32	0.9970	0.9924	1.8	1.1	0.1	0.1
	5	0.005	0.017	0.89	0.72	0.8403	0.9171	2.11	0.89	0.7448	0.9303	0.47	0.27	0.9952	0.9904	2.1	0.9	0.1	0.1
	6	0.005	0.007	0.91	0.88	0.8926	0.9533	2.04	1.86	0.6399	0.8030	0.46	0.47	0.9968	0.9975	2.0	1.9	0.1	0.1
	9	0.007	0.009	0.88	0.83	0.8309	0.8087	1.52	1.44	0.9459	0.9776	0.36	0.38	0.9984	0.9986	1.5	1.4	0.1	0.1

*Calculated by using dimensionless method

Table 7.6. Diffusion models parameters of ion exchange at 70 °C.

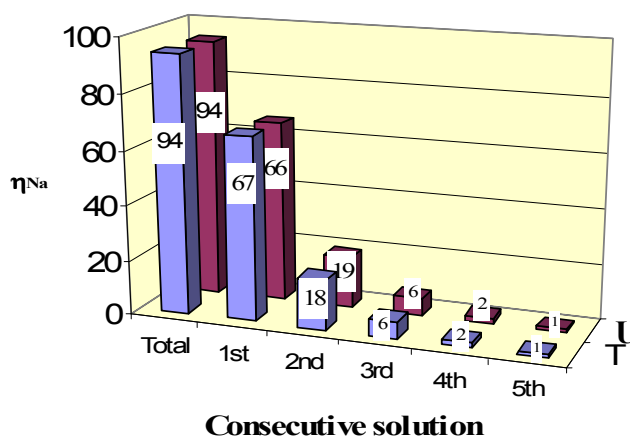
Counter ion	Fold Equiv. Excess	Intraparticle Diffusion										External Diffusion						Bi _m	
		k _i (meqg ⁻¹ min ^{-1/2})		C (-)		R ²		Dx10 ¹⁶ (m ² s ⁻¹)		R ²		K _f x10 ¹⁰ (m s ⁻¹)		R ²		*K _f x10 ¹⁰ (m s ⁻¹)			
		T	U	T	U	T	U	T	U	T	U	T	U	T	U	T	U	T	U
Li ⁺ r _H =3.80	3	0.008	0.018	0.95	0.92	0.9719	0.9538	3.02	2.53	0.8660	0.8255	1.3	1.8	0.9990	0.9993	3.0	2.5	0.2	0.3
	6	0.014	0.047	0.93	0.83	0.9215	0.9363	0.95	1.67	0.7381	0.6182	0.7	1.3	0.9969	0.9932	1.0	1.7	0.2	0.2
	9	0.035	0.085	0.85	0.78	0.9719	0.9425	3.74	0.70	0.6825	0.7604	2.6	1.2	0.9998	0.9923	3.7	0.7	0.1	0.3
Ca ²⁺ r _H =4.12	3	0.002	0.004	0.97	0.96	0.8001	0.9558	3.72	1.54	0.6999	0.5772	1.2	1.2	0.9998	0.9992	3.7	1.5	0.1	0.3
	6	0.011	0.019	0.89	0.82	0.8414	0.9545	1.09	0.69	0.9576	0.7300	0.3	0.3	0.9980	0.9881	1.1	0.7	0.1	0.2
	9	0.015	0.030	0.86	0.75	0.9862	0.9518	0.89	0.70	0.7688	0.8622	0.7	0.5	0.9953	0.9889	0.9	0.7	0.1	0.1
Ce ³⁺ r _H =9.0	3	0.004	0.022	0.91	0.64	0.9199	0.9590	2.24	0.56	0.8314	0.9326	0.4	0.2	0.9989	0.9783	2.2	0.6	0.1	0.1
	5	0.018	0.037	0.67	0.54	0.9656	0.9772	0.41	0.64	0.7829	0.9565	0.1	0.2	0.9445	0.9875	0.4	0.6	0.1	0.1
	6	0.007	0.016	0.87	0.75	0.7707	0.9030	1.91	1.08	0.8661	0.9361	0.3	0.3	0.9955	0.9939	1.9	1.1	0.1	0.1
	9	0.008	0.011	0.86	0.82	0.9602	0.9211	1.82	1.36	0.6662	0.6227	0.4	0.4	0.9955	0.9894	1.8	1.4	0.1	0.1

*Calculated by using dimensionless method.

7.1.2. Consecutive Studies

Equilibrium experiments were conducted by refreshing the counter cation solution. 5 consecutive solutions were used to obtain fully exchanged Li-, Ca- and Ce-zeolites. The experiential conditions (9 fold equivalent excess Li^+ and Ca^{2+} ion solutions and 5 fold equivalent excess Ce^{3+} ion solutions at $70\text{ }^\circ\text{C}$) in which maximum exchange obtained from kinetic studies were used in equilibrium studies.

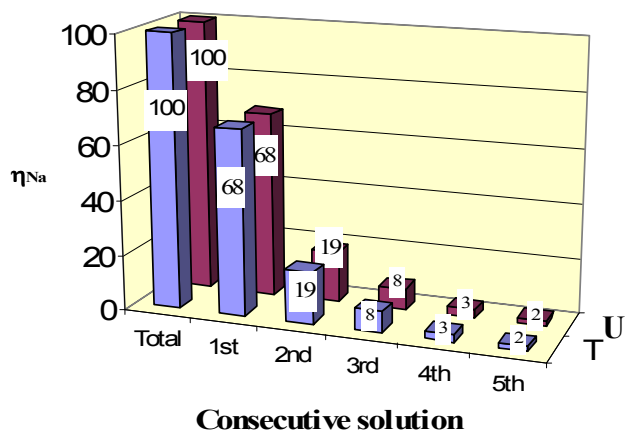
Figure 7.17 shows the change in the exchange percent of sodium ion with number of consecutive solution and the method used. The highest exchange of Na^+ ions into the 1st consecutive solution was observed. On the other hand almost no exchange in the 5th consecutive solution was obtained. It was found that 100 % and 94 % was obtained for Li^+ and Ca^{2+} ions exchange by using the both methods. However the effect of the method is evident in Ce^{3+} ion exchange; 62 % from traditional method and 73 % from ultrasonic method. As a conclusion, the negative effect of hydrated radius on the exchange is not overcome in consecutive study. Hence fully exchanged Ca^{2+} and Ce^{3+} ions can not be obtained.



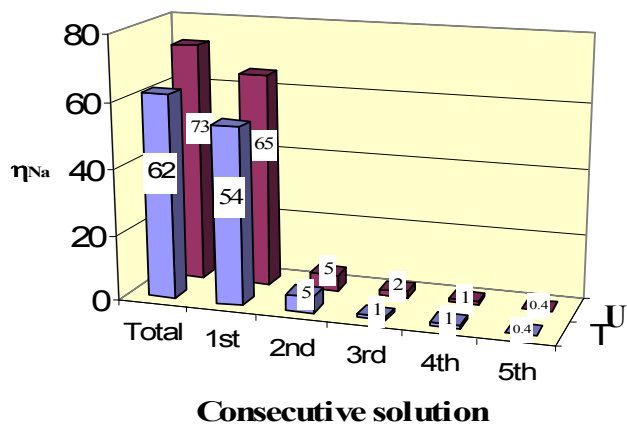
(a)

Figure 7.17. Ion exchange with consecutive cation solution of (a) Li^+ (b) Ca^{2+} (c) Ce^{3+} ions in traditional (T) and ultrasonic method (U).

(cont. on next page)



(b)



(c)

Figure 7.17. (cont.).

7.2. Characterization Studies

The characterization studies were applied to granule and ion exchanged form of NaX zeolite. The structural and textural properties of the zeolites in powder and granule forms were investigated by using volumetric nitrogen adsorption system, X-Ray diffractometer (XRD), scanning electron microscope (SEM), Fourier transform infrared spectroscopy (FT-IR), Zwick/Roell microhardness test device and sieve shaker.

7.2.1. Zeolite granules

Granulation densifies the material and makes them homogeneous in terms of size, shape and facilitates manipulation. In granulation, zeolite powder with the extent of 10 - 20 wt % were mixed with clay mineral from kaolin, smectite and sepiolite groups. Sepiolite (S) and montmorillonite (M) were used to test the granulation of NaX zeolite powder. The characterization studies were applied to powder of NaX zeolite and its granule forms (NaX, NaX-S, NaX-M) in order to investigate the effect of binders and the methods used.

Nitrogen adsorption isotherms (at 77 K) from volumetric adsorption system are shown in Figure 7.18. The zeolites were degassed for 24 h under vacuum better than 10^{-5} mbar at 350 °C. According to the IUPAC classification, the isotherms of montmorillonite and sepiolite are of Type II whereas that of NaX in powder and granule form are of Type I as illustrated in Appendix C, Figure C1 and C2.

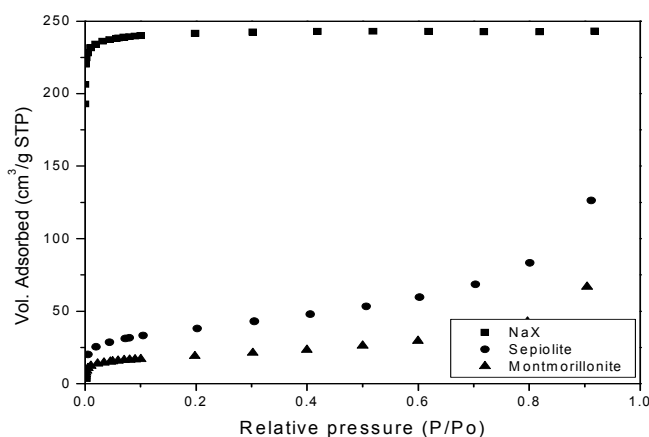


Figure 7.18. N₂ adsorption isotherms of NaX zeolite, sepiolite and montmorillonite.

Type I and Type II isotherms are typical isotherms for microporous and mesoporous material, respectively (Rouquerol et al., 1999). Textural properties such as specific surface area, external surface area and micropore volume of minerals in powder and granule forms are given in Table 7.7 and 7.8, respectively.

Table 7.7. N₂-adsorption isotherms at 77 K for NaX zeolite and clay minerals* .

Textural properties	NaX	Sepiolite (S)	Montmorillonite (M)
Specific surface area (m ² g ⁻¹)	1058 ^L	132 ^B	65 ^B
External surface area (m ² g ⁻¹)	42	114	47

*Specific Surface area from B.E.T (B) and Langmuir(L) methods, external surfacace area from t-plot method.

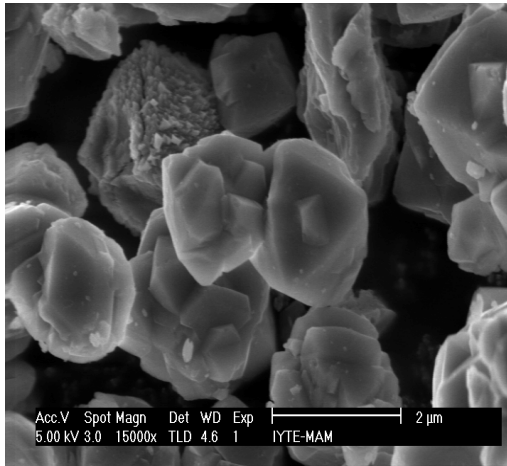
As seen from the Table 7.8, granulation is worsen the textural properties of zeolites. This can be result from heat treatment applied in both procedure (A and B). However, the effectiveness of the procedures on the textural properties was not evident.

Table 7.8. The textural properties of the zeolite granules* .

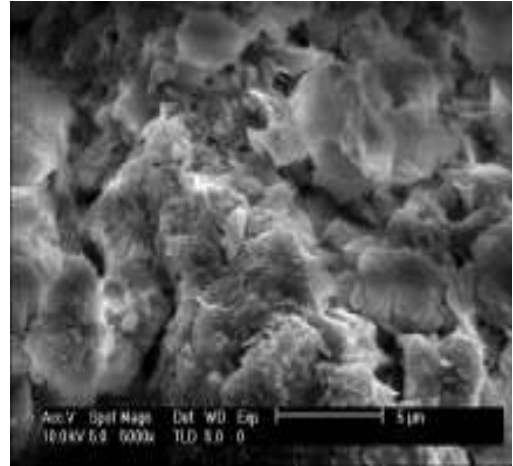
Textural properties *		Zeolite Codes				
		NaX	NaX-S (10%)	NaX-S (20%)	NaX-M (10%)	NaX-M (20%)
Specific surface area (m ² g ⁻¹)	Procedure A	1195	1026	786	1086	1097
		8.9	43	34	29	47
		0.42	0.34	0.26	0.37	0.37
External surface area (m ² g ⁻¹)	Procedure B	1324	683	1151	998	691
		8	25	30	24	30
		0.47	0.23	0.39	0.34	0.23
Max.pore volume (cm ³ g ⁻¹)						

*Specific surface area from Langmuir method, external surfacace area from t-plot method, max. pore volume from Horvath-Kawazoe method

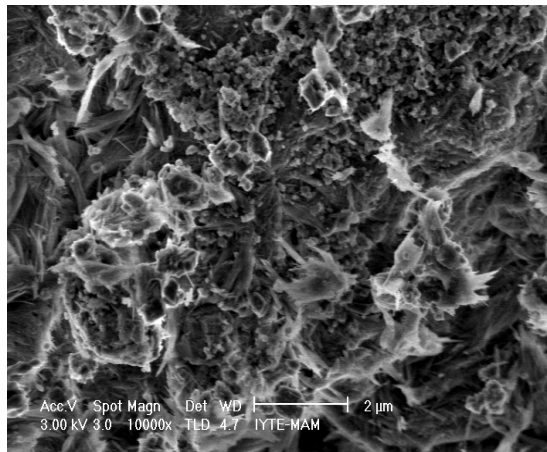
The **SEM** images of the zeolites in powder and granule form are given in Figure 7.19 and 7.20 respectively. As shown from Figure 7.20 montmorillonite and sepiolite crystals stuck on the zeolite crystals.



(a)

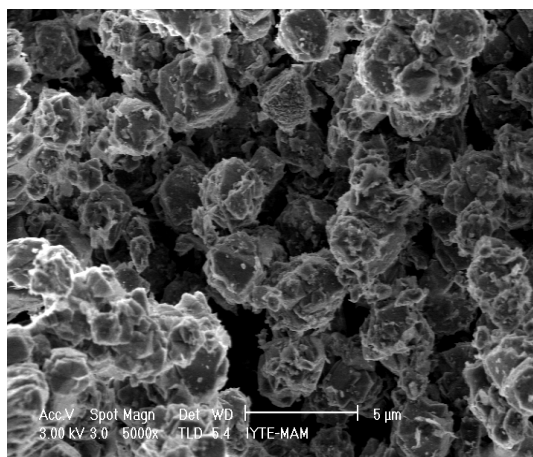


(b)

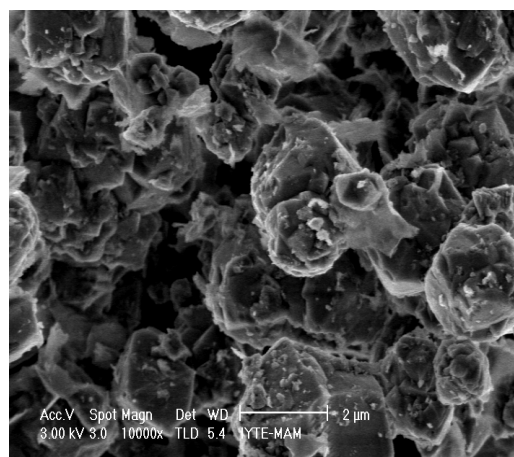


(c)

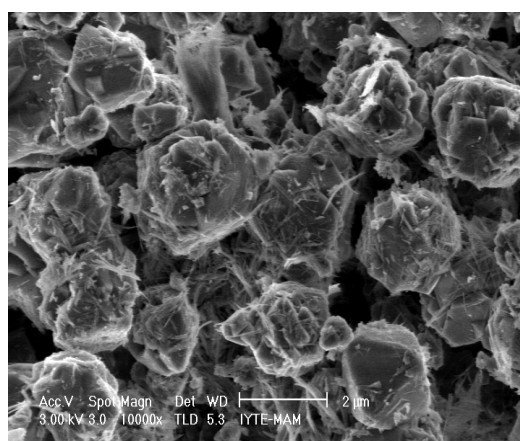
Figure 7.19. SEM images of (a) NaX zeolite (b) Montmorillonite (c) Sepiolite.



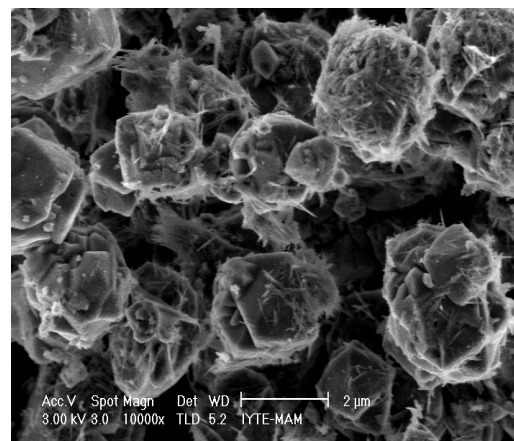
(a)



(b)



(c)



(d)

Figure 7.20. SEM images of (a) NaX-M (10%) (b) NaX-M (20%) (c) NaX-S (10%) (d) NaX-S (20%).

The effect of montmorillonite and sepiolite on the crystalline structure of NaX zeolite by using *X-ray diffractogram* were seen in Figure 7.21 and 7.22, respectively. NaX is highly crystalline material and its granule form has still crsytalline even if exposing heat treatment at 600 °C.

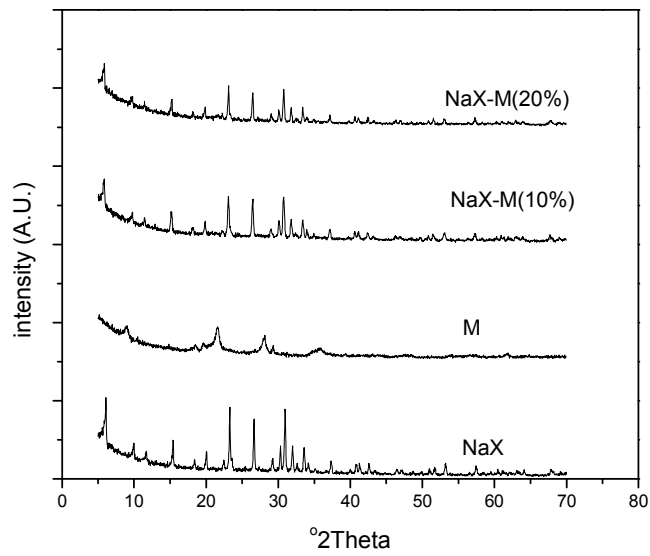


Figure 7.21. X-ray diffractogram of the NaX zeolite, Montmorillonite (M) and granulated form with montmorillonite (NaX-M).

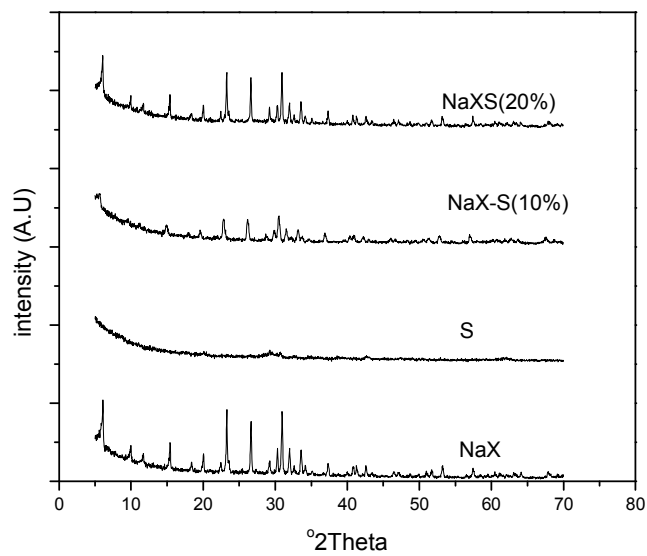


Figure 7.22. X-ray diffractogram of NaX zeolite, Sepiolite (S) and granulated form with sepiolite (NaX-S).

FT-IR spectroscopy was used to measure changes in the character or quantity of a particular bond, symmetric stretching band at 754 cm^{-1} , the double-ring vibration band at 566 cm^{-1} , characteristic of faujasite zeolites as stated by Zhan et al. (2002) as seen from Figure 7.23.

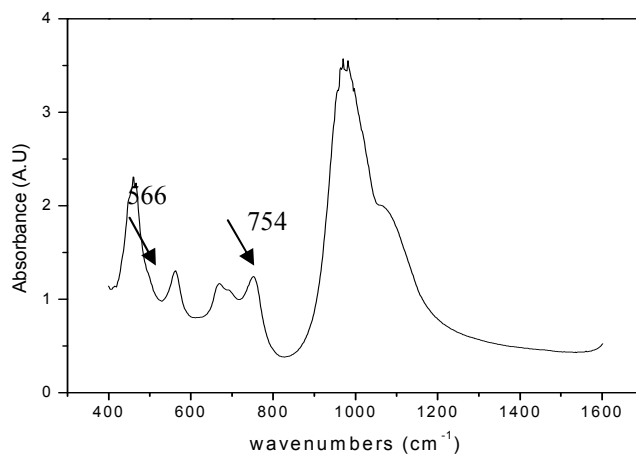


Figure 7.23. FT-IR spectra of NaX zeolite.

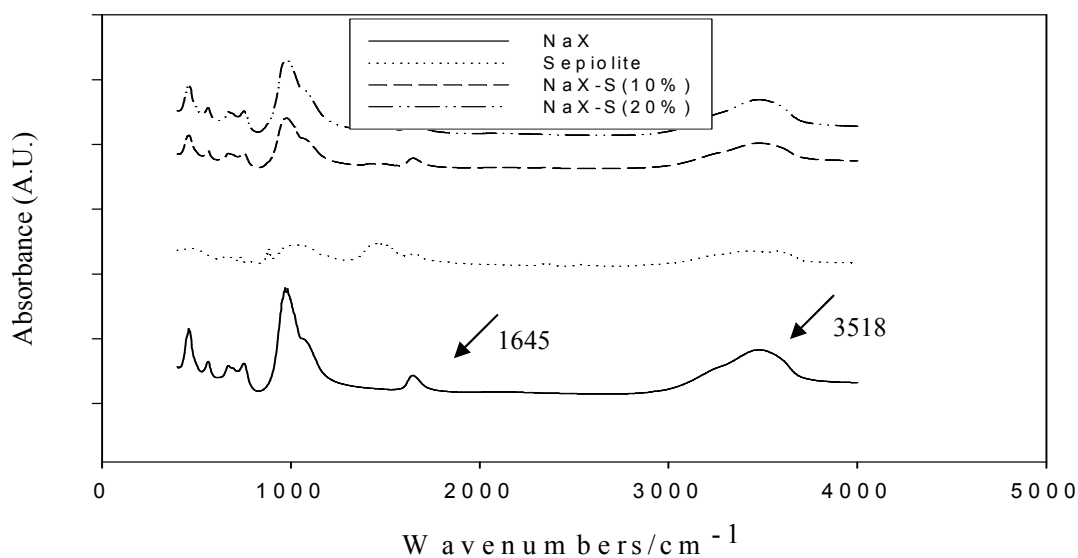


Figure 7.24. FT-IR spectra of the zeolites and Sepiolite.

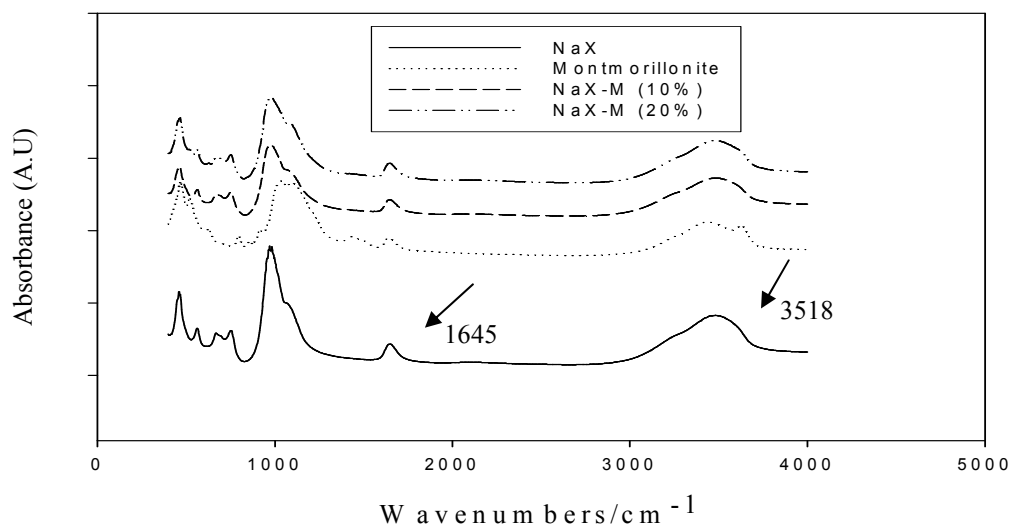


Figure 7.25. FT-IR spectra of the NaX zeolites and Montmorillonite.

The band at 1645 cm^{-1} is the characteristic of the bending mode in the water molecule. The water bending frequency is absent when the zeolite is fully activated. As seen from the Figure 7.24 and 7.25, frequency of water bend decreased with the granulation process as stated by Breck (1974). At room temperature, FT-IR spectra of the NaX zeolite showed a broad band of water sorption over the hydroxyl stretching region. However, upon granulation of NaX zeolite with montmorillonite and sepiolite, surface water decreased after heating at $600\text{ }^{\circ}\text{C}$ was stated by Jasra et al. (2003).

Fourier transform infrared spectroscopy showed a decrease in acidity upon granulation of zeolite as observed from the reduction in the intensity of the peaks corresponding to acidic hydroxyl groups (3518 cm^{-1}) which are on the surface of the sodalite cages. Decreasing in acidity of zeolite occurs with migration of exchangeable clay cations such as Na^+ , Mg^{2+} or Ca^{2+} ions to the zeolite pores during replacement with acidic H^+ ions of the zeolite as given in literature (Jasra et al., 2003). It can be said that FT-IR studies confirmed solid state cation exchange during zeolite granulation process as well as XRD. Hence the surface of the sodalite cages zeolites contains hydroxyl groups

The hardness test was provided measuring the abrasion of the zeolites and clay minerals (sepiolite and montmorillonite). The unit of hardness test is known as the Vickers Pyramid Number (HV) and determined as the following equation;

$$HV = \frac{\text{Indenter force (kg)}}{\text{Surface area of the indent (mm}^2\text{)}} \quad (7.4)$$

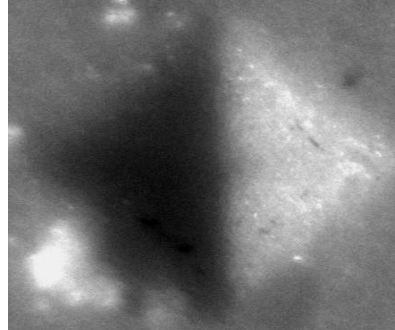


Figure 7.26. Indentation of the NaX pellets.

The Figure 7.26 shows the shape of the Vickers indenter which is square and the two diagonals have similar lengths. NaX pellet showed the highest resistance to abrasion and montmorillonite was seen more suitable in order to use as binder in granulation comparing to the sepiolite (Table 7.9).

Table 7.9. Vickers hardness numbers of the zeolites.

Zeolite Codes	HV (kg mm ⁻²)
NaX	27
Montmorillonite (M)	20
Sepiolite (S)	20
NaX-S (10 %)	14
NaX-S (20 %)	18
NaX-M (20 %)	21

Attrition test was carried out to measure the resistance of a granular zeolites to wear. Because a fluid flow may cause adjacent particles to contact and can abrade each other. High particle attrition contributes to product contamination, particle loss, plugging of equipment. The problem of particle attrition is especially severe with high porosity particles such as molecular sieves. Due to the ceramic nature of material, the surface is highly abrasive and subject to attrition.

Table 7.10. Losses (%) on attrition for NaX zeolite, clay minerals and pellet forms.

Zeolite Codes		loss % at 20 amplitude	loss % at 50 amplitude
NaX	Procedure (B)	0.08	0.81
NaX-M (10 %)		0.11	10.0
NaX-M (20 %)		0.08	2.72
NaX-S (10 %)		2.22	3.29
NaX-S (20 %)		1.93	1.77
NaX	Procedure (A)	77.2	----
NaX-M (10 %)		2.32	4.18
NaX-M (20 %)		1.20	2.12
NaX-S (10 %)		11.5	26.4
NaX-S (20 %)		5.33	19.1

The highest strength was obtained with NaX granule with procedure B (Table 7.10). Using montmorillonite provided higher resistance to abrasion than sepiolite as a binder. Loss on attrition decreased with weight percentage of binders used in granulation increased.

7.2.2. Ion Exchanged Zeolite

The characterization studies were done to observe the effect of ion exchange process on thermal and textural properties of the zeolites.

Thermal Gravimetric Analysis (TGA)

The zeolite stored over a saturated ammonium chloride solution in a desiccator to keep water content constant was heated up to 1000 °C (Figure 7.27). The total weight loss below is 23.7 %.

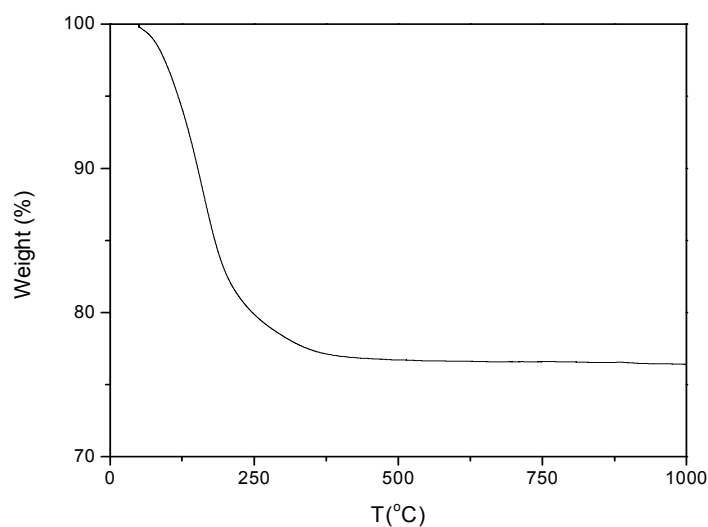


Figure 7.27. Thermogravimetry curve for NaX

As seen from the thermal gravimetric analyze (TGA) curve, the maximum weight loss due to desorbing free mobile water in the supercages was occurred up to 350 °C. Above 350 °C the water is desorbed from the hydration complexes of the cations tightly bonded to framework oxygens in the small pores of the zeolites as stated by Akbar et al. (2007).

The zeolites obtained after consecutive exchange

Textural properties of zeolites were determined by using volumetric adsorption system. Prior to N₂ adsorption, all zeolites were degassed for 24 h under vacuum better than 10⁻⁵ mbar at 350 °C. Nitrogen adsorption isotherms of the zeolites are shown on Figure 7.28. The zeolites According to the IUPAC classification, N₂ adsorption isotherms of the original (sodium), lithium and cerium rich form of the zeolites are of Type I. However, Nitrogen adsorption isotherm of calcium rich form (CaNaX) is of Type IV. The sudden jump and hysteresis at middle relative pressure on the isotherm is a result of capillary condensation in the mesopores.

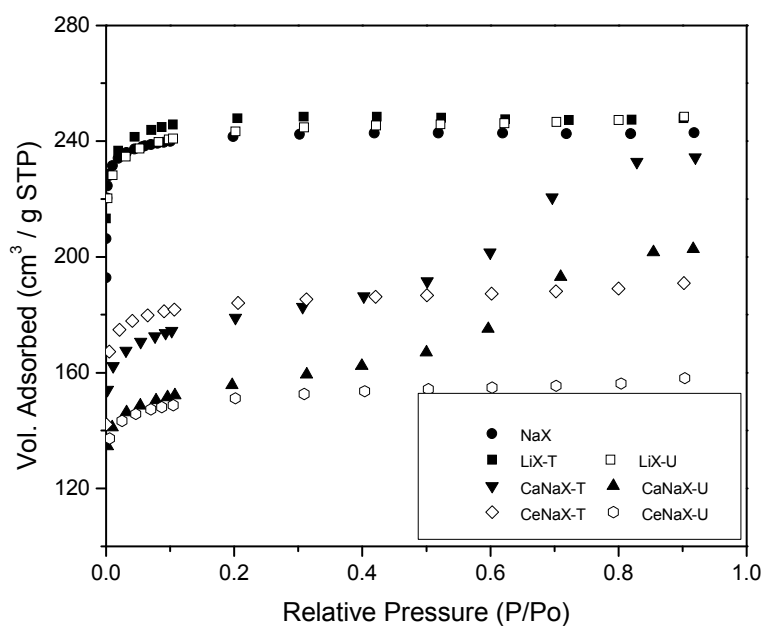


Figure 7.28. Nitrogen adsorption isotherms on NaX and exchanged NaX zeolite at 77 K.

The LiX and CeNaX zeolites with microporous structure have the highest and the lowest adsorption among the zeolites, respectively. Introduction of calcium to the structure (CaNaX-U) made the zeolite mesoporous. The isotherm data obtained were evaluated for the textural properties of the zeolites and tabulated in Table 7.11.

Table 7.11. Textural properties of the zeolites from consecutive study.

Zeolite Codes	Na- exchange (%)	Area ^L (m ² g ⁻¹)	V _{mic} (cm ³ g ⁻¹)	D _{Median} (Å)	cm ³ N ₂ /sc
NaX	---	1058	0.37	5.67	518
LiX-T	100	1087	0.38	6.57	485
LiX-U	100	1070	0.37	7.05	472
CaNaX-T	94	795	0.27	6.92	373
CaNaX-U	94	691	0.24	7.58	331
CeNaX-T	62	809	0.28	7.29	426
CeNaX-U	73	666	0.23	8.28	354

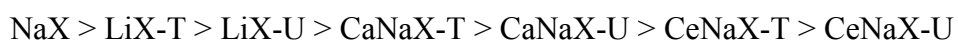
Å^L: Surface area from Langmuir method; V_{mic}: max. pore volume from Horvath-Kawazoe Method; Sc: supercage

The order of ionic radius of cations:

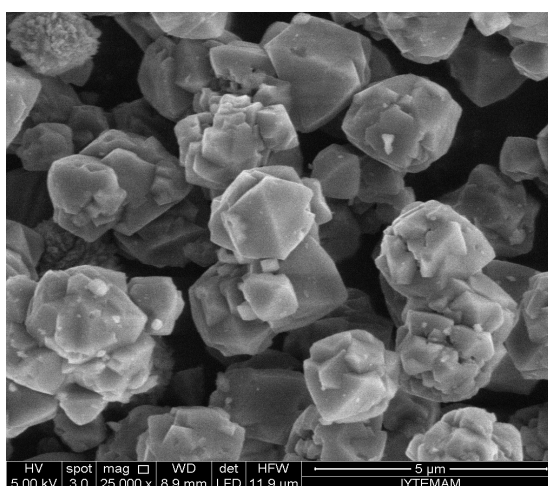
$$r_{\text{Li}^+} (0.69 \text{ \AA}) < r_{\text{Na}^+} (0.95 \text{ \AA}) < r_{\text{Ca}^{2+}} (0.99 \text{ \AA}) < r_{\text{Ce}^{3+}} (1.01 \text{ \AA})$$

The replacement of one Li⁺ ion with one Na⁺ ion for charge balancing increased the surface area of zeolite due to the ionic radius of cations. When the monovalent

sodium cations are exchanged with divalent and trivalent cations, the specific surface area decreased due to decreasing the number of cations present in the supercage (Peter et al., 2010). Thus, based on the size of these cations, the accessible pore volume of the supercage might also change. More available volume was obtained with traditional cation exchange and nitrogen capacity (at 77K) per supercage of gram zeolite was found in the order of;



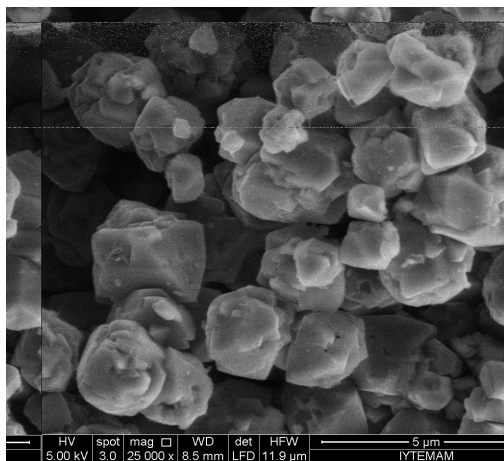
The micrographs of the surface obtained from scanning electron microscope show that the crystal size (2 μm) of NaX zeolite did not change with ultrasonic source or the methods used in Li^+ , Ca^{2+} or Ce^{3+} ion exchange (Figure 7.29).



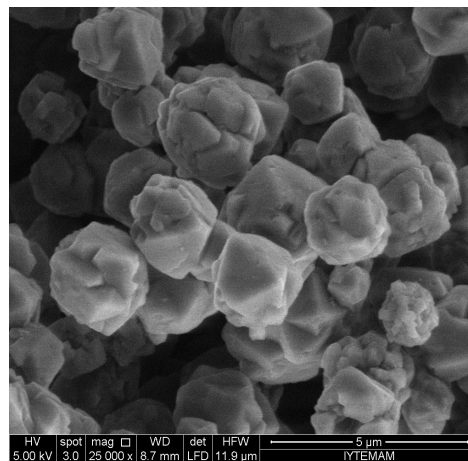
(a)

Figure 7.29. SEM images of zeolites: (a) NaX (b) LiX-T (c) LiX-U (d) CaNaX-T (e) CaNaX-U (f) CeNaX-T (g) CeNaX-U

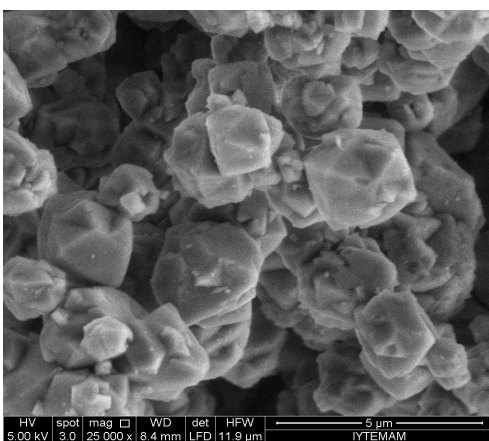
(cont. on next page)



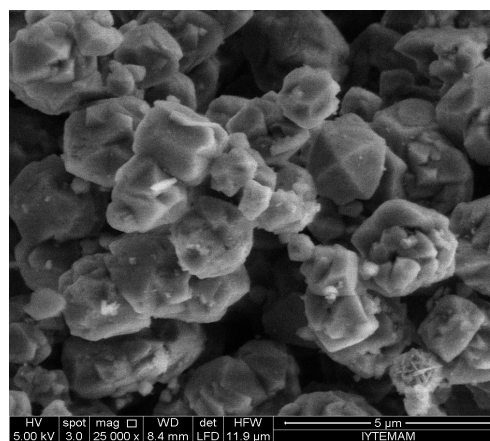
(b)



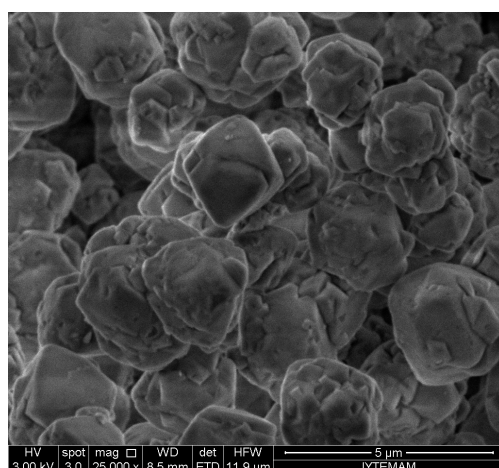
(c)



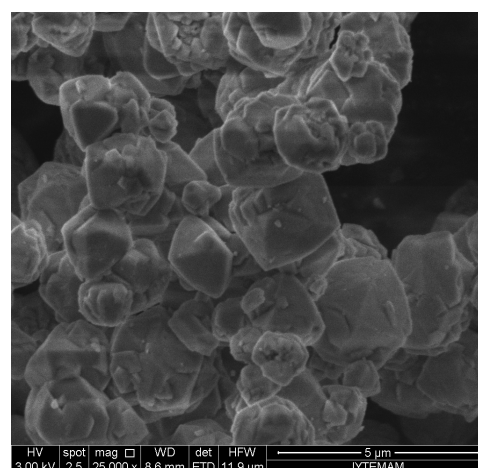
(d)



(e)



(f)



(g)

Figure 7.29. (cont.).

Figure 7.30 shows the X-ray diffractogram of the zeolites from consecutive study. The cation exchange resulted in decrease in the peak intensity as mentioned in the literature (Jasra et al., 2003; Buhl et al., 2003). As seen from the Figure 7.30, the NaX zeolite has the highest peak and highly crystalline material but its peak intensity reduced with lithium, calcium and cerium exchange process. This means that X-ray diffraction studies of the zeolites in powders confirm migration of cations to the zeolite extraframework sites.

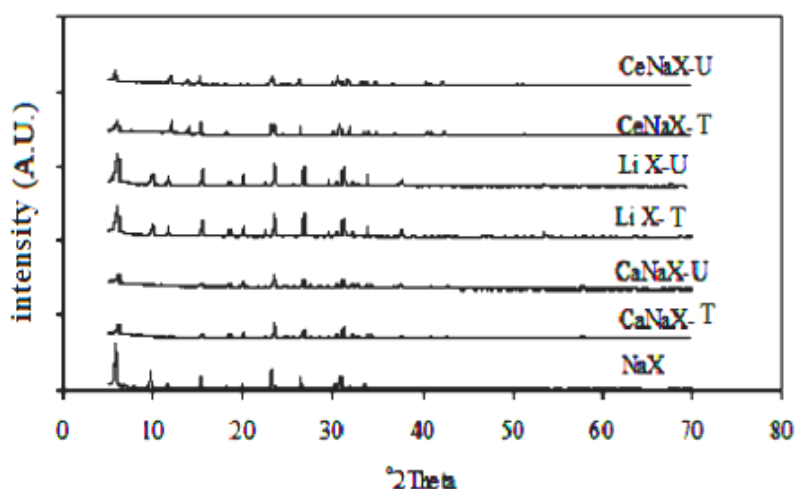


Figure 7.30. X-ray diffraction patterns of zeolites.

The zeolites obtained depending on ultrasonic source

Figure 7.31 shows the effect of the ultrasonic source on nitrogen adsorption at 77 K was examined on Li^+ , Ca^{2+} and Ce^{3+} ions exchanged zeolites, respectively. The increase in power applied in probe has negative effect on adsorption. Formation of mesopores with introduction of calcium is still observed whatever method used in Ca^{2+} ion exchange. The textural properties of the zeolites were given in Table 7.12.

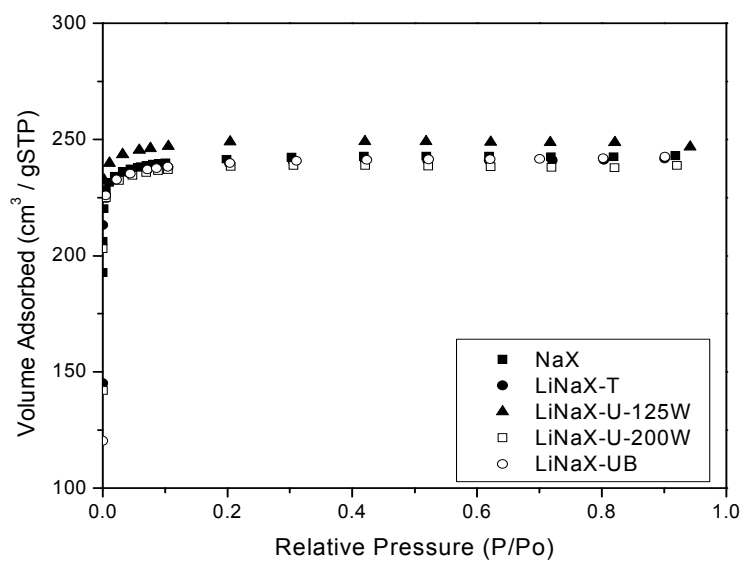
Table 7.12. Textural properties of Li⁺, Ca²⁺ and Ce³⁺ ions exchanged zeolite.

Counter ions	Physical properties*	U-125W	U-200W	UB	T
Li ⁺	Specific surface area (m ² g ⁻¹)	1086	1043	1051	1049
	Max. pore volume (cm ³ g ⁻¹)	0.38	0.37	0.37	0.37
	Median pore diameter (Å)	8.12	6.52	6.50	6.52
Ca ²⁺	Specific surface area (m ² g ⁻¹)	867	836	960	986
	Max. pore volume (cm ³ g ⁻¹)	0.30	0.29	0.33	0.34
	Median pore diameter (Å)	8.07	7.30	6.54	6.84
Ce ³⁺	Specific surface area (m ² g ⁻¹)	888	851	908	881
	Max. pore volume (cm ³ g ⁻¹)	0.31	0.30	0.32	0.31
	Median pore diameter (Å)	6.62	7.37	6.56	7.64

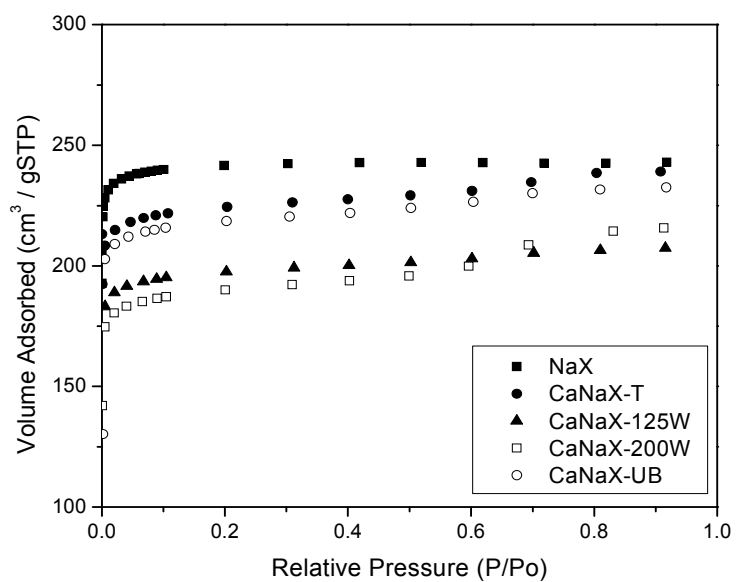
*Specific surface area from Langmuir method, max. pore volume and median pore diameter from Horvath-Kawazoe method

In ultrasonic probe method, the power applied has negative effect on zeolite surface area of the zeolites. Traditional and ultrasonic bath method give the similar results. The maximum surface area was obtained in Li⁺ ion exchange by ultrasonic probe method but ultrasonic bath method or traditional method in Ca²⁺ and Ce³⁺ ions exchange.

Surface area of Ca²⁺ and Ce³⁺ exchanged zeolites decreased comparing to the NaX zeolite. Ca²⁺ and Ce³⁺ ions are divalent and trivalent ions, respectively, reduces the number of charge compensating cations and thereby reducing the adsorption amount for nitrogen. Compared to Na⁺ ion, these counter ions will take up different site locations in NaX which cause changes in adsorption characteristics. Maximum pore volume decreased with increasing valence (and ionic radius) of counter ions. The median pore diameter increased for both counter ions when it is compared with the median pore diameter of NaX zeolite.



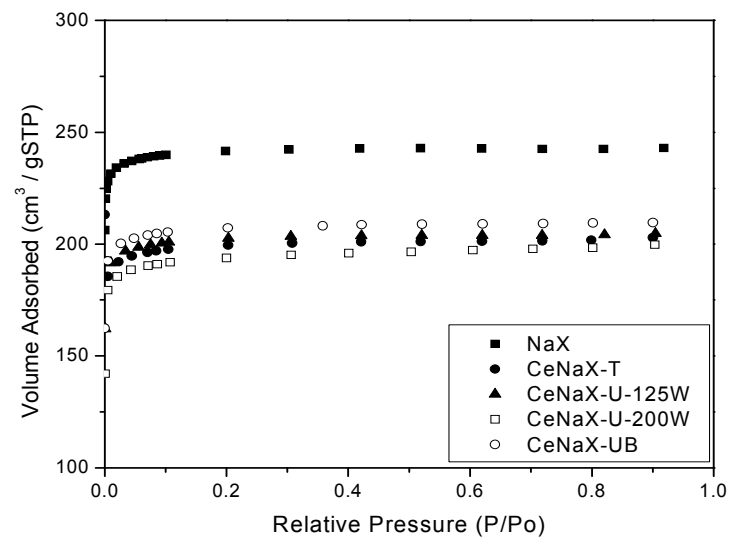
(a)



(b)

Figure 7.31. Nitrogen adsorption isotherm on (a) Li^+ (b) Ca^{2+} (c) Ce^{3+} ion exchanged zeolites.

(cont.on next page)



(c)

Figure 7.31. (cont.)

7.3. Adsorption of N₂, CO₂ and CH₄ on Zeolites by Zero Length Column Technique

CO₂, N₂ and CH₄ adsorption at 30 °C, 60 °C and 90 °C were studied by using Zero length column (ZLC) technique. This is a powerful technique for diffusivity measurement of pure gases on porous solids.

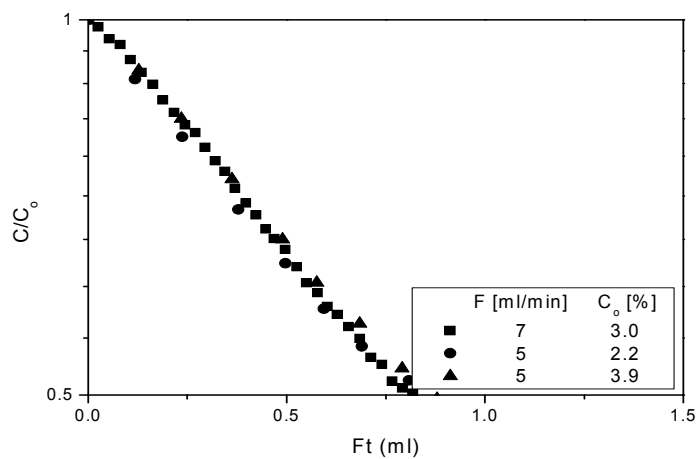
The length of the ZLC was very short and thin layer of adsorbent having 2 μm crystal size between two porous sintered discs was used which provides well mixed cell. Thus it minimizes the external resistance to heat and mass transfer. The use of individual crystals automatically eliminates macropore diffusion effects. The heat transfer effect can be eliminated and the operation is assumed isothermal.

Determination of Dead Volume and Linearity of the Response Curves

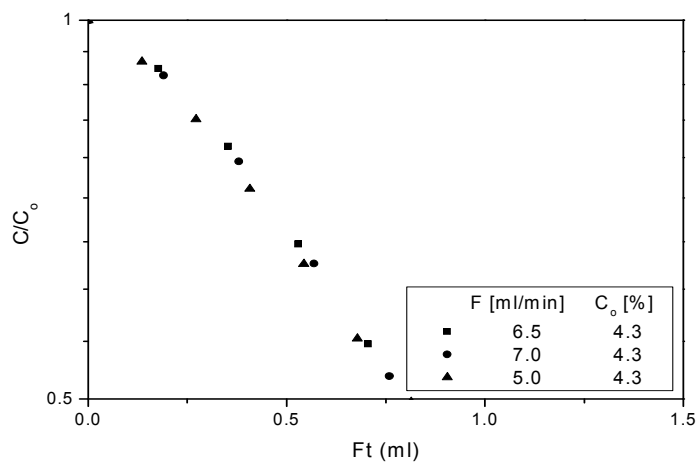
The dead volume represents the sum of the volume of the cell and the volume of the piping between the valve and the detector in the ZLC system. The determination of the dead volume, V_f , is important when the adsorbed species have poor interaction with adsorbent. The response curves for N₂, CH₄ and CO₂ gases into blank ZLC system are shown in Figure 7.32. The response curves ((C/C₀) vs.(Ft)) were independent of flow rate and adsorbate concentration, C₀. The dead volume calculated from the slope of the response curves by using

$$\frac{c}{c_0} = \exp\left(-\frac{Ft}{V_f}\right) \quad (7.5)$$

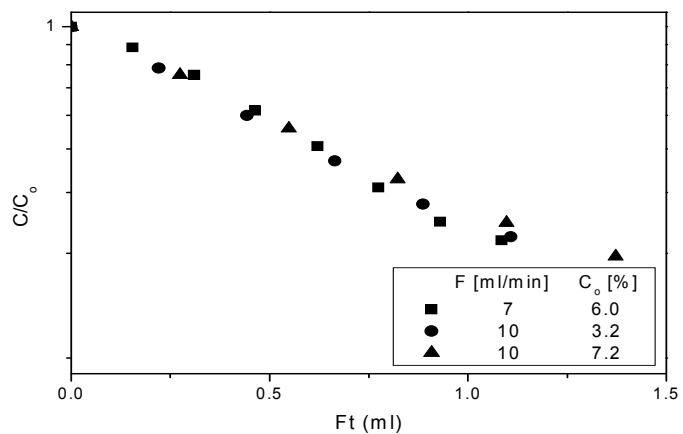
as about 1.04 ml.



(a)



(b)



(c)

Figure 7.32. ZLC blank response curves for (a) CH₄-He (b) N₂-He (c) CO₂-He.

Investigation of Controlling Step in ZLC: the kinetic or equilibrium

The flow rate is important parameter to decide the controlling step of mass transfer in ZLC: the kinetic or equilibrium control. The response curves measured at different flow rates are simple experimental test to confirm the equilibrium or kinetic control (Loos et al., 2000; Iliyas et al., 2008). As seen from the Figure 7.34, response curves were overlapped for flow rate range of 10.5-19.5 ml min⁻¹ but deviates at flow rate of 37.6 ml min⁻¹. This can be explained with the effect of purge flow rate on the time constant ratio, L . Time constant ratio, L , shows the relation between the flow rate and the controlling steps.

$$L = \frac{1}{3} \frac{\text{purge flow rate}}{\text{crystals volume}} \frac{r^2}{KD_c} = \frac{\left(\frac{r^2}{D_c}\right)}{\left(\frac{3KV_s}{F}\right)} \quad (5.16)$$

The controlling step can be decided by using the time constant ratio, L , as stated by Zaman (2004). Mass transfer in ZLC is controlled by

- equilibrium if $L < 0.5$,
- diffusion if $L \geq 5$.

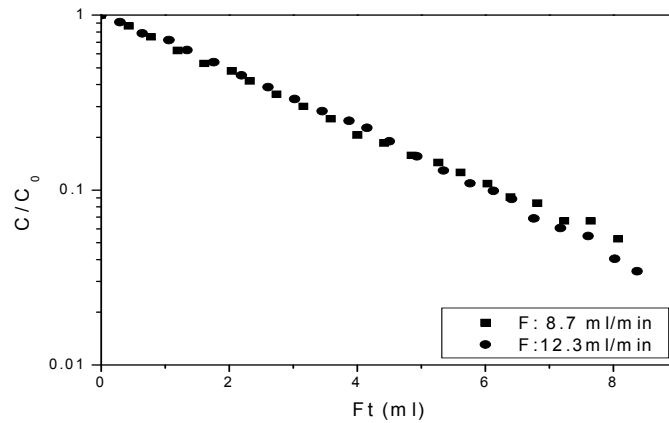


Figure 7.33. ZLC response curves for CH₄-NaX (C₀=3.3%).

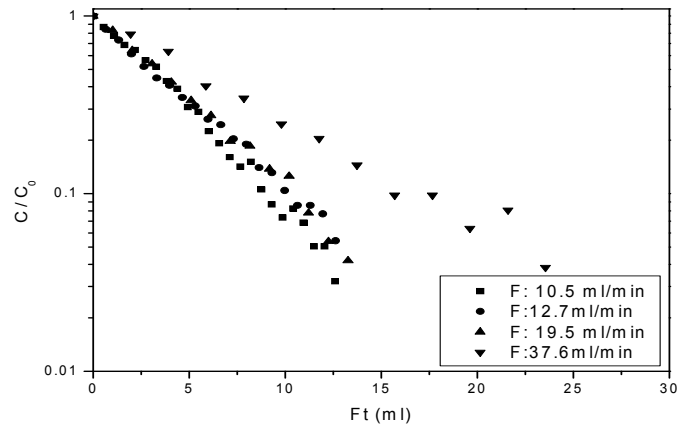


Figure 7.34. ZLC response curves for CO₂-NaX (C₀=3.2%).

According to the Figure 7.34, mass transfer is controlled by diffusion when the flow rate is used higher than 37.6 ml min⁻¹. In this study we decided to use the late stage of response curve (special case II) with Helium (purge gas) flow rate of 70 ml min⁻¹ to provide the conditions for the desorption process to be controlled by kinetics. The solution for the $C/C_0 < 0.3$ were used as the following equation.

$$\frac{C}{C_0} = \left(\frac{r^2}{L^2 \pi D_c t} \right)^{1/2} - \frac{1}{L} \quad (5.19)$$

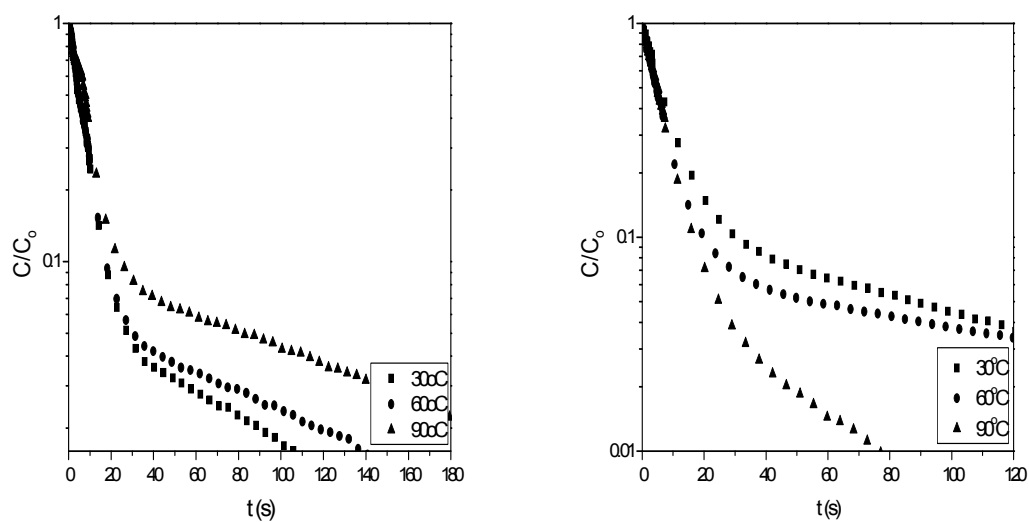
Diffusion coefficients, D_c , and L parameters were determined from the slope and intercept of the response curves (C/C_0 vs t), respectively. The data fitted with the model and the parameters were obtained by decreasing sum of square errors defined as in Equation 7.6;

$$SSE = \sum (q_{\text{exp.}} - q_{\text{calc.}})^2 \quad (7.6)$$

N₂, CH₄ and CO₂ Adsorption on Zeolites

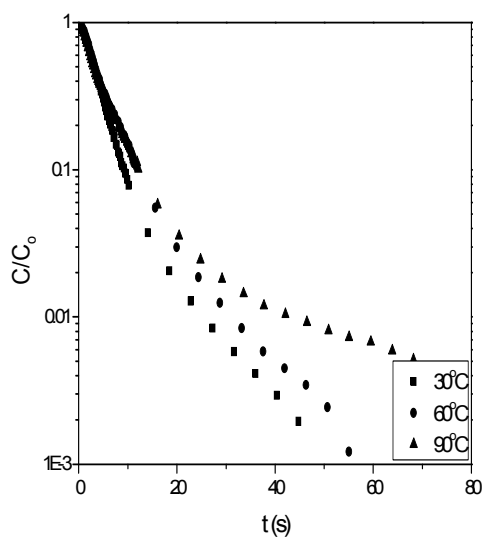
Adsorbents (LiX-U, CaNaX-U, CeNaX-U) used in the ZLC experiments are the zeolites from consecutive ion exchange study with ultrasonic method. Characterizations of the adsorbents are given in Chapter 7.2. The response curves of the gas adsorption on

the adsorbents (Figure 7.35 - 7.38) were fitted with equation 5.19 (Appendix D) and the parameters obtained were presented in Table 7.13. The experimental data were well correlated with the model ($R^2 > 0.98$). The SSE values are changed from 1×10^{-4} to 23×10^{-4} .



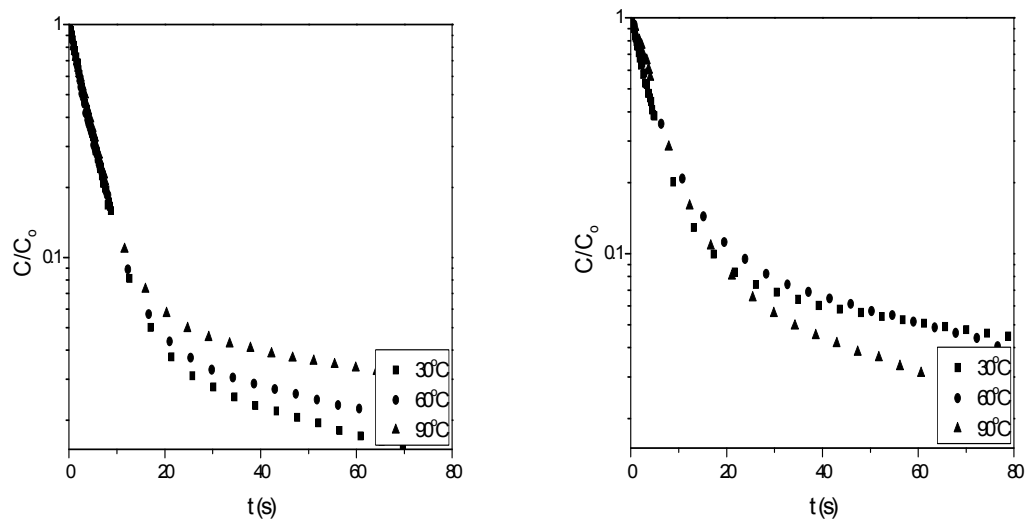
(a)

(b)



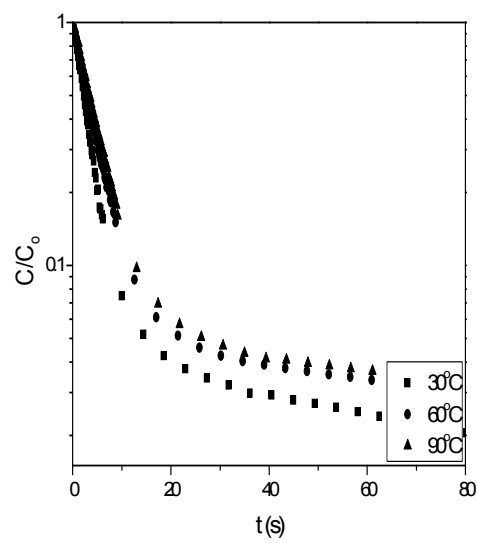
(c)

Figure 7.35. ZLC response curves of NaX for (a) N_2 (b) CO_2 (c) CH_4



(a)

(b)



(c)

Figure 7.36. ZLC response curves of LiX-U for (a) N₂ (b) CO₂ (c) CH₄

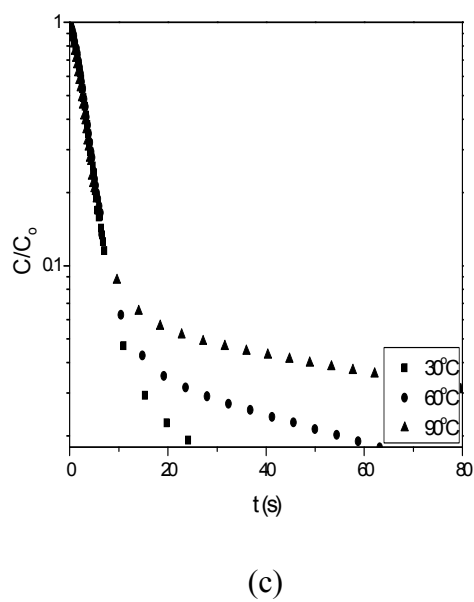
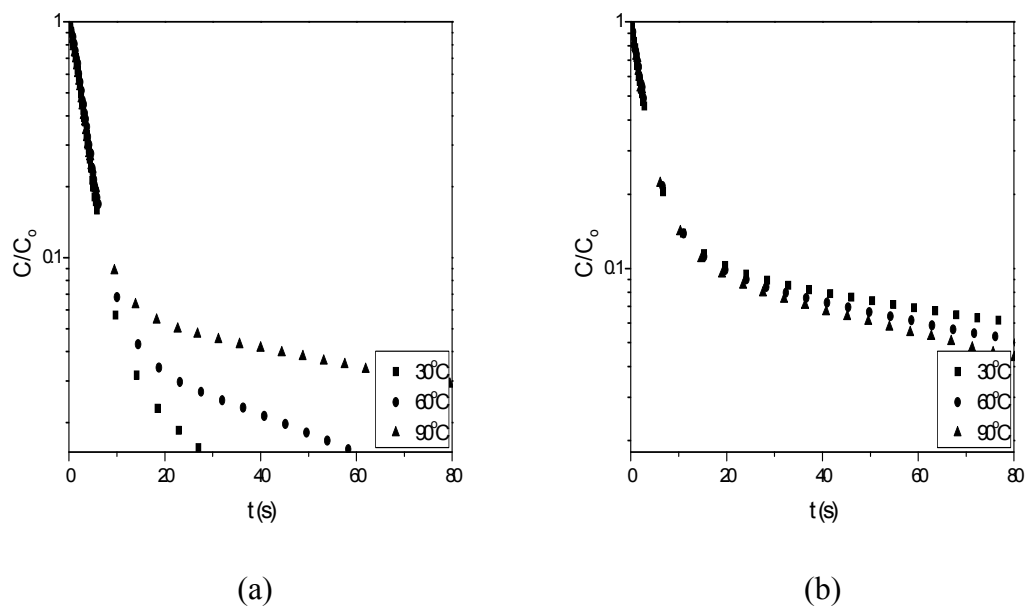


Figure 7.37. ZLC response curves of CaNaX-U for (a) N_2 (b) CO_2 (c) CH_4

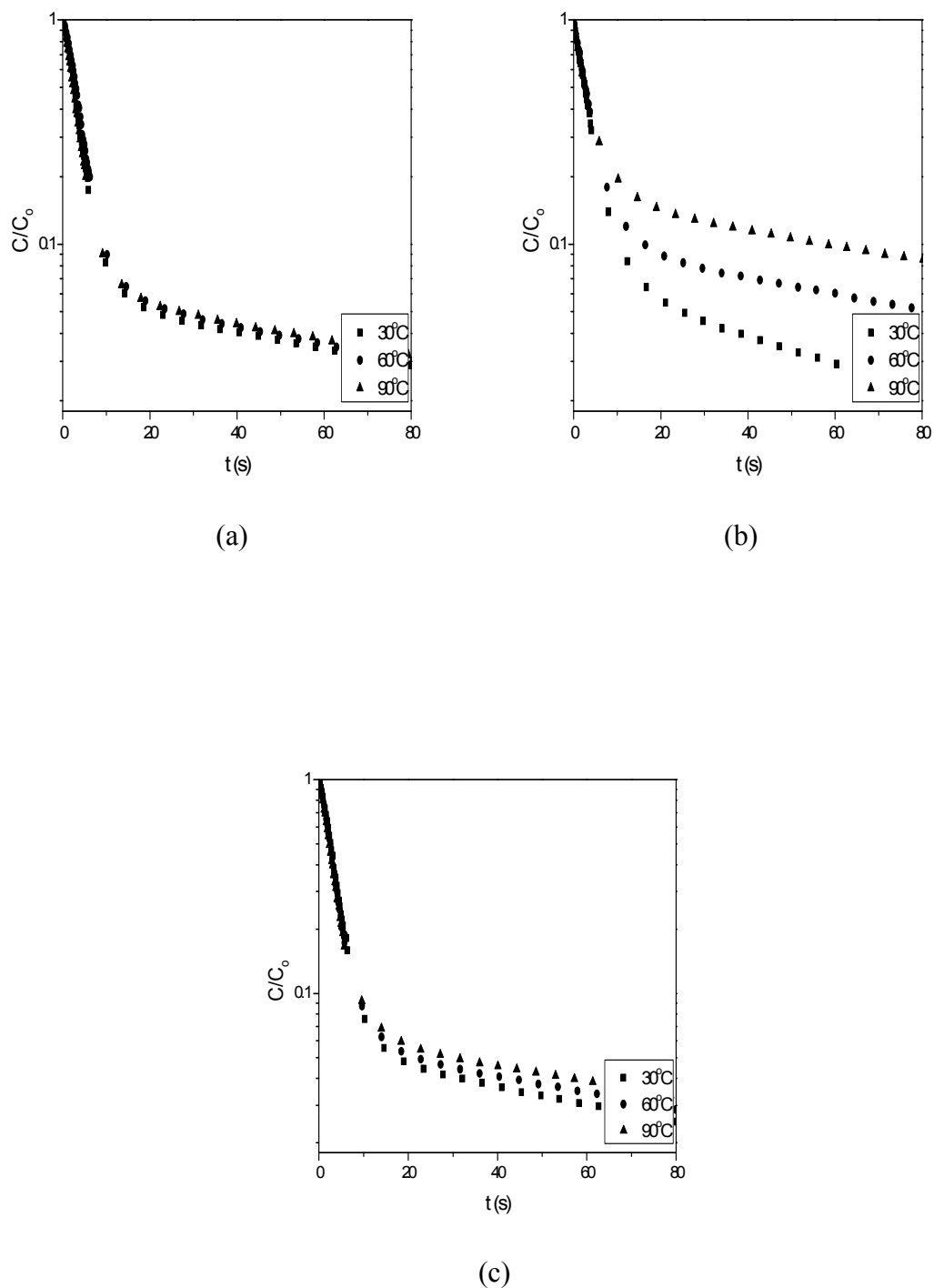


Figure 7.38. ZLC response curves of CeNaX-U for (a) N₂ (b) CO₂ (c) CH₄.

L value of CO₂, N₂ and CH₄ were found to be greater than 5 revealing that the process was controlled by the micropore diffusion (Equation 5.16). The low value of the micropore time constant ($D_c/r^2 \ll 0.05$) also shows that internal mass transfer resistance is the controlling step (Karger and Ruthven, 1992).

Table 7.13. Kinetic and equilibrium parameters of N₂, CO₂ and CH₄ adsorption.

Adsorbent \ Adsorbate	T (K)	NaX					LiX-U					CaNaX-U					CeNaX-U				
		L (-)	D _c x10 ¹⁴ (m ² s ⁻¹)	D _c /r ² x10 ⁴ (s ⁻¹)	K (-)	R ²	L (-)	D _c x10 ¹⁶ (m ² s ⁻¹)	D _c /r ² x10 ⁴ (s ⁻¹)	K (-)	R ²	L (-)	D _c x10 ¹⁶ (m ² s ⁻¹)	D _c /r ² x10 ⁴ (s ⁻¹)	K (-)	R ²	L (-)	D _c x10 ¹⁸ (m ² s ⁻¹)	D _c /r ² x10 ⁴ (s ⁻¹)	K (-)	R ²
N ₂	303	41	0.12	12	8410	0.9895	47	8.8	8.8	10587	0.9946	45	40	40	2147	0.9972	400	26	0.26	45565	0.9871
	333	72	0.05	5	11600	0.9905	182	1.6	1.6	15054	0.9822	85	11	11	4048	0.9953	1111	4	0.04	102909	0.9854
	363	48	0.04	4	23500	0.9802	775	0.063	0.1	90217	0.9951	39	9	9	11080	0.9962	1429	2	0.02	151512	0.9829
CH ₄	303	7	1.21	121	4690	0.9822	85	6.6	6.6	7859	0.9936	51	30	30	2532	0.9851	233	96	0.96	21018	0.9863
	333	5	1.17	117	6950	0.9917	112	2.5	2.5	15498	0.9931	68	12	12	4694	0.9867	333	40	0.40	34995	0.9855
	363	5	1.15	115	7580	0.9855	106	2.3	2.3	17638	0.9915	51	7	7	11242	0.9861	2500	1	0.007	287040	0.9853
CO ₂	303	14	0.12	12	24700	0.9946	116	1.2	1.2	31561	0.9821	31	5	5	26278	0.9954	53	908	9.08	9801	0.9925
	333	48	0.15	15	18900	0.9822	20	14	14	16131	0.9775	34	6	6	19366	0.9957	33	550	5.50	26043	0.9940
	363	31	0.24	24	5333	0.9951	25	18	18	9984	0.9795	28	9	9	15955	0.9964	21	500	5.00	45386	0.9960

Figure 7.39 shows the Arrhenius plot showing the effect of temperature on the micropore (or crystal) diffusivities, D_c , in NaX, LiX-U, CaNaX-U and CeNaX-U zeolites. The corresponding parameters (E_a and D_o/r^2) of the Arrhenius equation;

$$D_c = D_o \exp\left(-\frac{E_a}{RT}\right) \quad (5.27)$$

were tabulated in Table 7.14. The negative value of activation energy is unexpected result. The future project is to repeat the measurement in the wide range of temperature.

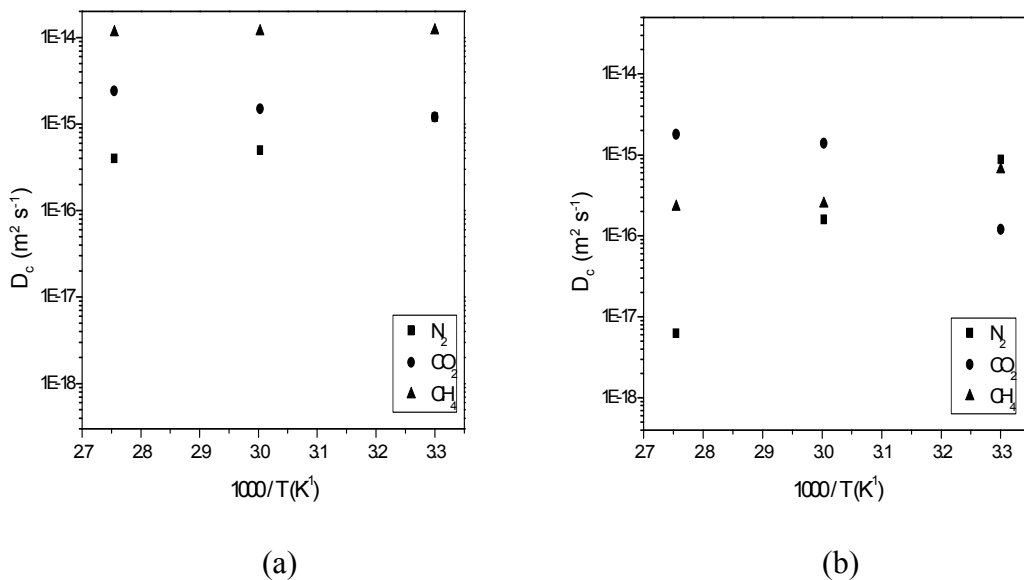


Figure 7.39. Temperature dependence of micropore diffusion coefficient for (a) NaX (b) LiX-U (c) CaNaX-U (d) CeNaX-U.

(cont. on next page)

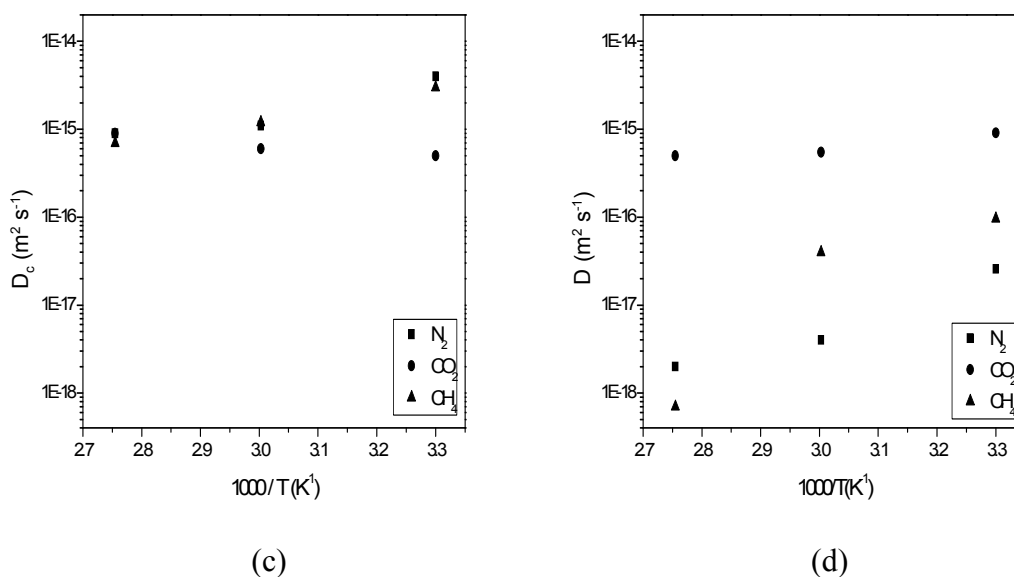


Figure 7.39. (cont.).

Table 7.14. Arrhenius equation parameters for zeolites

Adsorbates	Zeolite Codes	D_0/r^2 (s ⁻¹)	E_a (kJ mol ⁻¹)
N ₂	NaX	1.3×10^{-6}	-17.0
	LiX-U	1.8×10^{-16}	-74.4
	CaNaX-U	3.5×10^{-7}	-23.2
	CeNaX-U	3.5×10^{-12}	-39.5
CO ₂	NaX	7×10^{-2}	10.4
	LiX-U	3×10^3	42.2
	CaNaX-U	1.6×10^{-2}	8.8
	CeNaX-U	2.2×10^{-5}	-9.3
CH ₄	NaX	9×10^{-3}	-0.8
	LiX-U	9×10^{-7}	-16.4
	CaNaX-U	4×10^{-7}	-22.3
	CeNaX-U	4×10^{-17}	-73.4

Although an increase in crystalline diffusivity with temperature was expected, reverse behavior was seen in Henry's constant. Henry constant, K , showing the

interaction between the adsorbent surfaces and the adsorbed gas molecules, was calculated by using the equation 5.19 and presented in Table 7.13. The plots of Henry's constant versus the reciprocal temperature were given in Figure 7.40. The heat of CO₂, CH₄ and N₂ adsorption on the zeolites were calculated from the Henry's constant collected at 303 K, 333 K and 363 K by using Van't Hoff equation

$$K = K_0 \exp(-\Delta H / RT) \quad (5.26)$$

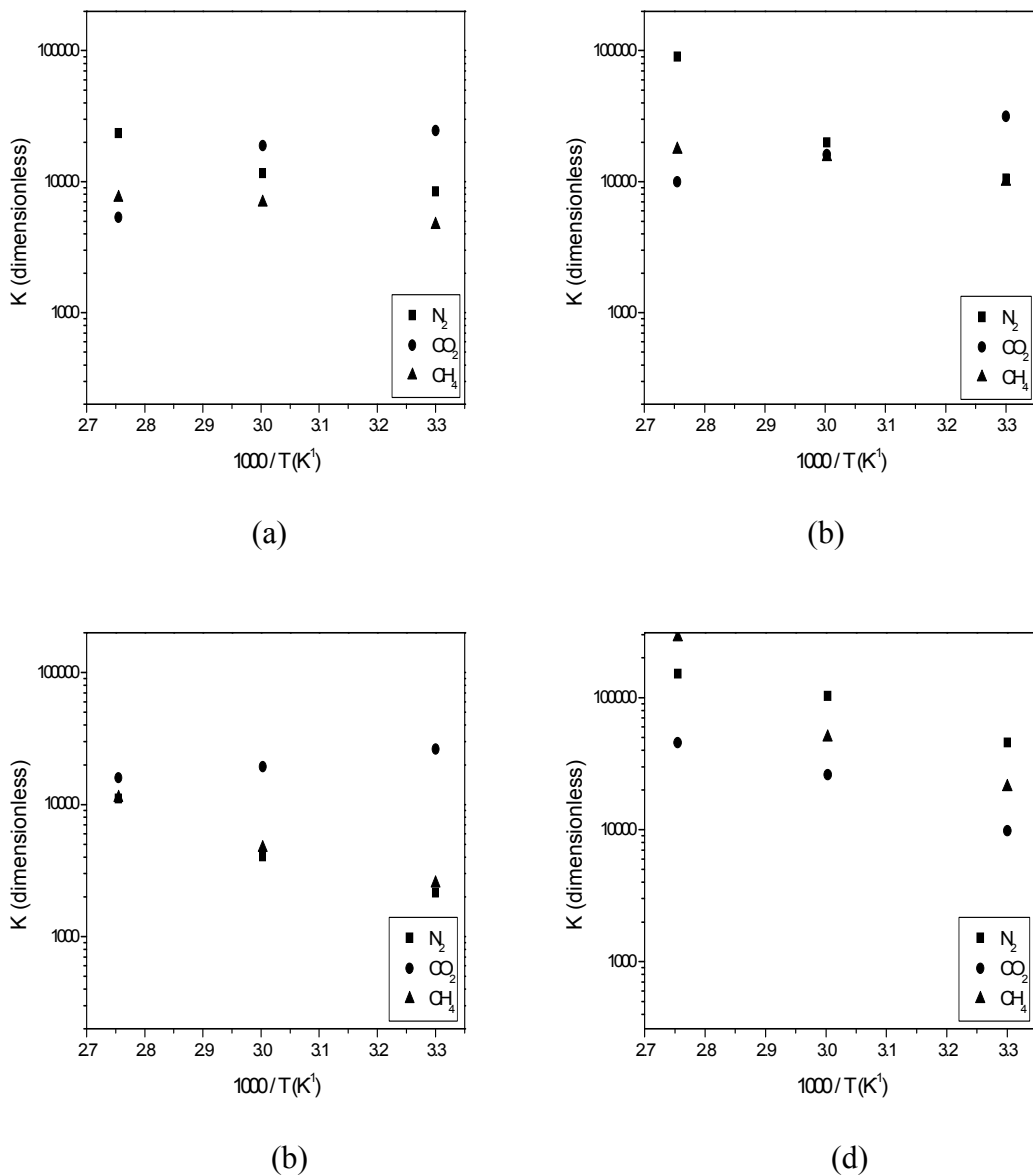


Figure 7.40. Van't Hoff plots showing temperature dependence of the Henry constants for (a) NaX (b) LiX-U (c) CaNaX-U (d) CeNaX-U zeolites.

As seen from Table 7.15, the results obtained from this study agree well with the results given in the literature for N₂ and CH₄. According to our results, the heat of N₂ and CH₄ adsorption on the all zeolites are endothermic. On the other hand, CO₂ adsorption on the NaX, LiX-U and CaNaX-U zeolites is exothermic. Since the adsorption process is exothermic, the negative heat of adsorption values will produce heat within adsorbent in ZLC during an adsorption. This increase in the column temperature will have an adverse effect on adsorption capacities of the adsorbent as stated by Harlick and Tezel (2004). Large temperature drop may also cause moisture on the adsorbent. However, the CO₂ interaction with NaX, LiX-U and CaNaX-U zeolites were found as an exothermic adsorption process, the parameters reported in Table 7.13 are merely fitting parameters and no physical meaning was attributed to them as stated by Cavenati et al. (2006). CO₂ adsorption on CeNaX-U zeolite showed endothermic reaction comparing to the others. Cerium ion is transition metal ion and can coordinate to adsorbate molecules with different adsorption behavior due to the presence of d-shell as stated by Sebastian et al. (2007).

The heat of adsorption of CH₄ on Li-, Ca- and Ce- exchanged zeolites was found in the order of; CeNaX-U > CaNaX-U > LiX-U > NaX. It can be explained with the charge density of the cations. Heat of adsorption increases with the charge density of monovalent, divalent and trivalent cations as stated by Peter et al. (2005). Charge density of Na⁺, Li⁺, Ca²⁺ and Ce³⁺ ions are 16.9, 23.6, 32.4 and 46.7 Cm⁻¹x10⁻¹⁰, respectively (Peter et al., 2005). The reverse behaviour was obtained with the N₂ adsorption on cation exchanged zeolites. It can be explained with the location of nitrogen molecules in X zeolites. Nitrogen molecules interact with the SII and SIII of the zeolite structure. Li⁺ ions prefer to occupy the SII and SIII of the zeolite structure in the ion exchange experiment which causes the strong interaction of the nitrogen molecule with extra-framework lithium ion comparing to the Ca²⁺ and Ce³⁺ ions (Habgood, 1964).

Therefore, it has been observed that the heat of N₂, CO₂ and CH₄ adsorption was varied with the type of counter ions on the zeolites (Table 7.15). Since, the type, size and location of the counter ions affect the local electric fields as well as adsorbate polarization. N₂, CO₂ and CH₄ molecules interact with the zeolite surface through lattice oxygen atoms and accessible extra-framework cations. The Al and Si atoms are not directly interact with adsorbate molecules (Sebastian et al., 2007).

Table 7.15. Heat of adsorption of NaX and cation exchanged NaX zeolite.

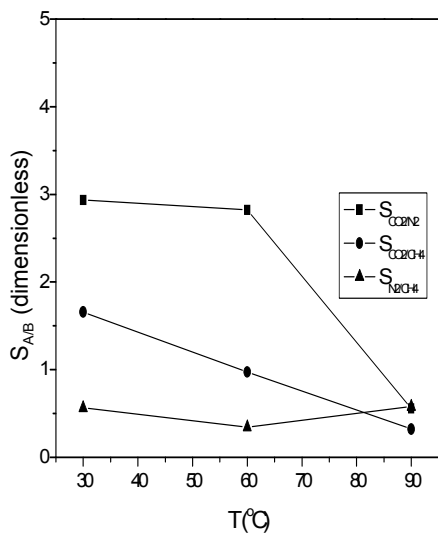
Adsorbates	Adsorbents	Temp.range (K)	ΔH (kJ mol ⁻¹)	Method Used
CO ₂ $\sigma=3.30 \text{ \AA}$ $\mu=0.64 \text{ \AA}^3$ $\alpha=1.9 \text{ \AA}^3$	NaX	303-363	-26	ZLC
	*NaX	295-343	34	Volumetric Ads. System
	LiX-U	303-363	-18	ZLC
	CaNaX-U	303-363	-8	ZLC
	CeNaX-U	303-363	23	ZLC
N ₂ $\sigma=3.64 \text{ \AA}$ $\mu=0.31 \text{ \AA}^3$ $\alpha=1.4 \text{ \AA}^3$	NaX	303-363	15	ZLC
	*NaX	295-343	17	Volumetric Ads. System
	LiX-U	303-363	33	ZLC
	CaNaX-U	303-363	25	ZLC
	CeNaX-U	303-363	18	ZLC
CH ₄ $\sigma=3.8 \text{ \AA}$ $\mu=0 \text{ \AA}^3$ $\alpha=2.6 \text{ \AA}^3$	NaX	303-363	11	ZLC
	*NaX	295-343	14	Volumetric Ads. System
	LiX-U	303-363	13	ZLC
	CaNaX-U	303-363	23	ZLC
	CeNaX-U	303-363	39	ZLC

* ΔH values obtained from literature (Source: Rege et al., 2001)
 σ : kinetic diameter, α : polarizability μ : quadrupolar moment

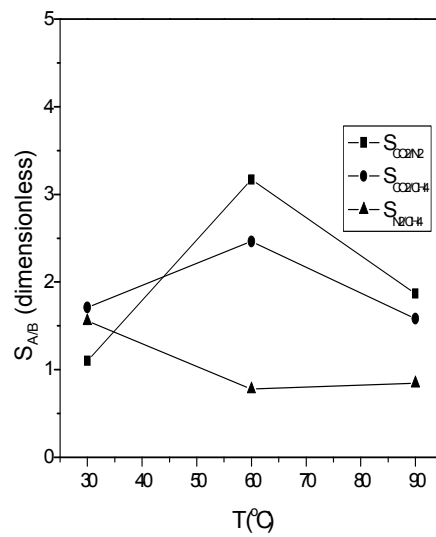
Selectivity

The kinetic selectivity gives an idea about which adsorbent the best to separate gas mixture. The kinetic selectivity of gas A over gas B, $S_{A/B}$ depends on both adsorption rate and equilibrium.

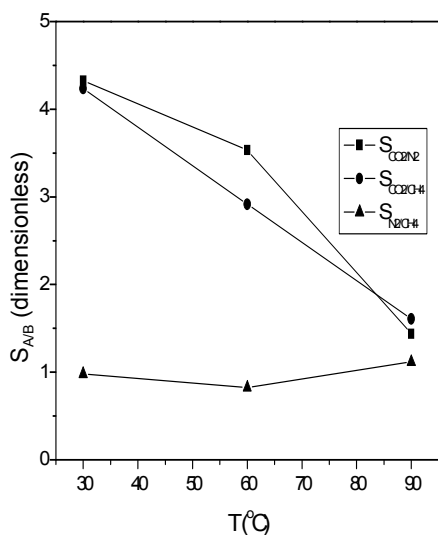
$$S_{A/B} = \frac{K_A}{K_B} \sqrt{\frac{D_A}{D_B}} \quad (5.24)$$



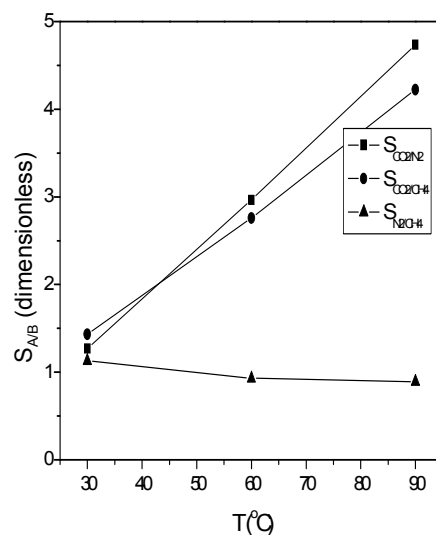
(a)



(b)



(c)



(d)

Figure 7.41. The kinetic selectivity, $S_{A/B}$, for (a) NaX (b) LiX-U (c) CaNaX-U (d) CeNaX-U

The average pore diameter of the adsorbents (5.67, 7.05, 7.58 and 8.28 for NaX, LiX, CaNaX-U and CeNaX-U respectively) are convenient for CO_2 , N_2 and CH_4 adsorption. The selectivities, S_{CO_2/CH_4} , S_{CO_2/N_2} , S_{N_2/CH_4} , were calculated and presented as a function of temperature (Figure 7.41). The kinetic selectivity is lower than 5 for all the adsorbents. The lowest selectivities are obtained for NaX zeolite. The separation of N_2 over CH_4 is very difficult kinetically for all the adsorbents. CO_2 selectivity over CH_4

and N_2 is decreased with increasing temperature surprisingly for NaX and CaNaX-U zeolites, although the other kinetic selectivities are increased with temperature. The CO_2 selectivity over CH_4 and N_2 are higher than N_2 selectivity over CH_4 for all the adsorbents ($S_{CO_2/CH_4}, S_{CO_2/N_2} > S_{N_2/CH_4}$). This can be explained with the high electrostatic interaction and the low kinetic diameter of CO_2 than the other gases.

CHAPTER 8

CONCLUSION

In this study, the exchange of Li^+ , Ca^{2+} and Ce^{3+} ions with the Na^+ ions in synthetic X zeolites was performed. The effect of the counter ion concentration (3-9 fold equivalent excess) and temperature (50 °C and 70 °C) on the exchange were examined kinetically in the presence of ultrasound. The results were compared with those obtained from traditional batch method.

The kinetics of ion exchange was very fast and completed within about 15 min. The exchange levels were increased with temperature and the fold equivalent excess used. Maximum exchange percent was obtained as 76, 72 and 66 for Li^+ , Ca^{2+} and Ce^{3+} ions exchange, respectively. The parameters; the fold equivalent excess, temperature and ultrasound are more effective in Li^+ ion exchange than Ca^{2+} and Ce^{3+} ions exchange. The Li^+ , Ca^{2+} and Ce^{3+} ions exchange in ultrasonic bath were also examined to show the effect of ultrasonic sources. The results showed that ultrasonic probe is more effective than ultrasonic bath and traditional methods.

The ion exchange data are fitted with the reaction and diffusion models and reached the following results:

- With the fold equivalent excess, the rate of lithium exchange was decreased significantly in the traditional method, but increased in case of ultrasonic method. For multivalent cations, the rate of calcium and cerium exchange were irregularly changed. The intraparticle diffusion coefficient for Li^+ and Ca^{2+} ion exchange was increased with decreasing counter ions concentration in both exchange methods. The disordered change in diffusion coefficient with counter ion concentration was observed for Ce^{3+} ion exchange.

The reason to do not observe the effect of hydrated radius on the rate of exchange or the diffusion coefficients can be attributed to lower contribution of Van der Waals interaction than electrostatic interactions.

- The equilibrated values (q_e) were increased with increasing Li^+ and Ca^{2+} ions concentration in solution for both exchange methods. However, the effect of solution concentration on the equilibrium could not be observed for Ce^{3+} ion.
- It can be concluded that the presence of more than one resistances (intraparticle or/and external film resistance) to the ion exchange should be considered.
- The effect of ultrasound on the external film resistance is not clear surprisingly.
- Mass transfer rate constant in the external film, k_f , was changed irregularly with initial concentration even the experimental data were well correlated with the model ($R^2 > 0.94$). The k_f values are increased with decreasing the valence of the counter ions. The order of the k_f values is; Li^+ ion exchange $>$ Ca^{2+} ion exchange $>$ Ce^{3+} ion exchange.
- Bi_m values are about 0.1 which is the critical value to decide the controlling step in mass transfer. Therefore both intraparticle and external film diffusion are comparable for Li^+ , Ca^{2+} and Ce^{3+} ions exchange. However the external film mass transfer resistance seems to be pronounced for multivalent cations than monovalent cation due to low Bi_m number.
- The activation energy and thermodynamics parameters by using the change in the intraparticle diffusion rate constant, k_i , with temperature showed that the rise in the solution temperature favour Li^+ , Ca^{2+} and Ce^{3+} ions exchange onto NaX zeolite. The activation energies for the ion exchange showed that the intraparticle diffusion is dominant and the cation exchange reactions are the endothermic reactions due to positive values of enthalpy of activation. However, the effect of temperature on the exchange is not clear since the range of the temperature is low. The enthalpy of activation for Li^+ ion exchange is lower in ultrasonic method than traditional method. This means that lithium is replaced by sodium with strong electrostatic interaction when the traditional method was used.
- At the end of the kinetic models, reaction and diffusion models showed that, the chemical reaction was dominant at initial of the ion exchange and followed by a slower process till equilibrium attained. At this time, the intraparticle, besides to external film resistance were involved in the ion exchange as the rate controlling steps.

Ion exchange experiments were also conducted by refreshing the counter cation solution to obtain fully exchanged Li-, Ca- and Ce- zeolites. It was found that Li^+ and Ca^{2+} ions replaced by Na^+ ion with the extent of 100 % and 94 %, respectively, with the both exchange methods. The effect of the method is more evident in Ce^{3+} ion exchange; 62 % from traditional method and 73 % from ultrasonic method. Formation of mesopores with introduction of calcium was observed whatever method used in Ca^{2+} ion exchange. The maximum surface area was obtained in Li^+ ion exchange by ultrasonic probe method but ultrasonic bath method or traditional method in Ca^{2+} and Ce^{3+} ion exchange. The micrographs of the surface obtained from scanning electron microscope showed that the crystal size (2 μm) of NaX zeolite did not change with ultrasonic source or the methods used in Li^+ , Ca^{2+} or Ce^{3+} ions exchange. The X-ray diffractogram of the zeolites showed that NaX zeolite has the highest peak and highly crystalline material but its peak intensity reduced with Li-, Ca- and Ce-exchange process.

The NaX crystals were tried to form into granule form to provide high physical strength and high attrition resistance. Sepiolite and montmorillonite minerals were used as inorganic binders. When weight percentage of binders increased, strength of the granule increased. However, it was seen that NaX granule without binder has the highest textural properties. Because of the necessity of the adsorbents at very small size in ZLC system, the crystal form of the samples are preferred in the experiments.

CO_2 , N_2 and CH_4 adsorption at 30 °C, 60 °C and 90 °C were studied by using Zero length column (ZLC) technique. The length of the ZLC was very short and thin layer of adsorbent having 2 μm crystal size between two porous sintered discs was used which provides well mixed cell. Thus it minimizes the external resistance to heat and mass transfer. The experimental data were evaluated to calculate the diffusion coefficients and equilibrium constants of CO_2 , N_2 and CH_4 gases.

- The low value of the micropore time constant ($D_e/r^2 \ll 0.05$) showed that internal mass transfer resistance is the controlling step.
- The results of heat of adsorption for NaX zeolite over the N_2 (15 kJ mol^{-1}) and CH_4 (11 kJ mol^{-1}) well agree with the results given in the literature (17 and 14 kJ mol^{-1} , respectively).
- The separation of N_2 over CH_4 is very difficult kinetically for all the adsorbents.

- The CO₂ selectivity over CH₄ and N₂ are higher than N₂ selectivity over CH₄ for all the adsorbents ($S_{CO_2/CH_4}, S_{CO_2/N_2} > S_{N_2/CH_4}$). This can be explained with the high electrostatic interaction and the low kinetic diameter of CO₂ than the other gases.

REFERENCES

- Ackley, M.W.; Rege, A.U.; Saxena, H. Application of Natural Zeolites in the Purification and Separation of Gases. *Microporous and Mesoporous Materials*, **2003**, 61, 25–42.
- Akbar, S.; Shah, T.H.; Shahnaz, R.; Sarwar, G. Thermal Studies of Synthetic NaX Zeolite and its Zinc Exchanged Forms. *Jour. Chem. Soc. Pak*, **2007**, 29, 5-11.
- Al-Ghouti, M.; Khraisheh, M.; Ahmad, M.; Allen, S. Thermodynamic Behaviour and the Effect of Temperature on the Removal of Dyes from Aqueous Solution Using Modified Diatomite: A kinetic study. *Journal of Colloid and Interface Science*, **2005**, 287, 6–13.
- Ash, R.; Barrer R.M.; Craven R.J.B. *Sorption Kinetics and Time-Lag Theory. Part I: Constant Diffusion Coefficient*. Imperial College, London, **1977**.
- ASTM International E 728-91. Standards Test Method for Resistance to Attrition of Granular Carriers and Granular Pesticides. United States. **2004**, p.133-134.
- Barcia, P.S.; A.C. Silva, J.; Rodrigues, E.A. Adsorption Equilibrium and Kinetics of Branched Hexane Isomers in Pellets of BETA Zeolite. *Microporous and Mesoporous Materials*, **2005**, 79, 145–163.
- Barman, S.; Pradhan, N.C.; Basu, J.K. Kinetics of Alkylation of Phenol with Methanol over Ce-Exchanged NaX Zeolite. *Catalysis Letters*, **2006**, 111, 67-73.
- Barros, M.A.S.D.; Araujo, JR.,I.F.; Arroyo, P.A.; Sousa-Aguiar, E.F.; Tavares, C.R.G. Multicomponent Ion Exchange Isotherms in NaX Zeolite. *Latin American Applied Research*, **2003**, 33, 339-344.
- Bekkum, H.V.; Flanigen, E.M.; Jacobs, P.A.; Jansen, J.C. *Introduction to Zeolite Science and Practice*; 2nd completely revised and expanded edition, Elsevier Science Publishing Company Inc. Newyork, **2001**
- Brandani, F.; Brandani, S.; Coe, C.G.; Ruthven, D.M. Measurement of Henry Constants and Equilibrium Isotherms by the ZLC Technique. *Fundamentals of Adsorption*, **2002**, 7, 21 - 28.
- Brandani, F.; Ruthven, D. ZLC Response for Systems with Surface Resistance Control. *Adsorption*, **2005**, 11, 31-34.
- Brandani, F.; Ruthven, D.; Coe, C.G. Measurement of Adsorption Equilibrium by the Zero Length Column (ZLC) Technique Part 1: Single-Component Systems. *Ind. Eng. Chem. Res.*, **2003**, 42, 1451-1461.
- Brandani, S.; Gunadi, A. Diffusion of Linear Paraffins in NaCaA Studied by the ZLC Method. *Microporous and Mesoporous Materials*, **2006**, 90, 278–283.

- Brandani, S.; Ruthven, D.M. Analysis of ZLC Desorption Curves for Gaseous Systems. *Adsorption*, **1996**, 2, 133-143.
- Brandani, S.; Xu, Z.; Ruthven D. Transport Diffusion and Self-diffusion of Benzene in NaX and CaX Zeolite Crystals Studied by ZLC and Tracer ZLC Methods. *Microporous Materials*, **1996**, 7, 323-331.
- Braun, A.; Evans, D.; Gandhi, P.M.; Garamszeghy M.; Geiser H.; Hooper E.W.; Kaufmann, F.D.; Luycx, P.; Martynoy, B.; Mezga, L.J.; Neubauer, J.; Norden M.; Pecha, M.; Piacek, P.; Potrok, M.; Sinha, P.K.; Stevens, T.; Tusa, E.; Zika, H. *Application of Ion Exchange Processes for the Treatment of Radioactive Waste and Management of Spent Ion Exchangers*. Technical Reports Series No. 408, International Atomic Energy Agency: Vienna, **2002**.
- Breck, D.W. *Physical Properties of Crystalline Zeolites in Zeolite Molecular Sieves: Structure, Chemistry and Use*; A Wiley-Interscience Publication: New York, **1974**.
- Broach, W.R. *Zeolite in Industrial Separation and Catalysis*. Edited by Santi Kulprathipanja, Wiley-VCH Verlag GMBH&Co. KGaA, **2010**.
- Buhl, J.-Ch.; Gerstmann, M.; Lutz, W.; Ritzmann, A. Hydrothermal Stability of the Novel Zeolite Type LSX in Comparison to the Traditional 13X Modification, Hannover, *Institut für Mineralogie*, **2003**.
- Buhl, J-Ch.; Gerstmann, M.; Lutz, W.; Ritzmann, A. Hydrothermal Stability of the Novel Zeolite Type LSX in Comparison to the Traditional 13X Modification. *Z. Anorg. Allg. Chem.*, **2004**, 630, 604-608.
- Castro, L.M.D.; Capote, F.P. *Techniques and Instrumentation In Analytical Chemistry : Analytical Applications of Ultrasound*. Elsevier B.V. Volume 26, **2007**.
- Cavenati, S.; Grande, C.A.; Rodriques, A.E. Removal of Carbon Dioxide from Natural Gas by Vacuum Pressure Swing Adsorption. *Energy & Fuel*, **2006**, 20, 2648-2659.
- Chatterjee, A.; Mizukami, F. Location and Role of Exchangeable Cations in Zeolite Catalysis:a First Principle Study. *Chemical Physics Letters*,. **2004**, 385, 20–24.
- Crank, J. *The Mathematics of Diffusion*, Second Edition, Oxford Science Publications, **2003**.
- Crittenden, J. C.; Wong, B. W. C.; Thacker, W. E.; Hinrichs, R. L. Mathematical Model of Sequential Loading in Fixed Bed Adsorbers. *J. Water Pollut. Cont. Fed.*, **1980**, 52, (11), 2780.
- Dabrowski, A. Adsorption from theory to practice. *Advances in Colloid and Interface Science*, **2001**, 93,135-224.

- DePaoli, S.M.; Perona, J.J. Model for Sr-Cs-Ca-Mg-Na Ion-Exchange Uptake Kinetics on Chabazite. *AIChE Journal*, **1996**, 42, 3434-3441.
- DeSilva, F.J. *Essentials of Ion Exchange*. Presented at the 25th Annual WQA Conference, **1999**.
- Diaz, E.; Ordonez, S.; Vega, A.; Coca, J. Characterization of Co, Fe and Mn-Exchanged Zeolites by Inverse Gas Chromatography. *Journal of Chromatography A*, **2004**, 1049, 161–169.
- Do, D.D. *Adsorption Analysis: Equilibria and Kinetics*; Imperial College Press: London, **1998**.
- Dyer, A.; White, K.J. Cation Diffusion in the Natural Zeolite Clinoptilolite. *Thermochimica Acta*, **1999**, 340-341, 341-348.
- Eic, M.; Micke, A.; Kocirik, M.; Jama, M.; Zikanova, A. Diffusion and Immobilization Mechanisms in Zeolites Studied by ZLC Chromatography. *Adsorption*, **2002**, 8: 15–22.
- Entezari, M.H.; Tahmasbi, M. Water Softening by Combination of Ultrasound and Ion Exchange. *Ultrason. Sonochem.*, **2009**, 16, 356-360.
- Faghihian, H.; Amini, M.K.; Nezamzadeh, A.R. Cerium Uptake by Zeolite A Synthesized from Natural Clinoptilolite Tuffs. *Journal of Radioanalytical and Nuclear Chemistry*, **2005**, 264, 577-582.
- Findik, S.; Gündüz, G.; Gündüz, E. Direct Sonication of Acetic Acid in Aqueous Solutions. *Ultrasonic Chemistry*, **2006**, 13, 203-207.
- Friedman, G. *Mathematical Modeling of Multicomponent Adsorption in Batch and Fixed-Bed Reactors*. MS Thesis, Michigan Technological Univ., Houghton. **1984**.
- Fujimoto, Y.; Nakatsuka, M. A Novel Method for Uniform Dispersion of the Rare Earth Ions in SiO₂ Glass Using Zeolite X. *Journal of Non-Crystalline Solids*, **1997**, 215, 182-191.
- Grande, C.A.; Silva, V.M.T.M.; Gigola, C.; Rodrigues, A.E. Adsorption of Propane and Propylene onto Carbon Molecular Sieve. *Carbon*, **2003**, 41, 2533-2545.
- Guimarães, A.P.; Möller, A.; Staudt R.; Azevedo D.C.; Lucena, S.M.P.; Cavalcante C.L. Diffusion of Linear Paraffins in Silicalite Studied by the ZLC Method in the Presence of CO₂. *Adsorption*, **2010**, 16, 29–36.
- Gupta, A.; Gaur, V.; Verma, N. Breakthrough Analysis for Adsorption of Sulfur-Dioxide over Zeolites. *Chemical Engineering and Processing*, **2004**, 43, 9 -22.
- Habgood, H.W. Adsorptive and Gas Chromatographic Properties of Various Cationic Forms of Zeolite X. *Canadian Journal of Chemistry*, **1964**, 42, 2340-2350.

- Hamdaoui, O.; Naffrechoux, E. An Investigation of the Mechanisms of Ultrasonically Enhanced Desorption. *AIChE Journal*, **2007**, 53, 363-373.
- Harlick, P.J.E.; Tezel, F.H. An Experimental Adsorbent Screening Study for CO₂ Removal from N₂. *Microporous and Mesoporous Materials*, 2004, 76, 71-79.
- Helfferich, F.G. *Ion Exchange*. McGraw-Hill, New York, **1962**.
- Ho, Y.S.; Wase, D.A.J.; Forster, C.F.; Batch Nickel Removal from Aqueous Solution by Sphagnum Moss Peat. *Water Research*, **1995**, 29 (5), 1327-1332.
- Ho, Y. S.; McKay, G. *Can. J. Chem. Eng.*, **1998**, 76, 822.
- Ho, Y.S. Citation Review of Lagergren Kinetic Rate Equation on Adsorption Reactions. *Scientometric*, **2004**, 1, 171-177.
- Ho, Y.S. Pseudo-isotherms Using a Second Order Kinetic Expression Constant. *Adsorption*, **2004**, 10, 151-158.
- Huften, R.J.; Ruthven, M.D. Diffusion of Light Alkanes in Silicalite Studied by the Zero Length Column Method. *Ind. Eng. Chem. Res.*, **1993**, 32, 2379-2386.
- Hutson, N.D.; Rege, S.U.; Yang, R.T. Mixed cation zeolites: Li_xAg_y-X as a Superior Adsorbent for Air Separation. *AIChE Journal*, **1999**, 45, 724-734.
- Ibrahim, W.A.; Hassan, L.A. *Determination of Surface Diffusion Coefficient for Lead Removal Using Adsorption Model*. Twelfth International Water Technology Conference, (IWTC12), Alexandria, Egypt., **2008**.
- Iliyas, A.; Eic, M.; Zahedi-Niaki, M.H.; Vasenkov, S.; Toward Observation of Single-File Diffusion Using the Tracer Zero-Length Column Method. *J.Phys. Chem. B.*, **2008**, 112, 3821-3825.
- Incropera, F.P.; Dewitt, D.P.; Bergman, T.L.; Lavine A.S. *Fundamentals of Heat and Mass Transfer*, John Wiley and Sons, Inc., pg. 260-261, **2007**.
- Inglezakis, V.J.; Pouloupoulos, S.G. *Adsorption, Ion exchange and Catalysis Design of Operations and Environmental Applications*; Elsevier, **2006**.
- Jasra, R.V.; Tyagi, B.; Badheka, Y.M.; Choudary, V.N.; Bhat, T.S.G. Effect of Clay Binder on Sorption and Catalytic Properties of Zeolite Pellets. *Ind. Eng. Chem. Res.*, **2003**, 42, 3263-3272.
- Ji, J.; Lu, X.; Xu, Z. Effect of Ultrasound on Adsorption of Geniposide on Polymeric Resin. *Ultrasonics Sonochemistry*, **2006**, 13, 463-470.
- Karge, H.; Weitkamp, J. *Adsorption and Diffusion: Molecular Sieves, Science and Technology*; Springer-Verlag Berlin Heidelberg, **2008**.

- Karger, J.; Ruthven, D. M. *Diffusion in Zeolites and Other Microporous Solids*; John Wiley and Sons: New York, **1992**.
- Keller, J.U.; Staudt, R. *Gas Adsorption Equilibria: Experimental Methods And Adsorptive Isotherms*; Springer Science and Business Media: Boston, **2005**.
- Kim, J. B. Li⁺- and H⁺- Exchanged Low Silica X Zeolite as Selective Nitrogen Adsorbent for Air Separation. *Bull. Korean Chem. Soc.*, **2003**, 24, 1814-1817.
- Kim, K-H.; Kim, K-B. Ultrasound Assisted Synthesis of Nano-sized Lithium Cobalt Oxide. *Ultrasonics Sonochemistry*, **2008**, 15, 1019-1025.
- Kitagawa, S.; Kitaura, R.; Noro, S. Review: Functional Porous Coordination Polymers. *Angew. Chem. Int. Ed.*, **2004**, 43, 2334–2375.
- Klima, J. Application of Ultrasound in Electrochemistry. An Overview of Mechanisms and Design of Experimental Arrangement. *Ultrasonics*, **2011**, 51, 202-209.
- LeVan, M.D.; Carta, G. *Adsorption and Ion Exchange*; Perry's Chemical Engineers' Handbook, 8th Edition, Section 16, McGraw-Hill Professional, **2007**.
- Loos, J-B W.P.; Verheijen, P.J.T.; Moulijn, J.A. Improved Estimation of Zeolite Diffusion Coefficients from Zero-Length Column Experiments. *Chemical Engineering Science*, **2000**, 55, 51-65.
- Malekian, A.; Vinh-Thang, H.; Huang, Q.; Eić, M.; Kaliaguine, S. Evaluation of the Main Diffusion Path in Novel Micro-Mesoporous Zeolitic Materials with the Zero Length Column Method. *Ind. Eng. Chem. Res.*, **2007**, 46, 5067–5073.
- Mier, M.V.; Callejas, R.L.; Gehr, R.; Jimeâ Nez Cisneros, B.E.; Alvarez, P.J. Heavy Metal Removal With Mexican Clinoptilolite: Multi-Component Ionic Exchange. *Wat. Res.*, **2001**, 35: 2, pp. 373-378.
- Mounts, T.L. Chemical and Physical Effects of Processing Fats and Oils. *JAOCS.*, **1981**, 51A-54A.
- Murray, H.H. Traditional and New Applications for Kaolin, Smectite, and Palygorskite: a General Overview. *Applied Clay Scienc.*, **2000**, 17, 207-221.
- Peter, S.A.; Moharir, A.S.; Jasra, V.R. Selective Adsorption of Oxygen over Argon in Alkaline-Earth-Metal Cation-Exchanged Zeolite X. *Ind. Eng. Chem. Res.*, **2010**, 49, 7524–7529.
- Peter, S.A.; Sebastian, J.; Jasra, R.V. Adsorption of Nitrogen, Oxygen, and Argon in Mono-, Di-, and Trivalent Cation-Exchanged Zeolite Mordenite. *Ind. Eng. Chem. Res.*, **2005**, 44, 6856-6864.

- Plesset, M.S.; Chapman, R.B. Collapse of an Initially Spherical Vapour Cavity in the Neighbourhood of a Solid Boundary. *Journal of Fluid Mechanics*, **1971**, 47, 283-290.
- Qiu, H.; Pan, B.; Zhang, Q.J.; Zhang, W.M.; Zhang, Q.X. Critical Review in Adsorption Kinetic Models. *Journal of Zhejiang University Science A.*, **2009**, 10, 716-724.
- Ranz, W.E.; Marshall, W.R. Evaporation from Drops, Part I. *Chemical Engineering Progress*, **1952**, 48, 141–146.
- Ranz W.E.; Marshall, W.R. Evaporation from Drops, Part II. *Chemical Engineering Progress*, **1952**, 48, 173–180.
- Rege, S.U.; Yang, R.T.; Chain, C. A. Desorption by Ultrasound: Phenol on Activated Carbon and Polymeric Resin. *AIChE Journal*, **1998**, 44, 1519-1528.
- Rege, S.U.; Yang, R.T.; Qian, K.; Buzanowski, M.A. Air-Prepurification by Pressure Swing Adsorption Using Single/layered Beds. *Chemical Engineering Science*, **2001**, 56, 2745-2759.
- Rodriguez-Reinoso, F.; Molina-Sabio, M.; Gonza'lez, J.C. Preparation of Activated Carbon–Sepiolite Pellets. *Carbon*, **2001**, 39, 771 –785.
- Rouquerol, F.; Rouquerol, J.; Sing, K. S. W. *Adsorption by Powders and Porous Solids: Principles, Methodology and Applications*; Academic Press, San Diego, **1999**.
- Ruthven, M.D. *Principles of Adsorption and Adsorption Processes*; A Wiley-Interscience Publication, Newyork, **1984**.
- Ruthven, M.D. Molecular Sieve Separations. *Chemie Ingenieur Technik*, 2011, 83, 44–52.
- Ruthven, M.D.; Reyes, S.C. Adsorptive Separation of Light Olefins from Paraffins. *Microporous and Mesoporous Materials*, **2007**, 104, 59–66.
- Ruthven, D.M.; Brandani, S. Analysis of ZLC Desorption Curves for Liquid Systems. *Chemical Engineering Science*, **1995**, 50, 2055-2059.
- Sander, A.; Skansi, D.; Bolf, N. Heat and Mass Transfer Models in Convection Drying of Clay Slabs. *Ceramics International*, **2003**, 29, 641–653.
- Sandi, G.; Winans, R.E.; Seifert, S.; Carrado, K. A. In Situ SAXS Studies of the Structural Changes of Sepiolite Clay and Sepiolite-Carbon Composites with Temperature. *Chem. Mater.*, **2002**, 14, 739-742.
- Sarkar, M.; Acharya, K.P.; Bhattacharya, B. Modeling the Adsorption Kinetics of Some Priority Organic Pollutants in Water from Diffusion and Activation Energy Parameters. *Journal of Colloid and Interface Science*, **2003**, 266, 28–32.

- Savitz, S.; Siperstein, F.R.; Huber, R.; Tieri, S. M.; Gorte, R.; Myers, A.; Grey, C.P.; Corbin, D.R. Adsorption of Hydrofluorocarbons HCF-314 and HCF-314A on X and Y Zeolites: Effect of Ion-Exchange on Selectivity and Heat of Adsorption. *J.Phys.Chem.B.*, **1999**, 103.
- Seader, J.D.; Henley, E.J. *Separation Process Principles*; Second Edition, John Wiley and Sons, Inc., **2006**.
- Sebastian, J.; Pillai, R. S.; Peter, S.A.; Jasra, R.V. Sorption of N₂, O₂ and Ar in Mn(II)-Exchanged Zeolites A and X Using Volumetric Measurements and Grand Canonical Monte Carlo Simulation. *Ind. Eng. Chem. Res.*, **2007**, 46, 6293-6302.
- Shen, D.; Bülow, M.; Jale, S.R.; Fitch, F.R.; Ojo, A.F. Thermodynamics of Nitrogen and Oxygen Sorption on Zeolites LiLSX and CaA. *Microporous and Mesoporous Material*, **2001**, 48, 211-217.
- Shinde, P.D.; Mahajan, V.A.; Borate, H.B.; Tillu, V.H.; Bal, R.; Chandwadkar, A.; Wakharkar, R.D. Li-X Type Zeolite Mediated Michael Addition of Thiols to Cyclic Enones and its Application in the Synthesis of 13-Thiaprostaglandins. *Journal of Molecular Catalysis A: Chemical*, **2004**, 216, 115-119.
- Silva, J. A.C.; Da Silva, F. A.; Rodrigues, A.E. An Analytical Solution for the Analysis of Zero-Length-Column Experiments with Heat Effects. *Ind. Eng. Chem. Res.*, **2001**, 40, 3697-3702.
- Silva, F.A.; Rodrigues, E.A. Adsorption Equilibria and Kinetics for Propylene and Propane over 13X and 4A Zeolite Pellets. *Ind. Eng. Chem. Res.*, **1999**, 38, 2051-2057.
- Suzuki, M. *Adsorption Engineering*; Elsevier Science Publishers B.V.: Tokyo, **1990**.
- Tan, H. K. S. Ion Exchange Accompanied by Neutralization Reaction: Removal of Dilute Acids by Anion Exchange. *Separation Science and Technology*, **2000**, 35: 1, 23-38.
- Traegner, U.K.; Suidan M. T. Parameter Evaluation for Carbon Adsorption. *Journal of Environmental Engineering*, **1989**, 115: 1, 109-128.
- Tsai, W.T.; Chen, H.P.; Hsieh, M.F.; Sun, H.F.; Chien, S.F. Regeneration of Spent Bleaching Earth by Pyrolysis in a Rotary Furnace. *J. of Analytical and Applied Pyrolysis*, **2002**, 63, 157-170.
- Walton, K.S.; Abney, M.B.; LeVan, M.D. CO₂ Adsorption in Y and X Zeolites Modified by Alkali Metal Cation Exchange. *Microporous and Mesoporous Material*, **2006**, 91, 78-84.
- Yang, J.; Hand, D. W.; Crittenden, J. C.; Hokanson, D. R.; Oman, E. J.; Audeves, D. Dynamic Mathematical Modeling of an Isothermal Three-Phase Reactor: Model Development and Validation. *Journal of Environmental Engineering*, **2003**, 129:7, 586-594.

- Zagorodni A.A. (2007). *Ion Exchange Materials Properties and Applications*; First edition, Elsevier B.V.: Amsterdam, pg.36, **2007**.
- Zaman, S.F. *Diffusion and Adsorption of Aromatics in Zeolites by Zero Length Column Technique*; Master of Science in Chemical Engineering, Arabia, pg.33, **2004**.
- Zhan, B.Z.; White, M.A.; Lumsden, M.; Mueller-Neuhaus, J.; Robertson, K.N.; Cameron, T.S.; Gharghour, M. Control of Particle Size and Surface Properties of Crystals of NaX Zeolite. *Chem. Mater.*, **2002**, 14, 3636-3642.

APPENDIX A

ION EXCHANGE STUDY

Kinetics of ion exchange were studied in the concentration range of 3-9 fold equivalent excess of Li^+ , Ca^{2+} and Ce^{3+} ions at 50 °C and 70 °C with traditional and ultrasonic method. Change in the exchange percent of Na^+ in zeolite were given in A1-A3.

Calculation of theoretical exchange capacity (TEC) of NaX zeolite

Theoretical exchange capacity (TEC) is the exchangeable cations in zeolite given as meq cations /g zeolite. Na^+ ion is the exchangeable ion in X zeolite. Common method for the determination of the theoretical exchange capacity of zeolites is chemical analysis. Therefore, theoretical exchange capacity (TEC) of NaX zeolite was determined by fusion dissolution technique with Inductively Coupled Plasma Atomic Emission Spectroscopy (ICP-AES) found as 5.7 meq g^{-1} zeolite in dry basis and considered in all calculations: change in the exchange percent of Na^+ ion and milliequivalent of counter ions (Li^+ , Ca^{2+} and Ce^{3+} ions) per gram of the zeolite.

Monovalent lithium, divalent calcium and trivalent cerium ions actually must displace one, two and three sodium ions, respectively. Since Na^+ and Li^+ ions which have a valence of 1; 1 mmol/g zeolite = 1 meq/g zeolite, whereas for a divalent Ca^{2+} (the valence of 2) and trivalent Ce^{3+} ions (the valence of 3); 1 mmol/g zeolite = 2 meq/g zeolite and 1mmol/g = 3meq/g zeolite, respectively.

The ion exchange experiments were carried out by contacting the zeolite (NaX) with LiCl , $\text{CaCl}_2 \cdot 2\text{H}_2\text{O}$ and $\text{CeCl}_3 \cdot 7\text{H}_2\text{O}$ solution including times more Li^+ , Ca^{2+} and Ce^{3+} ions (3, 5, 6 and 9 fold equivalent excess) according to theoretically needed to exchange Na^+ ions in X zeolite in order to obtain fully exchanged X zeolite with Li^+ , Ca^{2+} and Ce^{3+} ions.

A.1. Li- Exchanged NaX Zeolite

Table A.1. Change in the exchange percent of Na⁺ with excess of Li⁺ ion at 50 °C.

Time (h)	Zeolite Code					
	3 T	3 U	6 T*	6 U*	9 T	9 U
0.25	47	46	56	53	59	64
0.5	48	46	52	53	56	62
1	51	48	52	58	57	65
2	53	53	53	61	56	69
3	47*	61	53	64	63*	74
5	46	60	54	65	63	72

*experiments repeated as twice

Table A.2. Change in the exchange percent of Na⁺ with excess of Li⁺ ion at 70 °C.

Time (h)	Zeolite Code					
	3 T	3 U	6 T	6 U	9 T	9 U
0.25	46	49	62	58	68	66
0.5	52	50	56	59	68	68
1	52	51	58	59	68	69
2	50	52	58	59	69	76
3	47	52	62	65	69	76
5	48	52	62	65	68	75

Table A.3. Change in the exchange percent of Na⁺ with 9 excess of Li⁺ in a different medium at 70 °C.

Time (h)	T	U-125 W	U-200 W	UB-320 W
0.25	69	66	63	63
0.5	68	65	65	66
1	68	69	70	66
2	69	76	73	67
3	70	76	71	66

A.2. Ca- Exchanged NaX Zeolite

Table A.4. Change in the exchange percent of Na⁺ with excess of Ca²⁺ ion at 50 °C.

Time (h)	Zeolite Code					
	3 T	3 U	6 T	6 U	9 T	9 U
0.25	51	50	55	58	60	58
0.5	52	51	58	59	62	58
1	54	53	57	60	57	62
2	54	53	57	60	61	62
3	54	54	58	59	61	65
5	53	54	59	61	62	64

Table A.5. Change in the exchange percent of Na⁺ with excess of Ca²⁺ at 70 °C.

Time (h)	Zeolite Code					
	3 T	3 U	6 T	6 U	9 T	9 U
0.25	51	55	54	58	62	58
0.5	51	55	57	56	62	63
1	52	55	61	60	63	63
2	49	56	61	61	65	67
3	52	56	60	63	67	72
5	52	57	62	66	68	72

Table A.6. Change in the exchange percent of Na⁺ with 9 excess of Ca²⁺ ion in a different medium at 70 °C.

Time (h)	T	U-125 W	U-200 W	UB-320 W
0.25	62	58	65	61
0.5	65	63	65	59
1	62	63	67	60
2	65	67	67	59
3	65	72	67	62

A.3. Ce- Exchanged NaX Zeolite

Table A.7. Change in the exchange percent of Na⁺ with excess of Ce³⁺ ion at 50 °C.

Time (h)	Zeolite Code							
	3 T	3 U	5 T	5 U	6 T	6 U	9 T	9 U
0.25	44	43	46	42	47	47	46	44
0.5	46	44	47	45	47	48	51	48
1	46	49	45	49	49	50	51	51
2	46	51	48	51	48	50	53	51
3	47	52	48	54	49	51	53	51
5	49	51	50	53	51	52	54	52

Table A.8. Change in the exchange percent of Na⁺ with excess of Ce³⁺ ion at 70 °C.

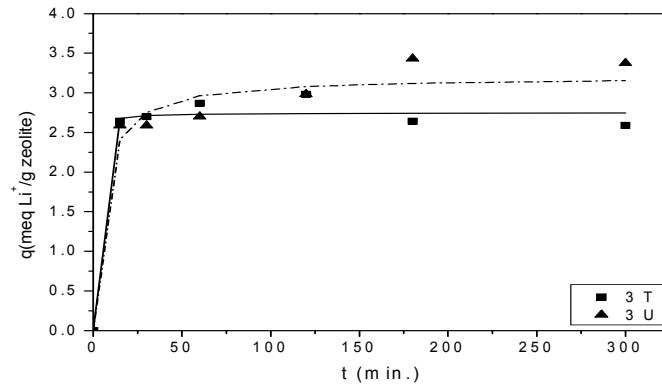
Time (h)	Zeolite Code							
	3 T	3 U	5 T	5 U	6 T	6 U	9 T	9 U
0.25	38	38	38	46	46	46	49	48
0.5	39	42	40	53	48	49	49	50
1	40	44	41	57	49	54	51	50
2	40	51	41	61	53	55	52	50
3	41	53	50	66	51	57	54	55
5	41	54	50	65	51	57	54	56

Table A.9. Change in the exchange percent of Na⁺ with 5 excess of Ce³⁺ ion in a different medium at 70 °C.

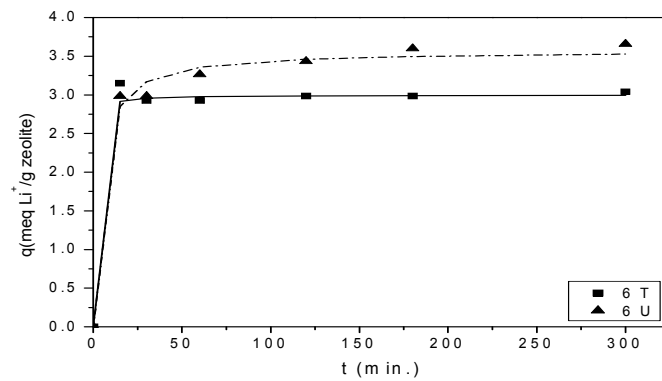
Time (h)	T	U-125 W	U-200 W	UB-320 W
0.25	38	46	44	44
0.5	40	53	48	50
1	41	57	48	49
2	41	61	51	48
3	50	69	59	47

A.4. Ion Exchange Kinetic Study

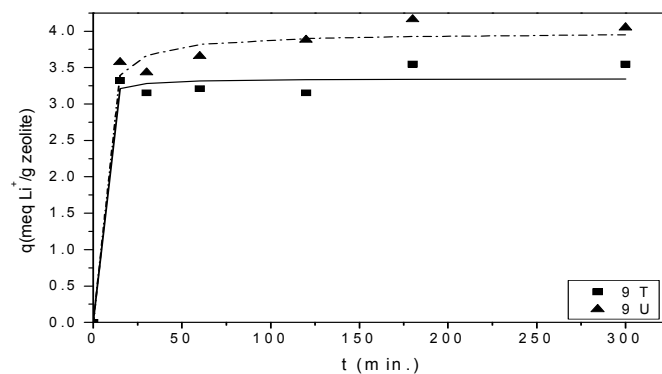
Kinetic curves of Li^+ , Ca^{2+} and Ce^{3+} ions exchange with fold equivalent excess by using the pseudo second order reaction model at 50 °C and 70 °C were given in Figure A1-A3.



(a)

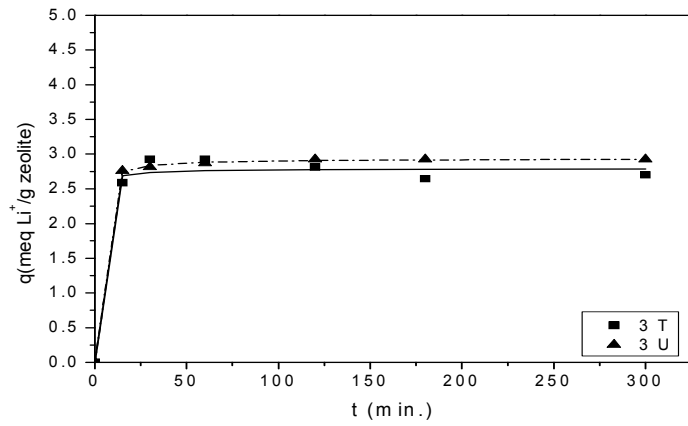


(b)

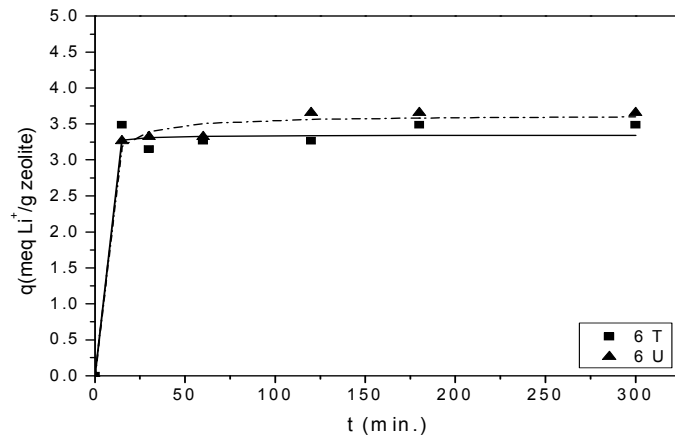


(c)

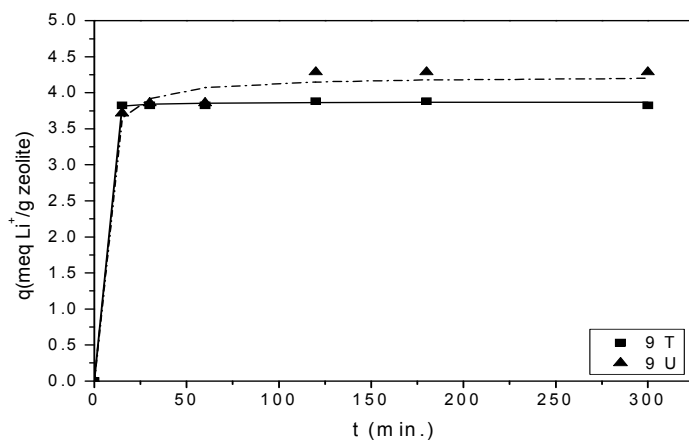
Figure A.1. Kinetic curves of Li- exchange at 50 °C with fold equivalent excess of (a) 3 (b) 6 (c) 9; model: 2nd order reaction equation (line), experiments: points.



(a)

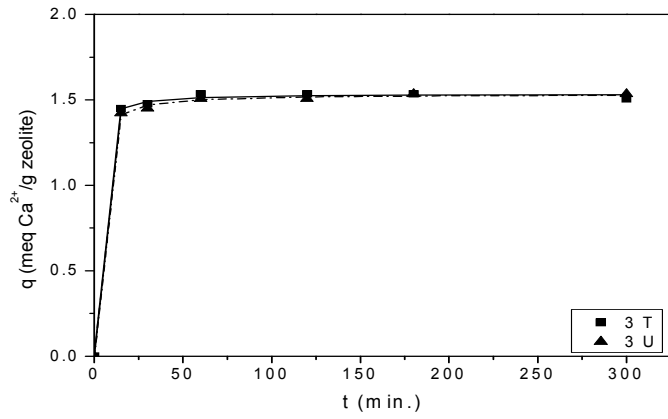


(b)

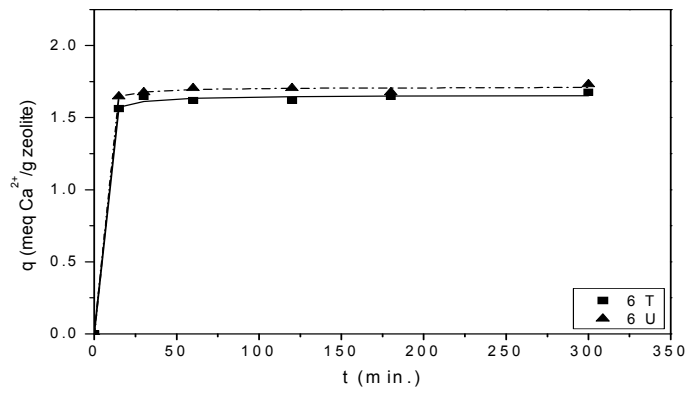


(c)

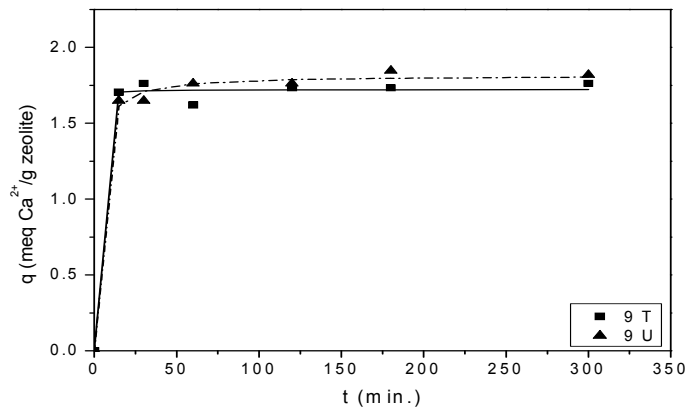
Figure A.2. Kinetic curves of Li- exchange at 70 °C with fold equivalent excess of (a) 3 (b) 6 (c) 9; model: 2nd order reaction equation (line), experiments: points.



(a)

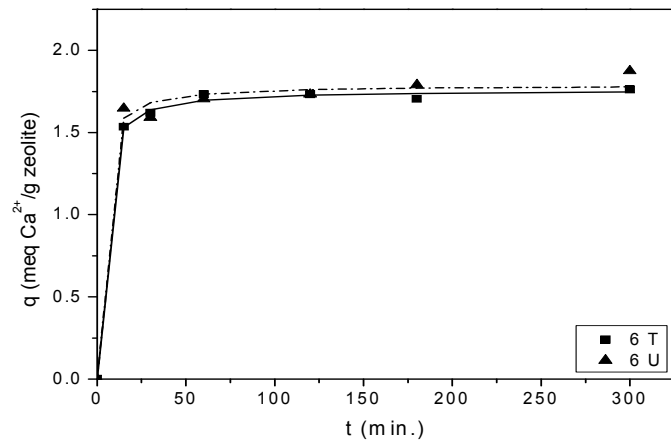
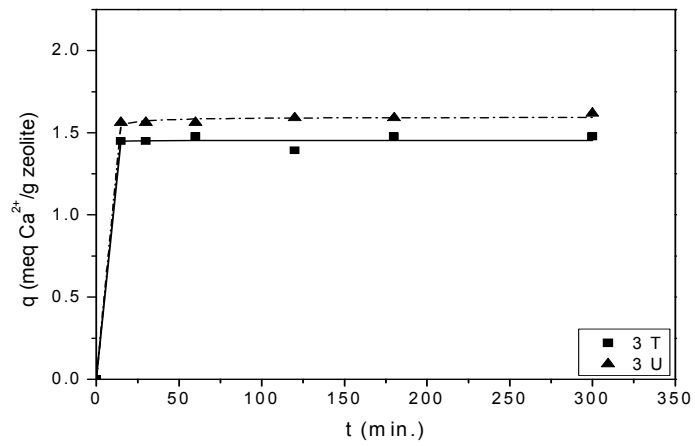


(b)

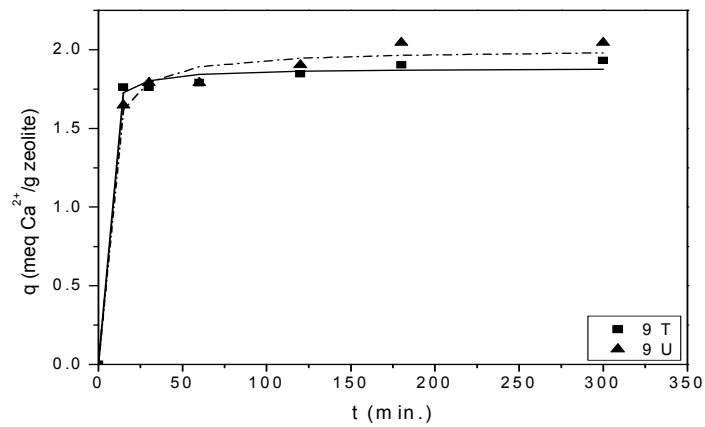


(c)

Figure A.3. Kinetic curves of Ca-exchange at 50 °C with fold equivalent excess of (a) 3 (b) 6 (c) 9; model: 2nd order reaction equation (line), experiments: points.

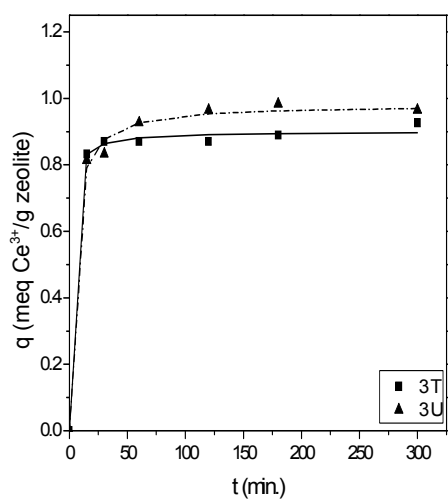


(b)

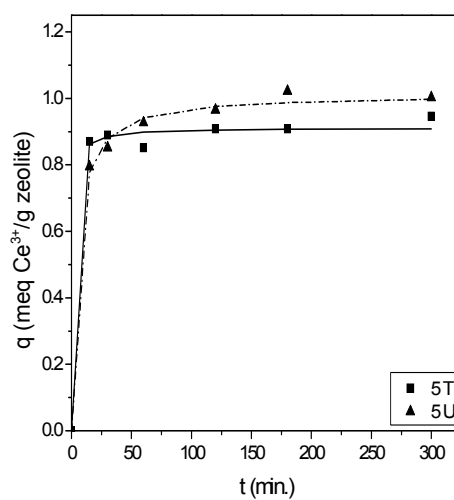


(c)

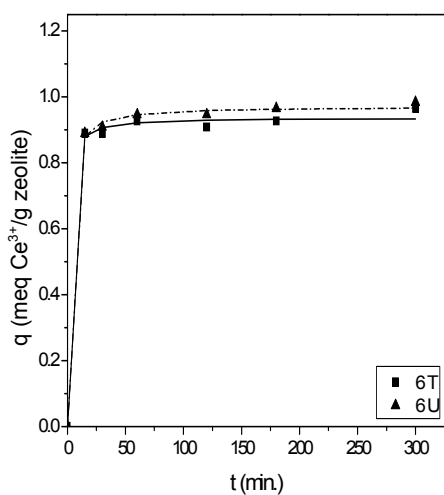
Figure A.4. Kinetic curves of Ca-exchange at 70 °C with fold equivalent excess of (a) 3 (b) 6 (c) 9 ; model: 2nd order reaction equation (line), experiments: points.



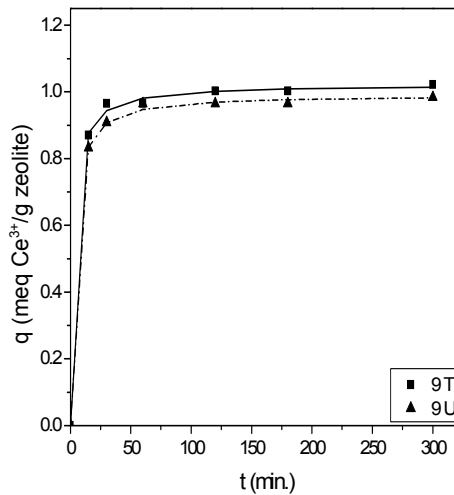
(a)



(b)

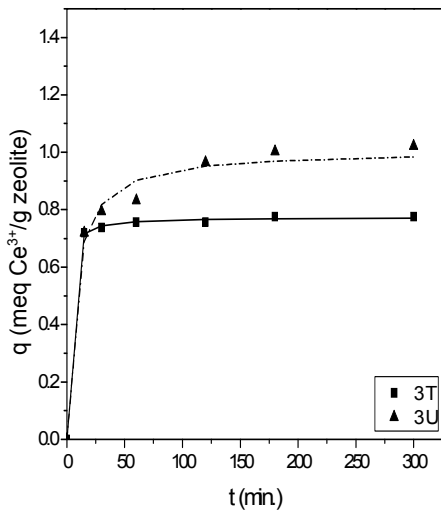


(c)

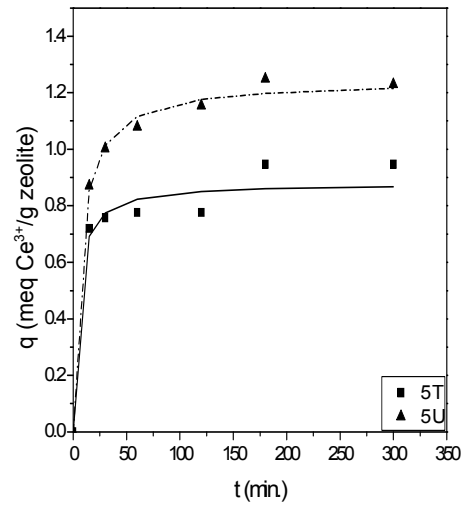


(d)

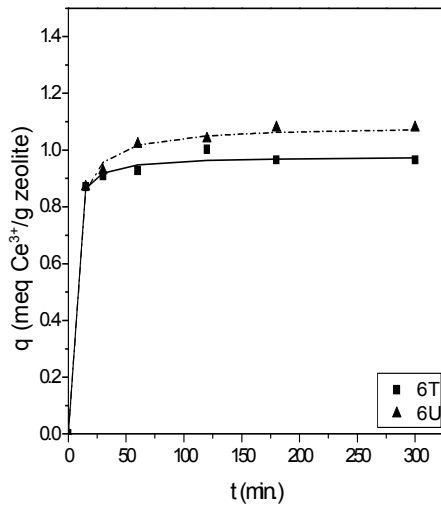
Figure A.5. Kinetic curves of Ce-exchange at 50 °C with fold equivalent excess of (a) 3 (b) 5 (c) 6 (d) 9; model: 2nd order reaction equation (line), experiments: points.



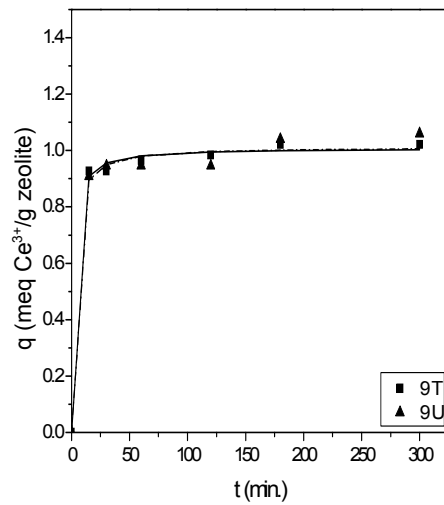
(a)



(b)



(c)



(d)

Figure A.6. Kinetic curves of Ce^{3+} exchange at $70\text{ }^{\circ}\text{C}$ with fold equivalent excess of (a) 3 (b) 5 (c) 6 (d) 9; model 2nd order reaction equation (line), experiments: points.

APPENDIX B

THE TEMPERATURE EFFECT ON INTRAPARTICLE RATE CONSTANT OF ION EXCHANGE

The activation energy of counter (Li^+ , Ca^{2+} and Ce^{3+}) ions exchange were obtained by using the change in the intraparticle diffusion rate constant, k_i , with temperature. The plots of rate constant versus the reciprocal temperature were given in Figure B.1-B.3.

B.1. Li- Exchange

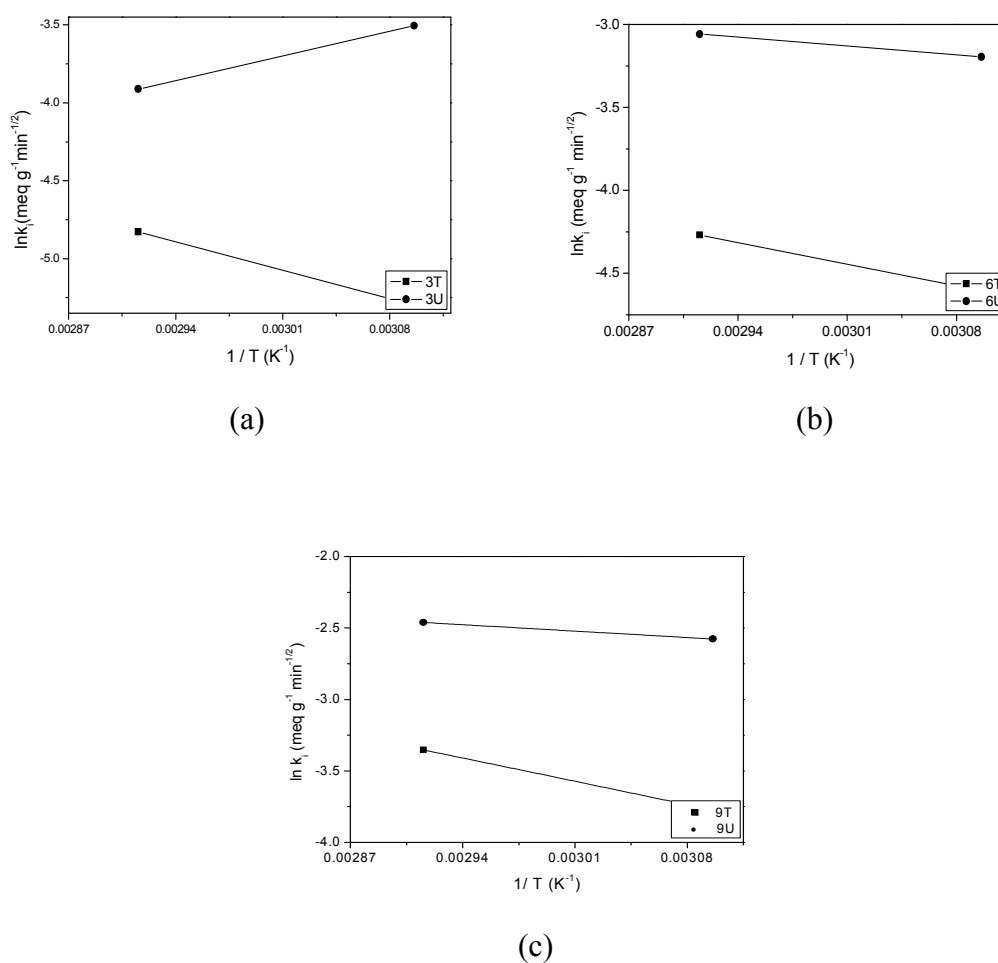
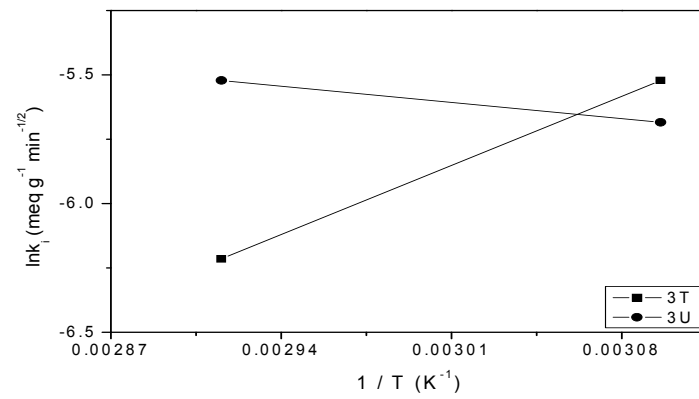
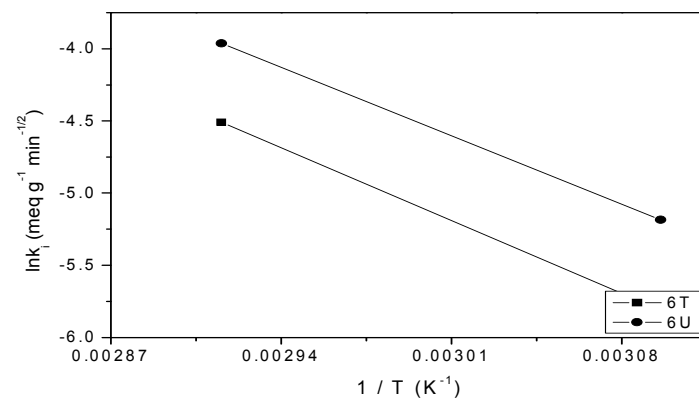


Figure B.1. The relation between intraparticle rate constant and inverse of temperature for Li- exchange (fold equivalent excess: (a) 3 (b) 6 (d) 9).

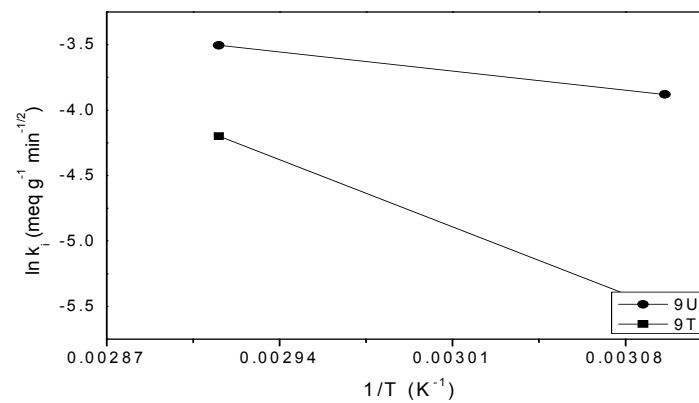
B.2. Ca- Exchange



(a)



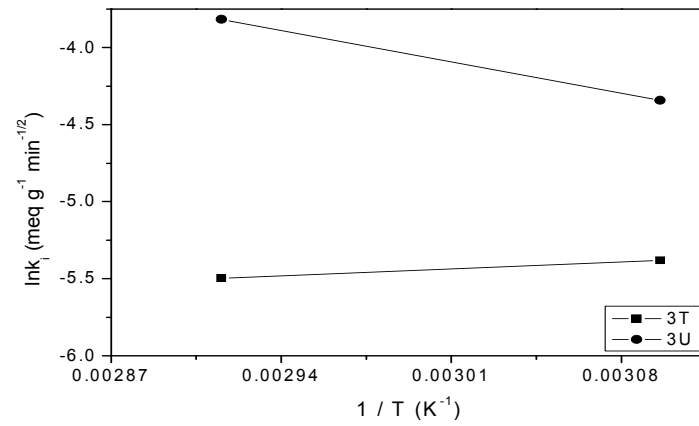
(b)



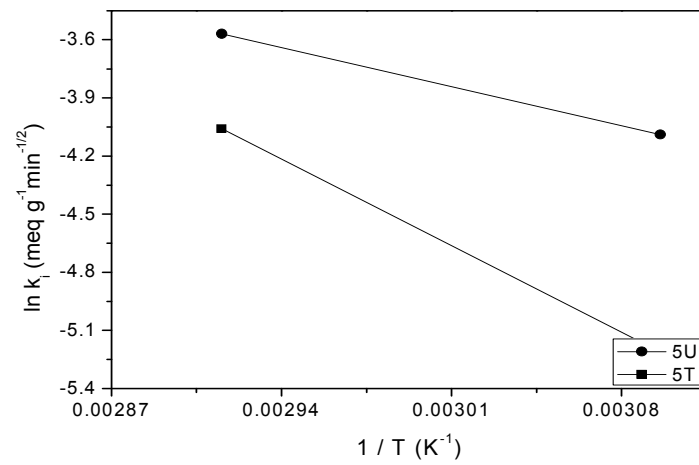
(c)

Figure B.2. The relation between intraparticle rate constant and inverse of temperature for Ca- exchange (fold equivalent excess: (a) 3 (b) 6 (d) 9).

B.3. Ce- exchange



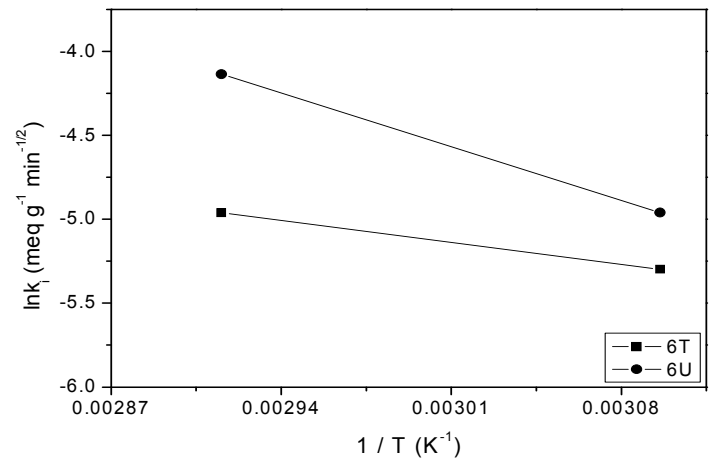
(a)



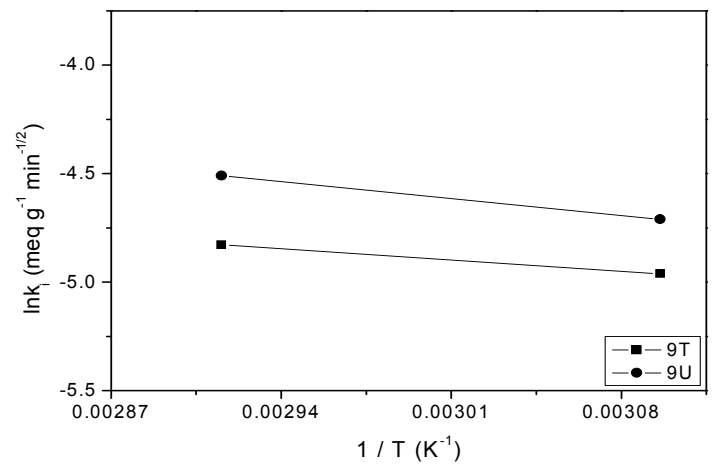
(b)

Figure B.3. The relation between intraparticle rate constant and inverse of temperature for Ce-exchange (fold equivalent excess: (a) 3 (b) 5 (c) 6 (d) 9).

(cont. on next page)



(c)



(d)

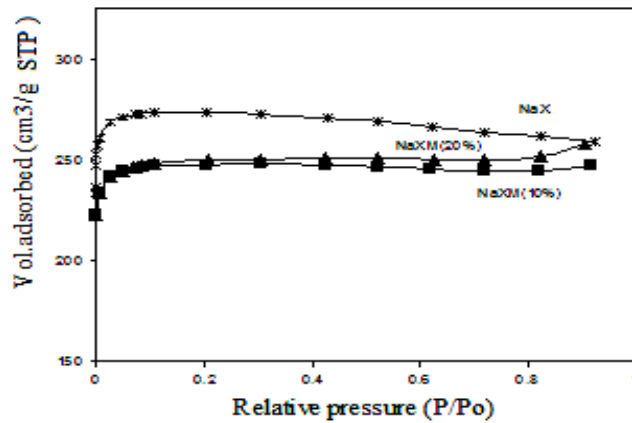
Figure B.3. (cont).

APPENDIX C

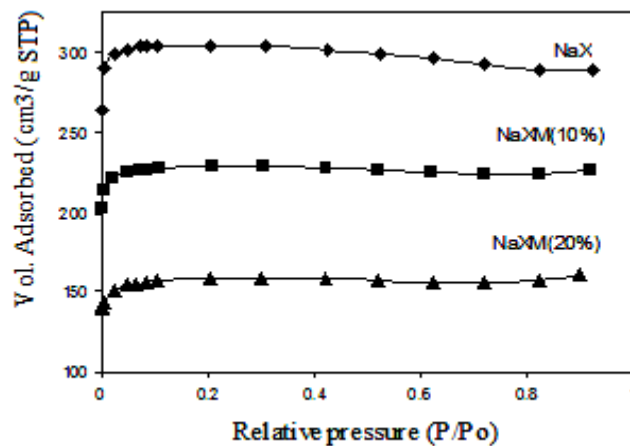
CHARACTERIZATION STUDY FOR ZEOLITE GRANULES

The powder form of NaX zeolite was granulated by using the Montmorillonite and Sepiolite minerals. N₂ adsorption isotherm (at 77 K) of granulated zeolites were given in Figure C1 and C2.

C.1. N₂ Adsorption Isotherms of Zeolites

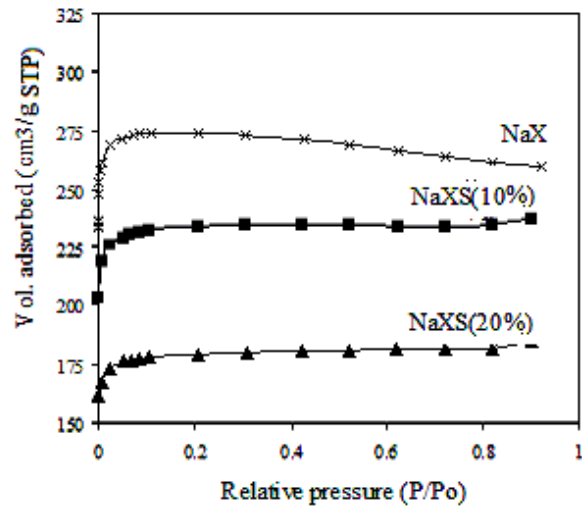


(a)

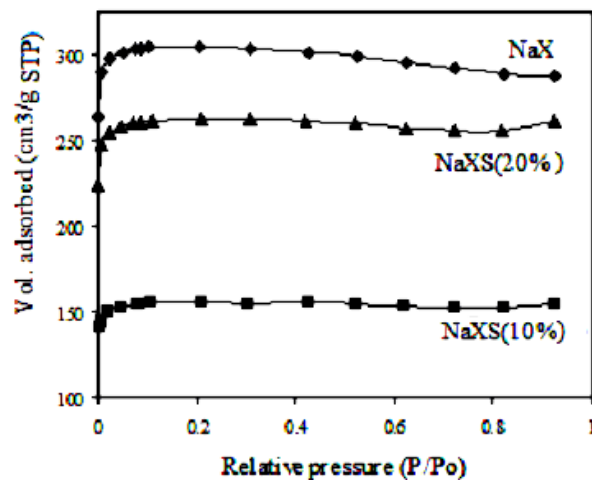


(b)

Figure C.1. N₂ adsorption isotherms of NaX zeolite, granulated form with montmorillonite (NaXM) by using (a) procedure A (b) procedure B.



(a)



(b)

Figure C.2. N_2 adsorption isotherms of NaX zeolite, granulated form with sepiolite (NaXS) by using (a) procedure A (b) procedure B.

APPENDIX D

ZLC STUDY

The parameters used in the ZLC experiment were tabulated in Table D.1. The experimental data obtained from ZLC desorption curves were plotted in the form of C/C_0 versus $t^{-1/2}$ given in Figure D.1-D.12.

Table D1. Parameters of ZLC experiment.

Zeolites	Mass of adsorbent (mg)	Crystal radius, r, (cm)x10⁴	Volume of adsorbent, V_s, (cm³) x10⁴	Density of adsorbent, ρ_s, (g cm⁻³)	Purge flow rate, (cm³ s⁻¹)	Temp. (K)
NaX	1.80		9.57	1.881		303
LiX	1.65	1	8.87	1.860	1.167	333
CaNaX	2.05		10.11	2.028		363
CeNaX	1.90		8.26	2.300		

D.1. ZLC Response Curves for N₂, CO₂ and CH₄ Gases on NaX, LiX, CaNaX and CeNaX Zeolites

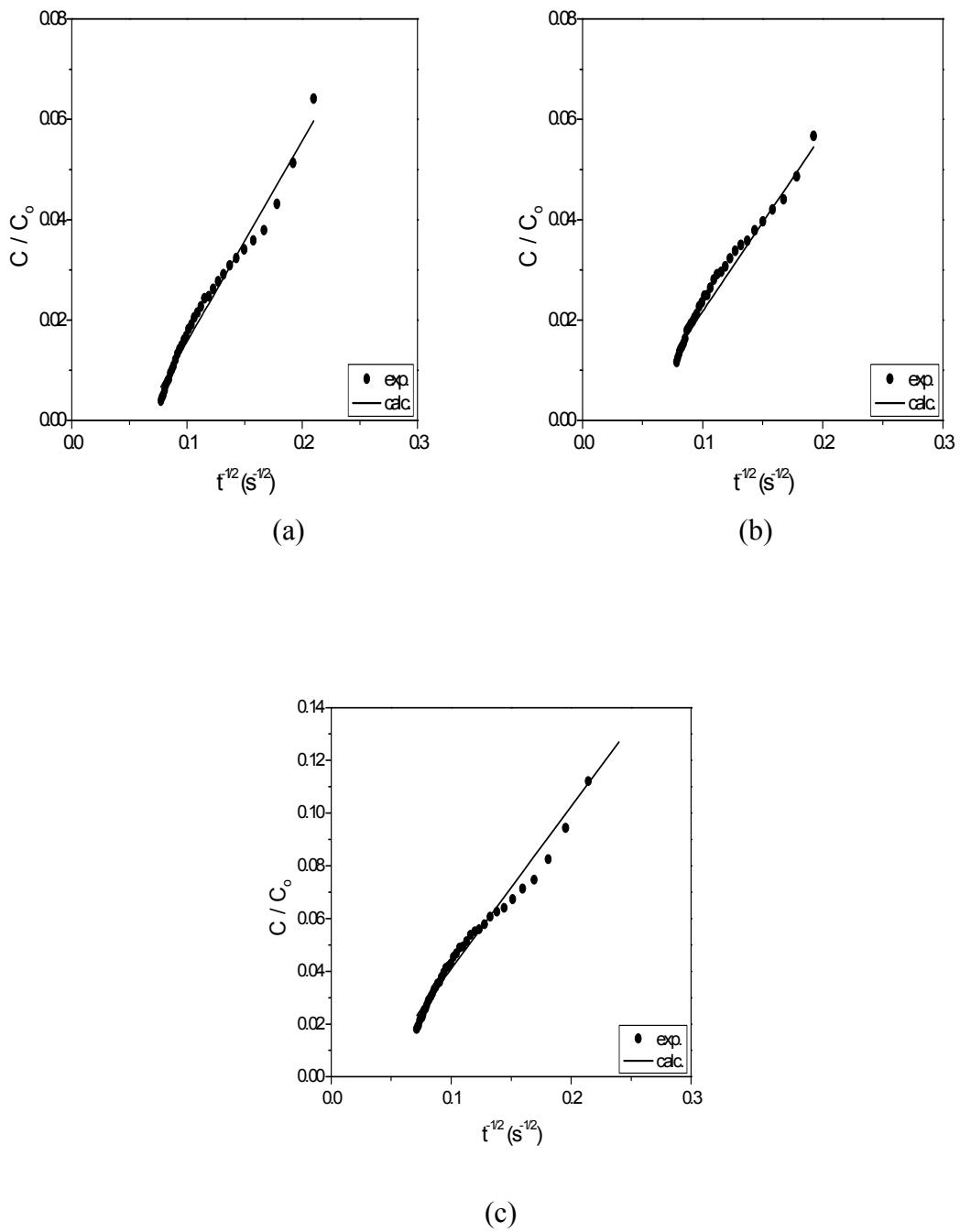
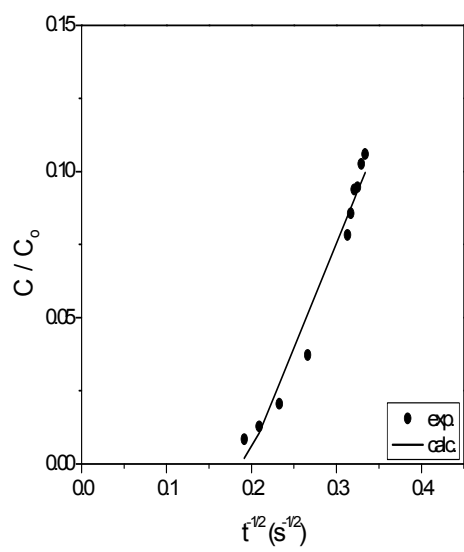
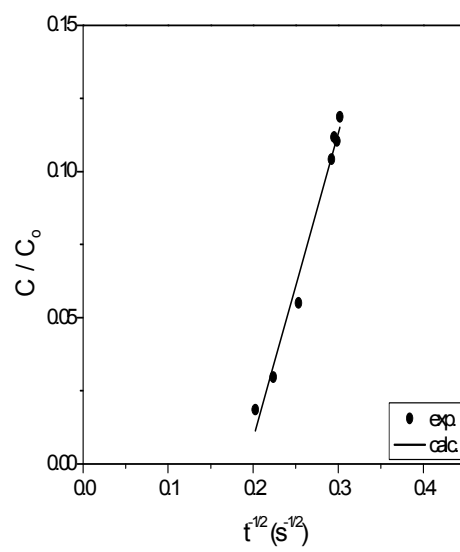


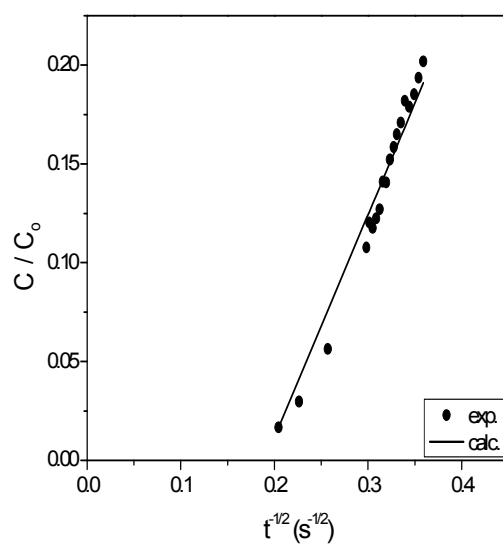
Figure D.1. ZLC response curves for N₂ – NaX (a) 30 °C (b) 60 °C (c) 90 °C.



(a)

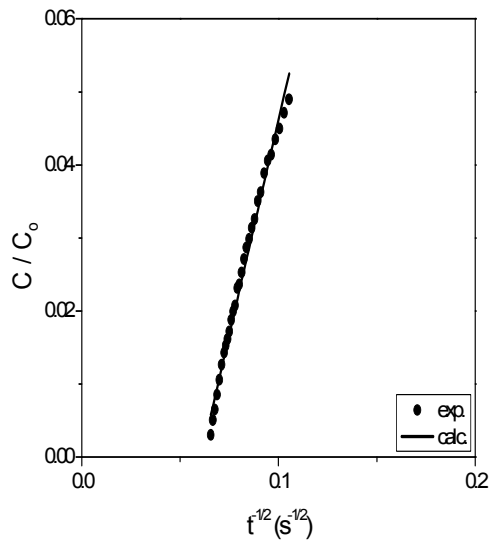


(b)

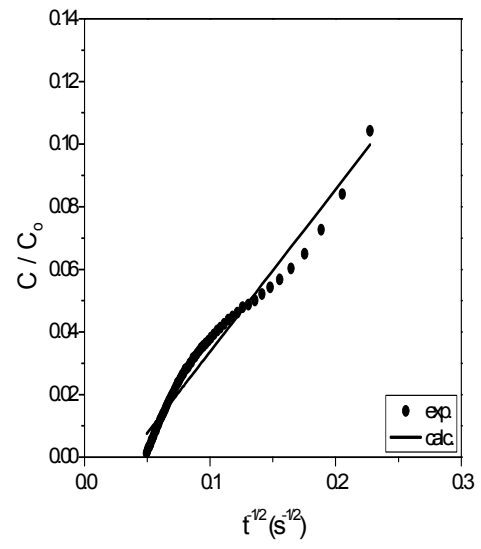


(c)

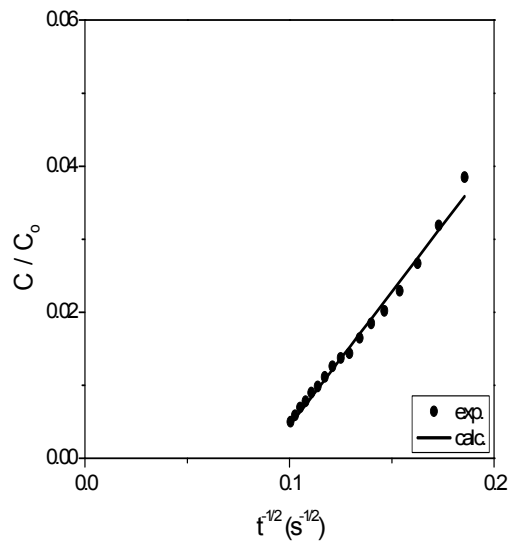
Figure D.2. ZLC response curves for CH₄ - NaX (a) 30 °C (b) 60 °C (c) 90 °C.



(a)

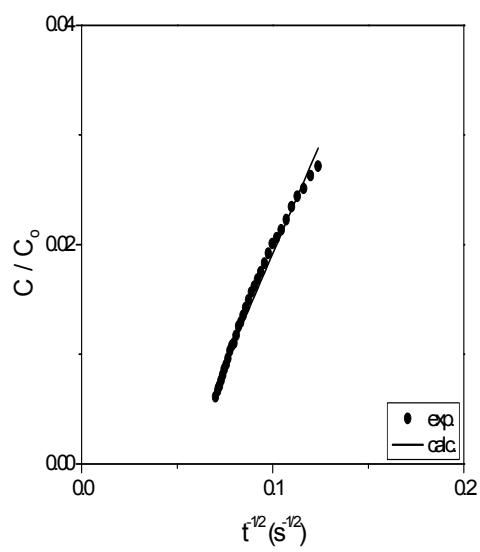


(b)

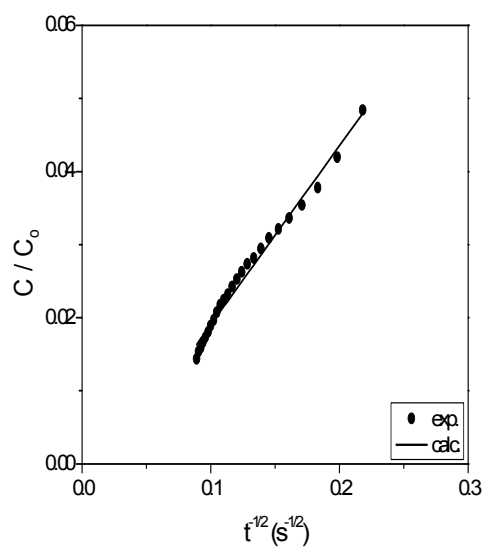


(c)

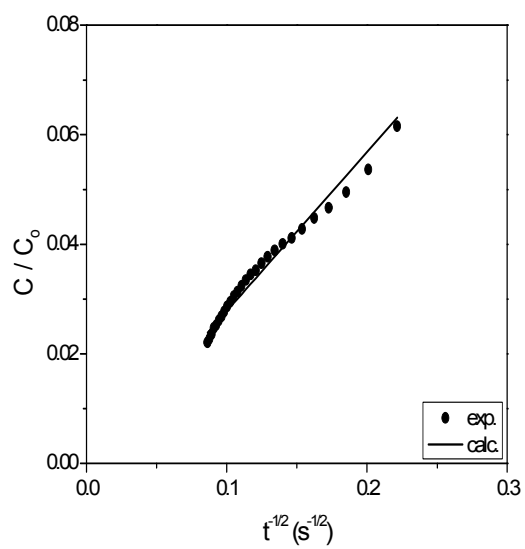
Figure D.3. ZLC response curves for CO₂-NaX (a) 30 °C (b) 60 °C (c) 90 °C.



(a)

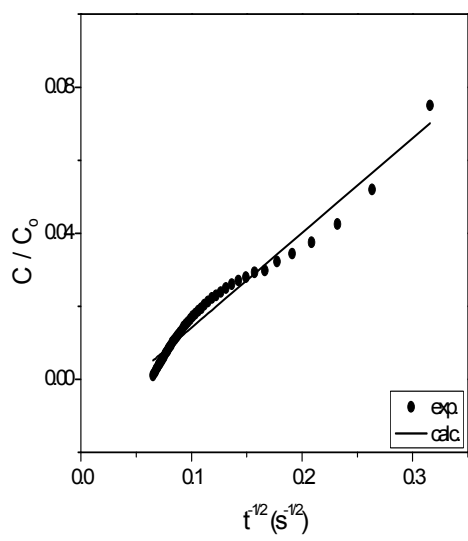


(b)

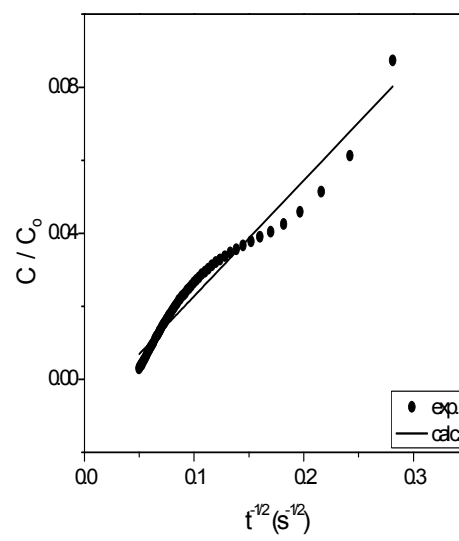


(c)

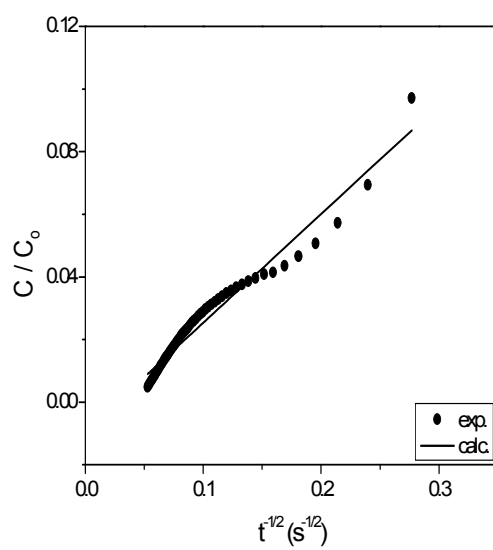
Figure D.4. ZLC response curves for N_2 –LiX-U (a) 30 °C (b) 60 °C (c) 90 °C.



(a)

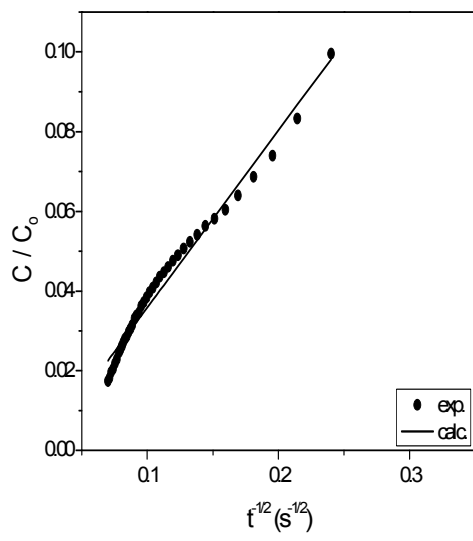


(b)

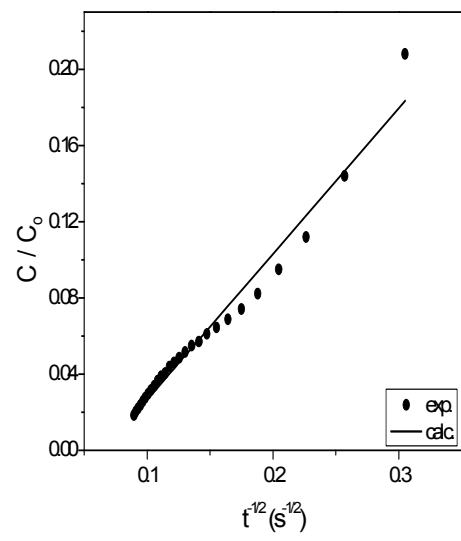


(c)

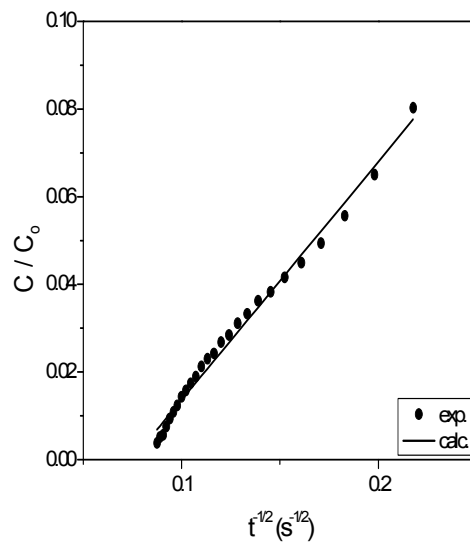
Figure D.5. ZLC response curves for CH₄–LiX-U (a) 30 °C (b) 60 °C (c) 90 °C.



(a)

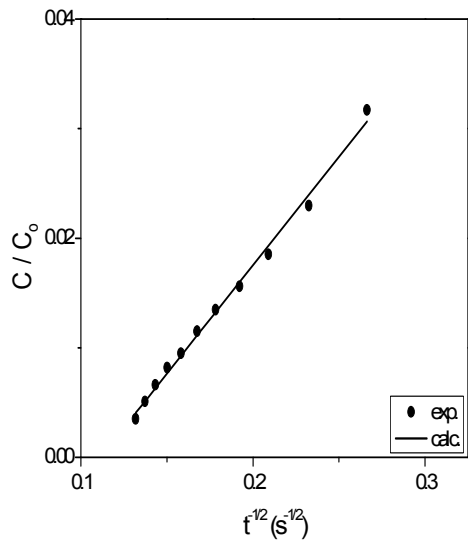


(b)

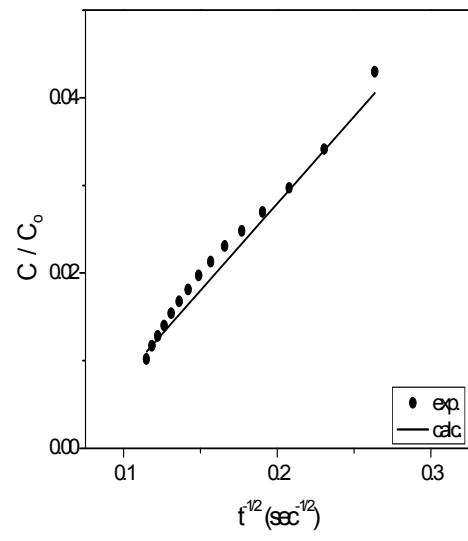


(c)

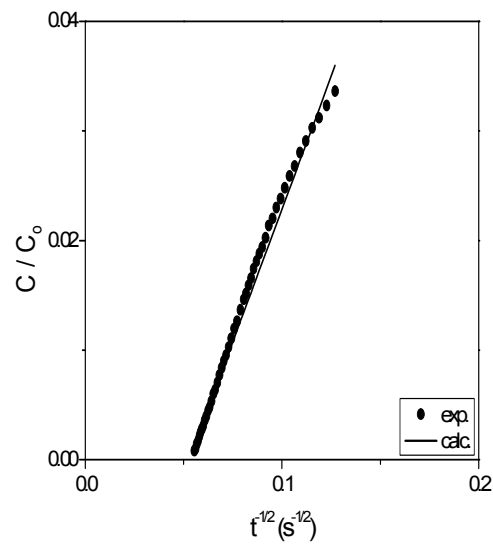
Figure D.6. ZLC response curves for CO₂-LiX-U (a) 30 °C (b) 60 °C (c) 90 °C.



(a)

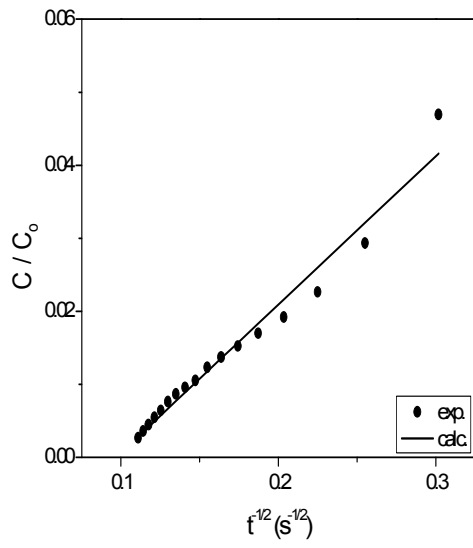


(b)

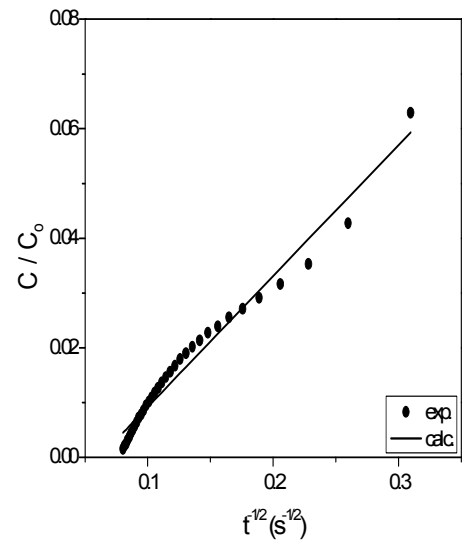


(c)

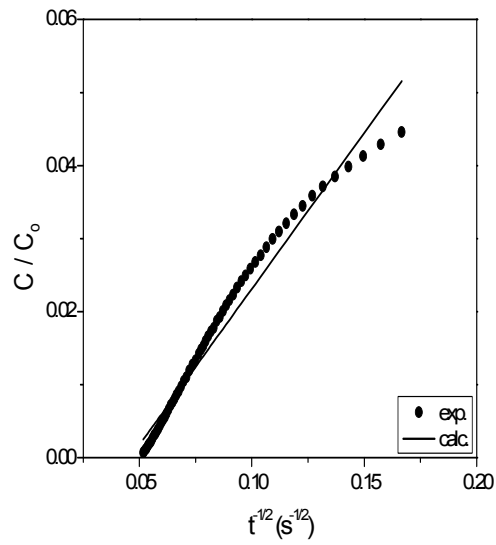
Figure D.7. ZLC response curves for N₂-CaNaX-U (a) 30 °C (b) 60 °C (c) 90 °C.



(a)

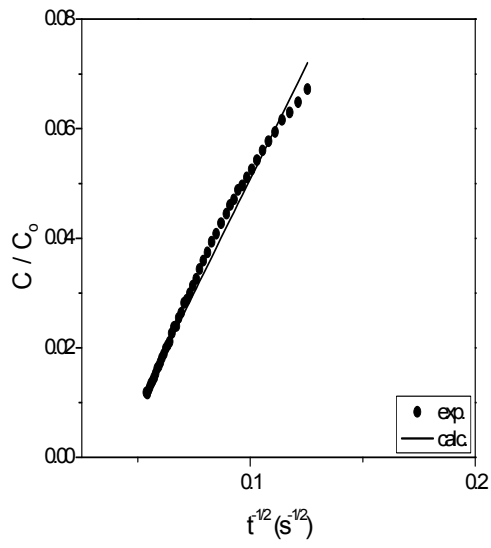


(b)

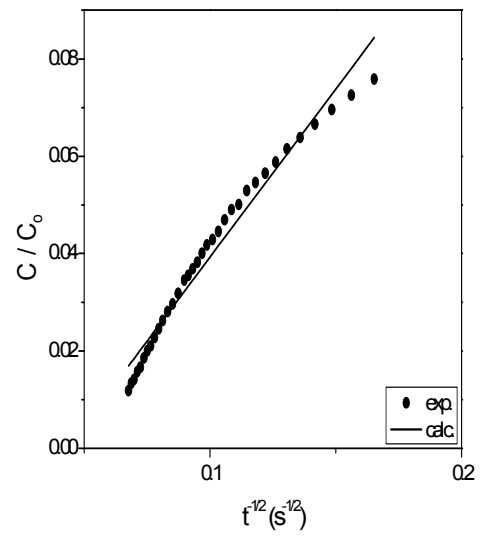


(c)

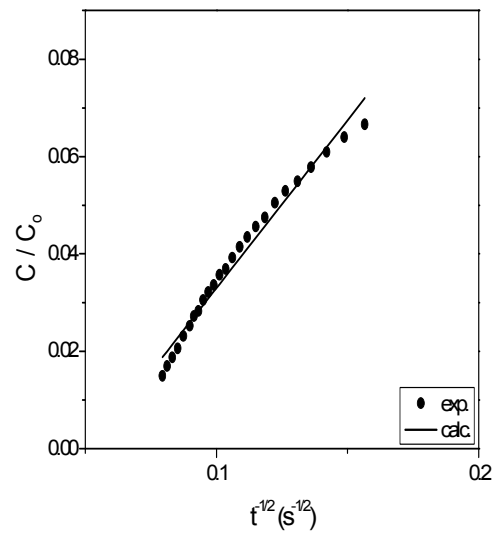
Figure D.8. ZLC response curves for CH₄-CaNaX-U (a) 30 °C (b) 60 °C (c) 90 °C.



(a)

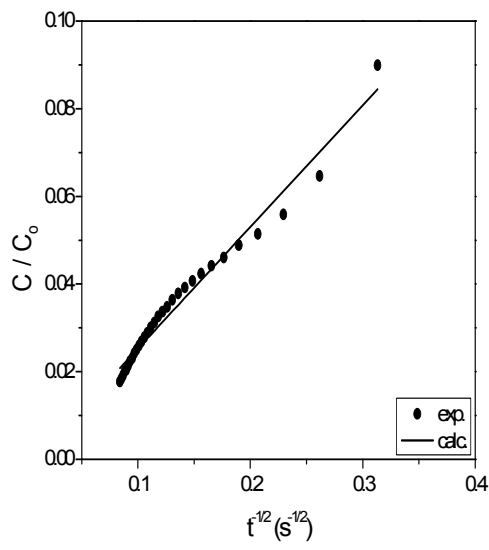


(b)

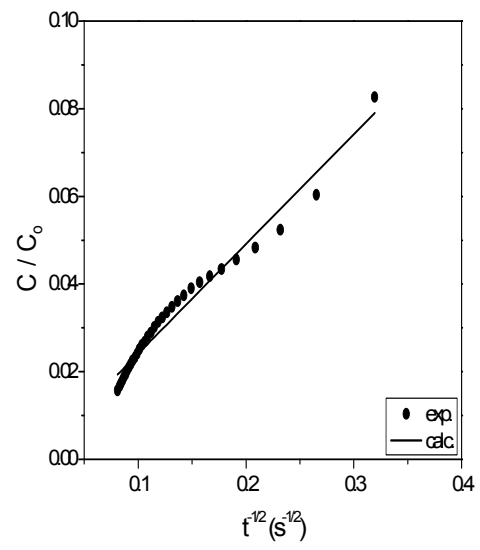


(c)

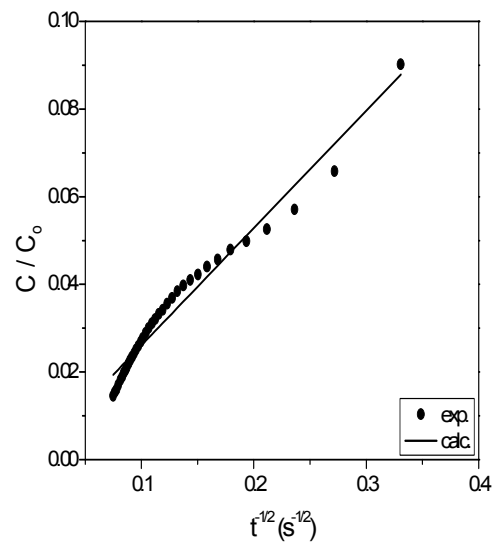
Figure D.9. ZLC response curves for CO₂– CaNaX-U (a) 30 °C (b) 60 °C (c) 90 °C.



(a)



(b)



(c)

Figure D.10. ZLC response curves for $N_2 - CeNaX-U$ (a) 30 °C (b) 60 °C (c) 90 °C.

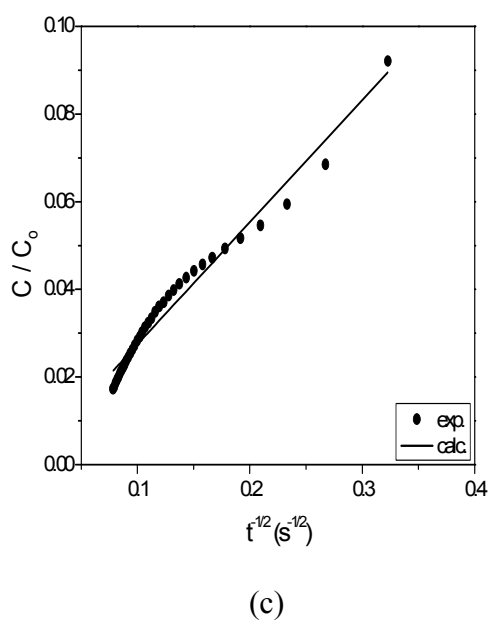
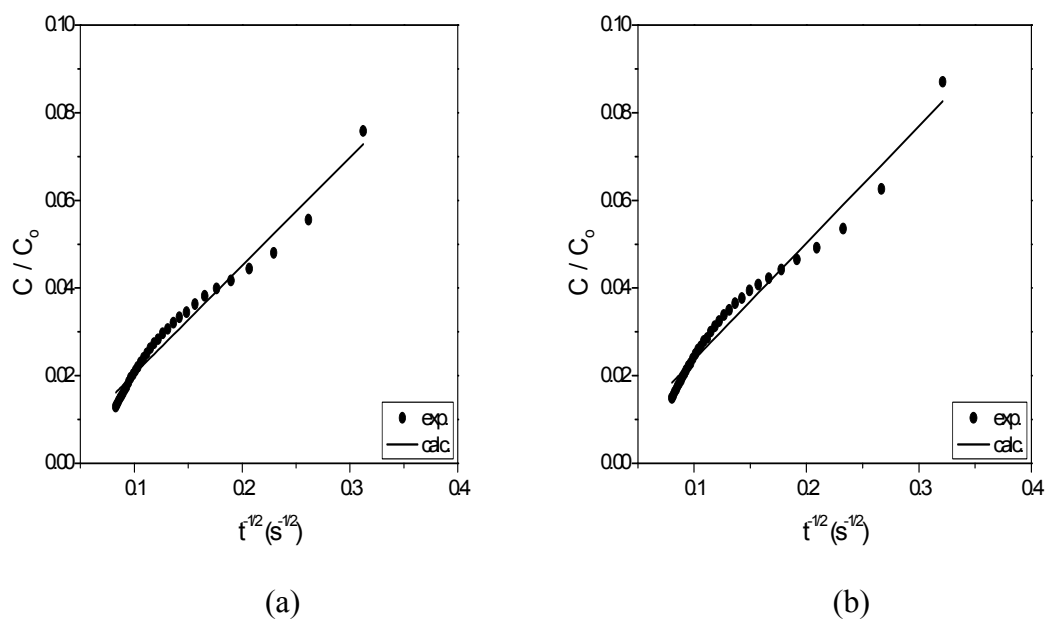
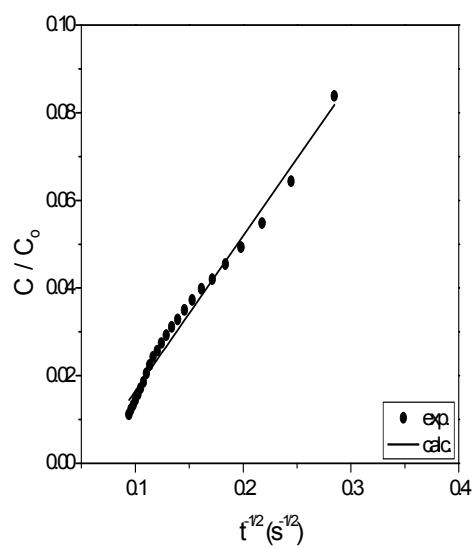
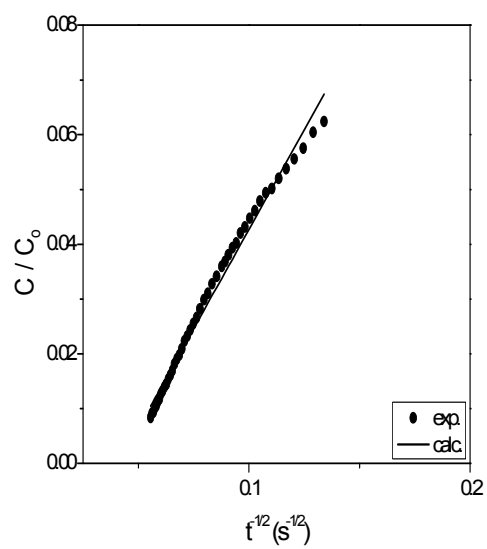


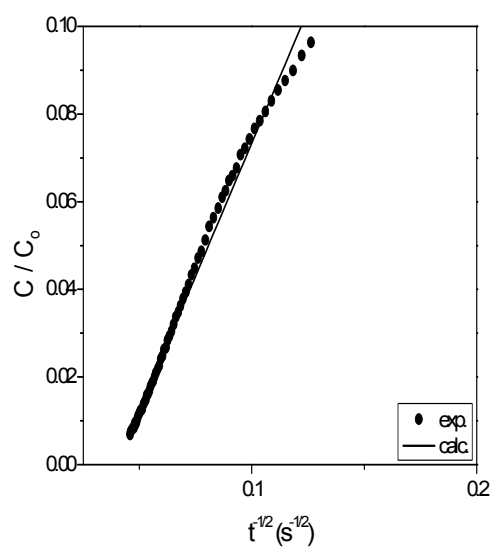
Figure D.11. ZLC response curves for CH₄-CeNaX-U (a) 30 °C (b) 60 °C (c) 90 °C.



(a)



(b)



(c)

Figure D.12. ZLC response curves for CO₂ – CeNaX-U (a) 30 °C (b) 60 °C (c) 90 °C.

YASEMİN ERTEN KAYA

Date of Birth: 26.06.1977

Place of Birth: İzmir

Citizenship: Turkish

EDUCATION

[1994-1999] B.Sc. (Food Engineering)

Ege University

Department of Food Engineering, İzmir, Turkey

Dissertation: Determination of Quality and Technologic Properties of Some Varieties of Wheat

[2001-2004] M.Sc. (Food Engineering)

İzmir Institute of Technology

Department of Food Engineering, İzmir, Turkey

Dissertation: Use of Domestic Minerals for Vegetable Oil Bleaching

[2004-2011] Ph.D. (Chemical Engineering)

İzmir Institute of Technology

Department of Chemical Engineering, İzmir, Turkey

Dissertation: Sorption of N₂, CO₂ and CH₄ on the Ultrasound Enhanced Cation Exchanged X Zeolites.

PUBLICATIONS

Erten-Kaya, Y.; Çakıcıoğlu-Özkan, F., (Submitted Manuscript). Effect of Ultrasound on the Kinetics of Cation Exchange in NaX Zeolite. *Ultrasonic Sonochemistry*. Manuscript Number: ULTSON-D-11-00350, **2011**.

Erten, Y.; Çakıcıoğlu-Özkan, F. Application of The Zero Length Column (ZLC) Technique for Measuring Crystal Diffusivities of NaX and CeNaX Zeolites. *Diffusion-Fundamentals Org.* **2009**, 28, Pp 1-2.

Erten, Y.; Güneş-Yerkesikli, A.; Çetin, A. E.; Çakıcıoğlu-Özkan, F. CO₂ Adsorption and Dehydration Behavior of LiNaX, KNaX, CaNaX and CeNaX Zeolites. *Journal of Thermal Analysis and Calorimetry*. **2008**, 3, 715–718.

Erten, Y.; Ertürk, H.; Özkan, F. Bleaching of Sunflower Oil Using Clay Mineral from Ankara Region. *The Journal of Academic Food Engineering and Food Industry*, **2005**, 7, 19-23.